2009

Electronic Properties And Microstructures Of Amorphous Sicn Ceramics Derived From Polymer Precursors

Tao Jiang
University of Central Florida

ELECTRONIC PROPERTIES AND MICROSTRUCTURES OF AMORPHOUS SiCN CERAMICS DERIVED FROM POLYMER PRECURSORS

by

TAO JIANG
M.S. University of Central Florida, 2007
M.S. Beijing University of Chemical Technology, China, 2000
B.S.E. Nanchang Institute of Aeronautical Technology, China, 1993

A dissertation submitted in partial fulfillment of the requirements
for the degree of doctor of philosophy
in the Department of Mechanical, Materials and Aerospace Engineering
in the College of Engineering and Computer Science
at the University of Central Florida,
Orlando, Florida

Summer Term
2009

Main Professor: Linan An

ABSTRACT

Polymer-derived ceramics (PDCs) are a new class of high-temperature materials synthesized by thermal decomposition of polymeric precursors. These materials possess many unique features as compared with conventional ceramics synthesized by powder metallurgy based processing. For example, PDCs are neither amorphous nor crystalline. Instead, they possess nano-domain structures. Due to the direct chemical-to-ceramic processing, PDCs can be used for making components and devices with complex shapes. Thus, understanding the properties and structures of these materials are of both fundamental and practical interest. In this work, the structures and electronic behavior of polymer-derived amorphous silicon carbonitrides (SiCNs) were investigated.

The materials were synthesized by pyrolysis of a commercially available liquid precursor. Ceramic materials with varied structures/properties were successfully synthesized by modifying the precursor and using different pyrolysis temperatures. The structures of the obtained materials were studied using XRD, solid state NMR, EPR, FTIR and Raman Spectroscope. The electronic behavior of the materials was investigated by measuring I-V curves, Hall effects, temperature dependent conductivity. The experiments were also performed to measure UV-Visible absorption and dielectric properties of the materials. This work leads to the following significant progresses: (i) developed quantitative technique for measuring free carbon concentration; (ii) achieved better understanding of the electronic

conduction mechanisms and measured electronic structures of the materials for the first time; and (iii) demonstrated that these materials possess unusual dielectric behavior and provide qualitative explanations.

ACKNOWLEDGMENTS

I greatly appreciate the help of Professor Linan An, my advisor. He encouraged me and gave me great advice during my study and research at UCF. He provided direction for my research so that I can get the results as soon as possible.

I would also like to thank Professor Lee Chow, Professor Jiyu Fang, Professor Nina Orlovskaya, and Professor Lei Zhai for their thoughtful comments and assistance in the analysis of critical results. I also appreciate Dr. Ligong Zhang, Dr. Weifeng Fei and Dr. Yansong Wang for their support in discussing experiment results and maintaining apparatus.

I also wish to express my sincere gratitude to all of the staff of the MCF: Mr. Mikhail Klimov, Mr. Zia Rahman, and Mr. Kirk Scammon for their assistance with my experiments; Dr. Hans Van Tol, Dr. Andrew Ozarowski, and Dr. Zhehong Gan, the scientists in Florida State University, for their kind help with EPR and NMR experiments and analysis.

I would especially like to thank my wife, Yun Wei, my parents and my one year old Jessica Jiang for their immense love, support, and constant encouragement.

TABLE OF CONTENTS

LIST OF FIGURES

LIST OF TABLES

CHAPTER ONE: INTRODUCTION

1.1 Overview

Polymer-derived ceramics (PDCs) are a new class of high-temperature materials synthesized by thermal decomposition of polymeric precursors, which possess many advantages over conventional ceramics including fabrication of materials at a relatively lower temperature, lower impurity level, homogeneous elemental distribution and cost efficiency. Another attractive feature of PDCs is their potential to give rise to controlled compositions and structures by varying precursors & process conditions, thus, multifunctional materials with tailored properties could be designed and synthesized. The synthesized materials are typically amorphous in nature, which possess excellent high-temperature properties, such as oxidation and creep resistance, superior high-temperature stability, etc. Previous studies mainly focused on the basic knowledge of PDCs such as chemical and physical changes during the polymer-to-ceramic transformation process, the various properties such as mechanical and thermal properties, and the structures of ultimate ceramics. However, understanding the electronic behavior of these materials and their relationship with atomic and electronic structures has received lesser attention. A thorough understanding of electronic behavior of PDCs will be critical for the synthesis and application of PDCs. In this work, the structures and electronic behavior of polymer-derived SiCN ceramics were studied.

1.2 Outline of Dissertation

This dissertation is organized as follows:

Chapter 2 provides the background information about PDCs and an overview of the available literature on PDCs' synthesis and properties. The following section details the fabrication processes and structural evolution of SiCN polymer-derived ceramics during pyrolysis process, which was thoroughly studied using various analytical characterization methods like FTIR, NMR, Raman spectroscopy and EPR. The fourth chapter focuses on the electronic properties of these polymer-derived ceramics, such as I-V dependence characteristic, Hall Effect, temperature dependence of d.c. conductivity and UV-Visible absorption behavior. Chapter 5 is the results and discussion of impedance and dielectric properties of SiCN ceramics. Concluding remarks are listed in Chapter 6.

CHAPTER TWO: LITERATURE REVIEW

Polymer-derived ceramics (PDCs) are a new class of high-temperature materials synthesized by thermal decomposition of polymeric precursors. The basic steps involved in PDC processing are [1]: (1) synthesis of polymer precursors, (2) cross-linking the precursors to form pre-ceramic network, (3) pyrolysis of the cross-linked precursors to form amorphous ceramics, and (4) annealing the ceramics at even higher temperatures to form crystalline ceramics, if needed. PDCs possess many advantages over conventional ceramics made from powder metallurgy based processing:

1) PDCs can be fabricated free of any additives at temperatures as low as 1000℃. Hence, the thermo-mechanical properties of these ceramics such as strength, oxidation and creep resistance at elevated temperatures will be greatly improved due to the low impurity level and the homogeneous element distribution [2].
2) The compositions and microstructures, thereby properties of PDCs can be controlled over a wide range by chemically modifying the precursors and/or by designing process conditions during the course of polymer-to-ceramic conversion [1].
3) The processing of PDCs also offers a simple & cost-efficient method to fabricate ceramic components/devices with unconventional structures, such as fibers, coatings, ceramic matrix composites (CMCs) and MEMS, which the powder-route cannot perform [1].

Based on so many advantages over conventional ceramics, PDCs will play a major role in the fields of the aforementioned applications. Thus, understanding the fundamental aspects of PDCs such as chemical and physical changes during the polymer-to-ceramic transformation process, their modified properties and the evolved structures will be very important for fabrication and application. In following sections, available knowledge of PDCs are briefly reviewed based on the literature that primarily focused on the electrical properties and their relationship with the microstructure of the PDCs, Si-(E)-C-N system in specific.

2.1 Processing of Polymer-Derived Ceramics

2.1.1 Synthesis of Polysilazanes

The preparation and characterization of polymeric precursors have been studied for a long time and a series of general empirical rules has been put forth [3, 4]. For example, the properties that an ideal pre-ceramic polymer should possess could be listed as follows [5], even they are sometimes incompatible:

1) Molecular weight should be sufficiently high to prevent any volatilization of oligomers.

2) A polymeric structure should contain cages or rings to decrease the volatile fragments resulting from backbone cleavage.
3) Desired viscoelastic properties (fusibility, malleability, or solubility) to apply the polymer in the desired shape before the pyrolytic process.
4) Presence of latent reactivity (functional substituent) to obtain thermosetting or curing properties.
5) Low organic group content to increase ceramic yield and avoid the production of undesired free carbon excess.

Usually, (poly) silazanes containing Si-N-Si units have been used as the starting precursors for Si/C/N ceramic systems because they could be obtained very easily from chlorosilanes and ammonia, amines, etc [1]. The starting precursors could be synthesized by following methods and the details were summarized by E. Kroke, et al [1]:

1) Ammonolysis of monochlorosilanes R_3SiCl, dichlorosilanes R_2SiCl_2 and trichlorosilanes $RSiCl_3$
2) Aminolysis of chlorosilanes.
3) Hydrazinolysis of chlorosilanes.
4) Silazanolysis of chlorosilanes.
5) Modification of silazanes.

2.1.2 Cross Linking of the Precursors

One of the most important steps in the preparation of ceramics by pyrolysis of polymer precursors is cross-linking. Cross-linking can transform the oligomeric silazanes into large molecules with highly interlocked backbones, which is required to avoid the evaporation of oligomers during pyrolysis [6] and give a high ceramic yield.

The effective cross-linking can be obtained by either thermally or chemically using radical initiators like peroxides or catalysts. Thermal cross-linking is preferred on consideration of the control of elemental and phase composition of the final ceramics because no additional elements are introduced to the polymer. Thermal cross-linking requires the presence of reactive functional groups such as vinyl or silyl groups in the precursors. The major cross-linking reactions involved in the pyrolyzing polysilazanes are a) hydrosilylation of vinyl groups, b) dehydrocoupling, c) transaminations, and d) vinyl polymerization [1]. The effects of the different functional groups on thermal cross-linking behavior of polymer precursors were systematically investigated by Choong Kwet Yive *et al.* [7]. They found the enhanced cross-linking reaction with an increasing number of active vinyl and Si-H groups. Based on their experimental results, the cross-linking activity can be arranged in the following order:

Hydrosilylation > dehydrocoupling > transaminations > vinyl group polymerization

The study on PUMVS-Ceraset by Seyferth and his co-workers [8] showed that the presence of Si-H and vinyl groups in Ceraset makes it possible to cross-link it at a relatively low temperature. The Ceraset solidifies mainly by the hydrosililylation reaction. Intense cross-linking results in a highly interconnected backbone structure that is infusible and easy to shape by powder processing.

2.1.3 Pyrolysis of Ceramics

The pyrolysis of polysilazane to ceramics process is a very complex process which will be discussed in two aspects including pyrolysis mechanism and composition changes.

The pyrolysis mechanism involved in the polymer-to-ceramic transformation is a very complex process and is not completely understood. By applying solid state NMR, TG/MS, TG/FTIR and other modern methods, some pyrolysis mechanisms of special precursors have been put forth [1, 9, 10]. One important feature of the pyrolysis mechanism is the weight loss during the process. The weight loss during pyrolysis was caused predominately by the evolution of oligomers at lower temperatures and by-product gases at higher temperatures. A three-stage weight loss was generally observed for the polysilazanes [10]. First, weight loss occurs at temperatures lower than 400℃ due to the evaporation of light molecular weight oligomers and transamination reaction. There is also a contribution from hydrosilylation reaction in case of precursors with reactive groups of Si-H and -CH=CH_2- .The second

weight loss comes from the loss of hydrocarbons such as CH_4, C_2H_6 and others in the temperature range of 400-750 ºC. Also, there is some dehydrogenative coupling with Si-H and N-H groups. Above 750 ºC, the weight loss is mainly due to hydrogen evolution. The exact temperature of gas evaporation changes with the different polymer structure and the degree of cross-linking. There is also some variability due to the heating rate and pyrolysis environment.

The elemental compositions are changed largely during the whole pyrolysis process depending on several factors such as chemical composition of the starting materials [11], pyrolysis environment [12, 13], and degree of cross-linking [14], heating rate and the reactive groups in the polymer precursors. For example [15], Table 1 lists the elemental compositions of the starting PUMVS precursor, the cross-linked, pyrolyzed and crystallized products obtained at the indicated temperatures. All these changes might influence the structures and properties of the final ceramics.

The chemical composition and phases of the silazane derived ceramics can also be evaluated using the ternary phase diagram. Figure 1 shows the composition of SiCN ceramics derived from polymer precursors. The stable phases SiC and Si_3N_4 are shown in the figure. The tie line joining Si_3N_4 and SiC separates the diagram into two important domains. The domain below the tie line shows there is an excess of silicon. The one above the line has an excess of carbon. Generally, the composition range lies within the triangle bound by SiC, Si_3N_4, and carbon. Thus, their composition can be expressed as $SiC_nSi_3N_4xC$. The ratio, *n*, is

a measure of the relative amounts of Si–N and Si–C bonds in the amorphous structure, while *x* measures the free-carbon atoms bonded to themselves.

Table 1: Chemical composition of the starting PUMVS polymer (1), the polymer cross-linked at 450 °C (2), the ceramics pyrolyzed at 1000 °C (3) and the ceramics annealed at 1700 °C (4). All the processing was conducted under argon atmosphere with an annealing time of 2 h [15]

Sample no.	Sample name	Composition (wt %)						Empirical formula
		Si	N	C	H	O	Total	
1	PUMVS	43.9	19.1	27.3	8.11	0.38	98.8	$SiN_{0.87}C_{1.45}H_{5.17}O_{0.01}$
2	CL-450	44.1	19.7	28.5	6.92	0.59	99.8	$SiN_{0.89}C_{1.51}H_{4.39}O_{0.02}$
3	Py-1000	55.3	22.6	20.3	＜0.01	0.76	98.96	$SiN_{0.82}C_{0.86}O_{0.02}$
4	Py-1700	67.0	5.26	26.0	＜0.01	1.5	98.3	$SiN_{0.16}C_{0.91}O_{0.04}$

2.1.4 Annealing Process of Ceramics

The thermal stability of polymer derived ceramics is the stability against chemical decomposition and crystallization. At high temperatures (above 1440 ºC), the amorphous Si/C/N ceramics will become unstable and transform to the thermal stable phases such as Si_3N_4 and SiC according to following reactions[16]:

$$Si_{3+X}C_{X+Y}N_4 \rightarrow Si_3N_4 + xSiC + yC \qquad (2.1)$$

$$Si_3N_4 + yC \rightarrow (1-y/3)\ Si_3N_4 + ySiC + (2/3y)\ N_2 \qquad (2.2)$$

$$Si_{3+X}C_{X+Y}N_4 \rightarrow (1-y/3)\ Si_3N_4 + (x+y)SiC + (2y/3)N_2 \qquad (2.3)$$

The excess carbon and nitrogen will also be formed during these processes. These reactions depend strongly on the nitrogen pressure and on the temperature.

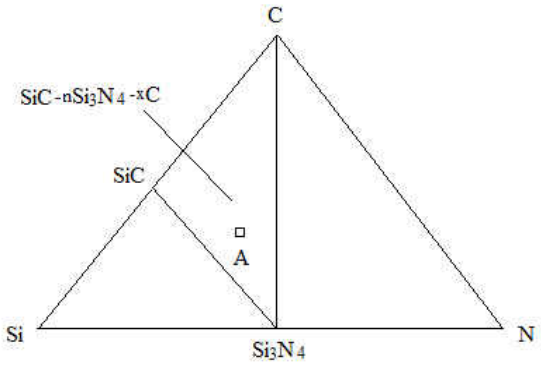

Figure 1: Composition diagram for Si–C–N system. A: amorphous SiCN pyrolyzed at 1000~1350 ºC [16]

2.2 Fabricating Route of Polymer-Derived Bulk Ceramics

Before the 1990s, polymer-derived ceramics were mainly prepared in the form of materials of smaller dimensions such as fibers, coatings or powders. Since 1991， four new methods have been developed to fabricate dense and crack-free ceramics. In this section, these techniques are briefly reviewed.

2.2.1 Cold/Warm-Press Powder Route

In 1991, Riedel et al. developed a process which produces dense Si/C/N bulk ceramics [17]. This method involves cross-linking of polysilazanes into infusible solids, milling the cross-linked silazanes into fine powders followed by shaping green bodies, and pyrolyzing the compacts around 1000ºC. The unique feature of this novel process is the direct transformation from highly cross-linked polymer networks to dense monolithic Si/C/N bodies

by pyrolysis without sintering aids. The key steps to this process are the cross-linking process and the compaction process. For cross-linking process, an optimal temperature is needed to obtain the high degree of cross-linking and the good plasticity of the cross-linked polymer. For compaction process, two compact methods can be used: cold pressing and warm pressing. Early attempts to prepare polymer compacts for bulk pyrolysis used isostatic or uniaxial cold pressing leading to densities of the compacts of 84%. The final bulk density of the Si/C/N ceramics after pyrolysis at 1000 ºC was 93%. Recently, warm-pressing methods have been used by Seitz and Bill [18]. The dense green bodies with porosity of 7.5% were obtained by this compaction technique and Si/C/N ceramics with a relative density of 97% were obtained after pyrolysis at 1000 ºC.

2.2.2 The Active/Inactive Filler Route

In this route, liquid or solid polymer precursors are mixed with active or inactive filler powders, followed by shaping and pyrolysis. The active fillers may react with the silazane, its decomposition products, or active atmospheres during pyrolysis to form carbide, nitride, carbonitride, oxide phases, which in turn can reduce the shrinkage and the amount of volatile side products. By this process, zero shrinkage after pyrolysis could be achieved allowing a near net shape fabrication of ceramic composite materials. However, the pyrolyzed bodies were not fully densified with an appreciable amount of residual open porosity. A similar

effect may be gained by passive fillers which do not react with the silazane matrix, but decrease shrinkage and formation of volatiles due to a reduction of the total polymer amount. [19, 20]

2.2.3 Pressure-Assistance Route

A novel pressure-assisted pyrolysis process has been recently developed to synthesize fully dense bulk polymer-derived ceramics without pores and cracks [21]. In this process, the cross-linked polymer precursor is pyrolyzed in the hot-isostatic press furnace (HIP) at low ramping rate in order to release the gaseous by-products without breaking the structure. The applied isostatic pressure prevented the formation of pores and cracks during pyrolysis.

2.2.4 Photo-Catalyst Route

Recently, a new photo-catalyst route has been developed in our research group at UCF. The integrated fabrication process consists of the following steps as shown in Figure 2: (1) addition of a photoinitiator to the precursor, (2) cross linking the precursor into solid polymeric samples, (3) pyrolysising to convert the polymeric samples into ceramic, and (4) annealing the ceramic samples above 1000 ºC. By this route, we got fully dense ceramics samples with excellent properties. The detail of the process will be introduced in chapter 3.

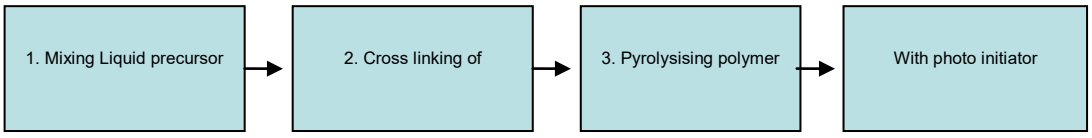

Figure 2: Schematic representation of photo-catalyst route

2.3 Structure of Polymer-Derived Amorphous Bulk Ceramics

The structure of polymer-derived amorphous ceramics has been studied for a long time with different methods such as Nuclear Magnetic Resonance (NMR), Electron Paramagnetic Resonance (EPR), Neutron scattering (NS), Electron Energy-Loss Spectroscopy (EELS), Small-Angle X-ray Scattering (SXAS) and Raman Spectroscopy, etc. [22, 23, 24, 25, 26, 27, 28, 29, 30]. G. Gregori[31] et al. found chemical bonds of Si-Si, Si-N, Si-C and C-C but no C-N bond in the amorphous SiCN samples when they studied the microstructure of the materials with Neutron scattering and EELS. According to NS data, they concluded that the amorphous SiCN bulk consists of two main phases: (i) a Si–C–N network and (ii) a free carbon phase. Other researchers [2, 15, 32] also arrived at the same conclusion when they performed the structural characterization of SiCN ceramics derived from polymeric precursors using NMR. It was reported that the ^{29}Si NMR spectrum exhibited a broad resonance peak centered at around 31 ppm at temperature range from 900 to 1400 ºC [29]. The simulation of this peak revealed three main structural components including SiC_2N_2, $SiCN_3$ and SiN_4, which indicates that a ternary amorphous Si–C–N phase is obtained at these temperatures. In addition, between 700º and 800 ºC, a broad resonance peak which was

assigned to free carbon is present. This result suggests that a free carbon phase started to form. In the amorphous ceramic above 1000 ºC, the carbon was found to exist in one main fraction, namely as graphite like domains. Based on these results, the microstructure of SiCN amorphous materials can be generally described as a random Si–C–N network composed of amorphous tetrahedral mixed units, $[SiC_xN_{(4-x)}]$ $(1 \leq x \leq 4)$, with excess amorphous carbon.

The spatial distribution of these two structural units in amorphous SiCN is important in deciding the properties of these materials. However, the details of these distributions have not been studied thoroughly. Jens Cordelair et al. [33] proposed two possible domain distribution models for amorphous PDCs when they studied the structure transitions in polysiloxane derived Si-O-C ceramics (figure 3), which may also be used in Si-C-N system.

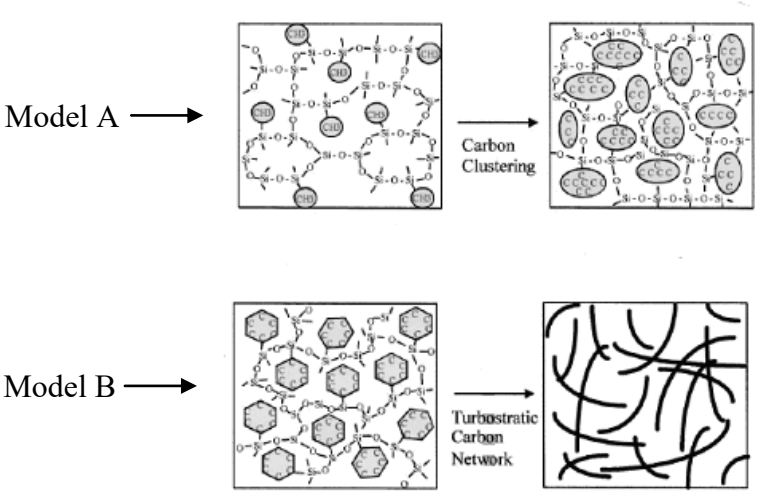

Figure 3: Model of carbon redistribution reactions during pyrolysis in (bottom) PMS and (top) PPS derived ceramic residue [33].

In model A, the domains in amorphous ceramics (annealed at temperature lower than 1400 ºC) consist of a discontinuous dispersion of sp2 carbon embedded in a continuous phase of silica. In this instance the size of the nano-domains will be determined by the ‘‘free’’ carbon cluster. In model B, the carbon cluster became a cage-like network of sp2 graphene carbon that forms an interconnected network, in which, the domains of clusters of silica tetrahedral were embedded. Although both of these two models are consistent with NMR results [33], A. Saha et al [34, 35] argued that, compared to model A, the model B is consistent with other phenomenological properties better like quite remarkable creep and viscoelastic behavior of SiCO. In model B, the domain size predicted by a simple geometrical model developed by these researchers are consistent with experimental domain size, ranging from 1 to 5 nm, measured by small-angle X-ray scattering (SAXS). In addition, high resistance to crystallization of amorphous ceramics even at temperatures as high as 1400 ºC can be explained by model B in geometric and thermodynamic aspects. On one hand, the nucleation of crystallites of silica requires the growth of embryos of a critical size of few nanometers. Forming such a large nucleus requires diffusion of the silica over distances much larger than the size of the existing silica domains, leading to a very low probability of reaching a nucleus of critical size in a laboratory time scale. On the other hand, in model B, the calculated enthalpy of formation of the amorphous phase is significantly lower than that of the isocompositional mixture of crystalline SiO_2, SiC, and C. Because the entropy of the

amorphous phase must be greater than that of crystalline phases, it is inferred that the amorphous phase of SiCO possesses lower free energy with respect to the crystalline phases.

The formation of graphitic-like carbon phase and its structural rearrangements have important influence on the electronic properties of PDCs [2, 36, 37, 38, 39, 40, 41]. However, no excess carbon phase could be imaged by HRTEM even annealing the samples at temperatures as high as 1400 ºC, no matter which way the carbon exists in ceramics: homogeneous distribution of carbon clusters or a network of graphitic-like lamellae of a few atom layers. Two reasons might explain this phenomena: a) the carbon phase is not well ordered (amorphous-like) and hence gives a similar projected potential as the surrounding amorphous SiCN and/or, b) the ordered carbon regions are considerably smaller than the foil thickness (10–20 nm) illuminated by the electron beam.

2.4 General Thermo-Mechanical Properties of PDCs

Generally, the PDCs products exhibited excellent properties including: 1) high resistance to high temperature thermal decomposition (figure 4) [41], 2) high creep resistance (figure 5) [42, 43], 3) high resistance to oxidation and hot-corrosion (figure 6, 7, 8) [44].

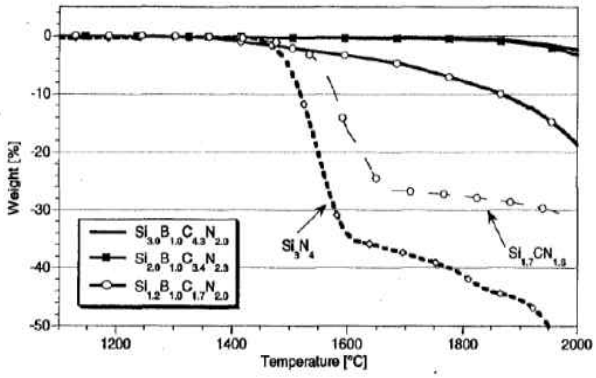

Figure 4: TGA of polymer-derived SiCN, SiBCN and commercial silicon nitride in 0.1 MPa. Heating at the rate of 5 K/min, suggesting SiBCN can be stable up to 1800 ºC [41]

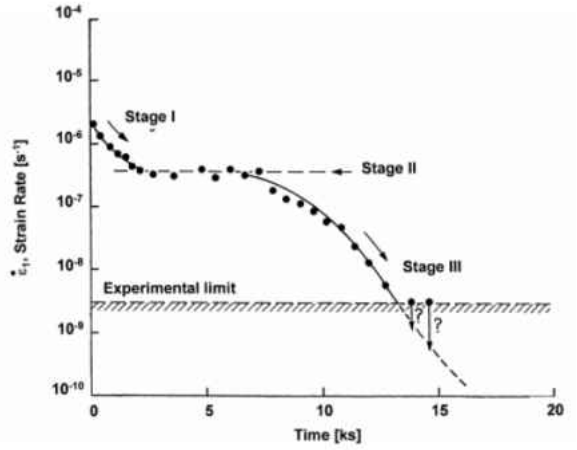

Figure 5: Change of the strain rate in Si/(B)/C/N vs. time showing three different stages [42,43].

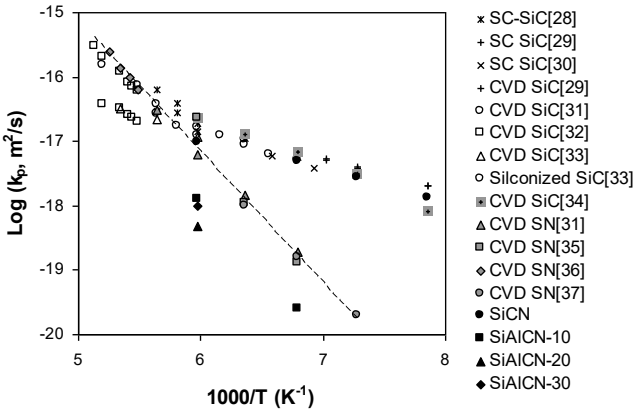

Figure 6: Plot of log parabolic rate constants as a function of reciprocal of temperatures for the PDCs SiAlCN samples and other ceramics [44].

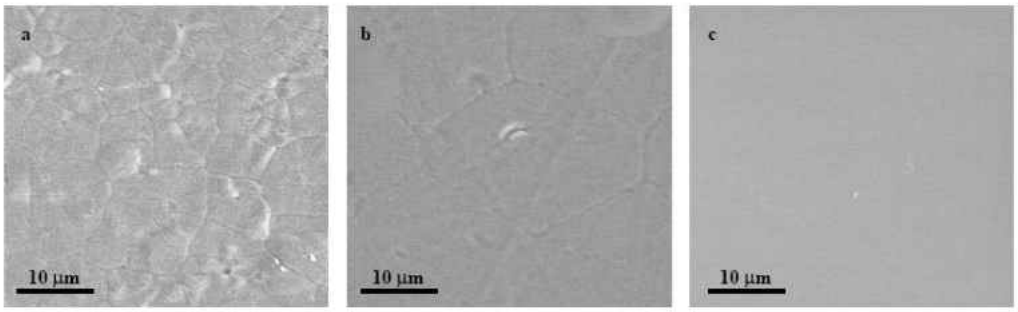

Figure 7: SEM images of the surfaces of (a) SiCN, (b) SiAlCN-07, and (c) SiAlCN-14 after annealing at 1200 ºC for 50 hrs in NaCl environments. SiAlCN-14 shows significant resistance to alkali corrosion without detectable corrosion [44]

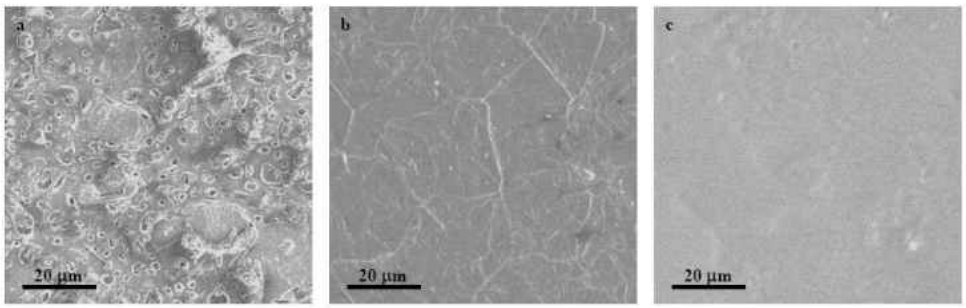

Figure 8: SEM images of the surfaces of (a) SiCN, (b) SiAlCN-07, and (c) SiAlCN -14 after annealing in 100% water vapor of 1 atmosphere pressure at 1200 ºC for 50 hrs Again, SiAlCN-14 shows excellent resistance to water vapor corrosion without detectable corrosion [44].

PDCs also possess excellent physical and mechanical properties [42]. Table 2 shows some physical-mechanical properties of PDC as compared to the other ceramics (SiC, Si_3N_4). Due to the absence of grain boundary phases, it is expected that such excellent mechanical behavior can be retained at high temperatures. These excellent thermo-mechanical properties suggest that the PDCs are suitable for high temperature applications.

Table 2: Properties of polymer derived SiCN and other high temperature materials

Properties	PDC-SiCN	SiC	Si_3N_4
Density (g/cm^3)	2.3	3.17	3.19
Young's modulus (GPa)	90-150	400	320
CTE ($x10^{-6}/K$)	3	3.8	2.5
Poisson's Ratio	0.18	0.14	0.24
Strength (MPa)	~1000	420	700
Hardness (GPa)	20	30	28
Thermal Shock FOM*	~3000	350	880

* Thermal shock FOM = strength/ (E-modulus. CTE)

2.5 Electrical Properties of Polymer-Derived Ceramics

2.5.1 D.C - Conductivity of Polymer-Derived Ceramics

2.5.1.1 D.C - Conductivity of SiCN Ceramics Annealed at Different Temperature

In general, all investigated amorphous SiCN-ceramics annealed at temperature range from 1000 to 1300 ºC showed semi-conducting behavior and an increase of the d.c-conductivity with increasing annealing temperature [2, 15, 36, 37, 38, 39, 40]. Haluschka [37] et al. attributed this phenomenon to the loss of residual hydrogen with increasing annealing temperature, thereby increasing the sp2-/sp3-ratio of the carbon atoms and hence the energy barrier for the transport of charge carriers was lowered, leading to the increase in the electrical conductivity. It was believed that the tunneling of large polarons was the main

transport mechanism in this regime. Hermann [39] et al. also reported the same results when they studied the structure and electronic transport properties of pristine and boron-doped SiCN ceramics. In addition, they found that the as-pyrolyzed SiBCN ceramics have significantly higher conductivity ($\sigma=10^{-8}\ \Omega^{-1}\cdot cm^{-1}$ at room temperature) than that of SiCN ceramics ($\sigma=10^{-12}\ \Omega^{-1}\cdot cm^{-1}$), i.e. an increase of 4 orders of magnitude.

2.5.1.2 The Temperature Dependence of the D.C.-Conductivity of SiCN Ceramics

The Relationship between d.c conductivity and measuring temperature has also been studied by some researchers [2, 39]. Generally, the conductivity of pyrolyzed and annealed samples follows the Mott law or Arrhenius law with measuring temperature. Hermann [39] found that the conductivity of both as-pyrolyzed and annealed samples, pristine and boron-doped SiCN ceramics heat-treated at temperature range from 1000~1550 ºC, exhibited a linear behavior when plotted against $T^{1/4}$ (Mott low) but nonlinear behavior when plotted with T^{-1}. Linear behavior of conductivity with $T^{1/4}$ indicated that the electrical transport properties are a typical of three-dimensional variable range hopping (3D VRH) (Fig. 9, 10), indicating that these ceramics are highly disordered with unsaturated bonds resulting in a high density of localized states in the mobility gap. Nonlinear behavior of the conductivity with inverse temperature indicates that conductivity is due to hopping of carriers between localized states in the mobility gap rather than due to band-to-band transition.

In comparison to the results reported by Hermann, Trassl et al., [2] argued that the pyrolysis and annealing temperature have a profound influence on the temperature dependence of the d.c.-conductivity of the SiCxNyHz ceramics. It was concluded that at lower pyrolysis temperatures (T_p <1200 ºC), the temperature dependence of the d.c.-conductivity of the SiCxNyHz ceramics could be explained by Mott law (eq. 2.4). At higher pyrolysis temperatures (1200 ºC <T_P <1400 ºC), the temperature dependence of the d.c.conductivity follows an Arrhenius law (eq. 2.5).

$$\sigma_{dc}(T) = \sigma_0 \times Exp\left[-\left(\frac{T_0}{T}\right)^{\frac{1}{4}}\right] \qquad (2.4)$$

$$\sigma_{dc}(T) = \sigma_0 \times Exp\left[-\left(\frac{\Delta E}{kT}\right)\right] \qquad (2.5)$$

Where, σ_{dc} (T) is the electrical conductivity of samples pyrolyzed at temperature T, σ_0 is constant, k is Boltzmann constant, Δ E is activation energy (energy gap between Fermi level and conducting band), T is temperature.

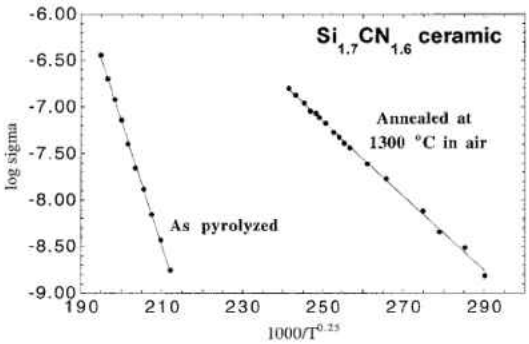

Figure 9: Conductivity variation with temperature for as-pyrolyzed and high-temperature annealed SiCN ceramics showing that a three dimensional VRH mechanism is operative. Conductivity is increased drastically by annealing treatments [39].

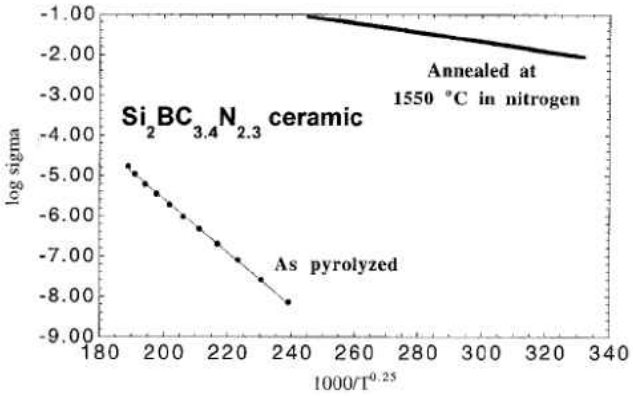

Figure 10: Conductivity variation with temperature for as-pyrolyzed and high-temperature annealed SiBCN ceramics showing that a three dimensional VRH mechanism is operative. The SiBCN ceramics show higher conductivity than SiCN ceramics. Conductivity is increased drastically by annealing treatments [39].

2.5.2 A.C- Conductivity of Polymer-Derived Ceramics

Haluschka [37, 41] et al., also studied the relationship between a.c. conductivity and frequency ν of SiCN ceramics. In accordance with a main feature of amorphous semiconductors the a.c. conductivity increased with frequency ν (fig. 11) approximated by a power-law with the frequency exponent s≤1 [45]

$$\sigma(\nu) = A*\nu^{s} \qquad (2.6)$$

The origin of this behavior is related to relaxation caused by hopping or tunneling processes. By plotting s vs. the measuring temperature, the transport mechanism responsible for the a.c.-conductivity could be derived. The minimum of s (T), which is a typical feature of large polaron tunneling, is shifted towards lower temperatures with increasing annealing temperature. T_{min} decreased with increasing annealing temperature T_a (Fig. 12) indicating

enhanced transfer of polarons. This is consistent with the increasing a.c.-conductivity with increasing annealing temperature.

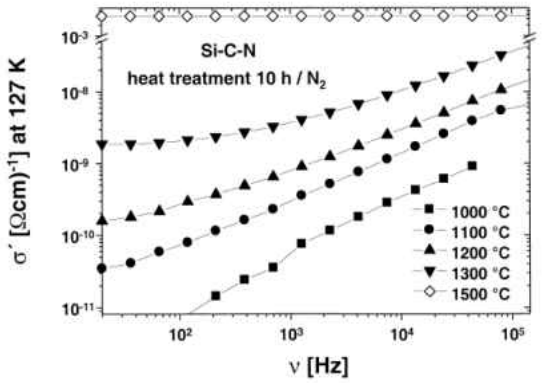

Figure 11: Real part of the a.c-conductivity σ' depending on the frequency ν and the annealing temperature T_a [45].

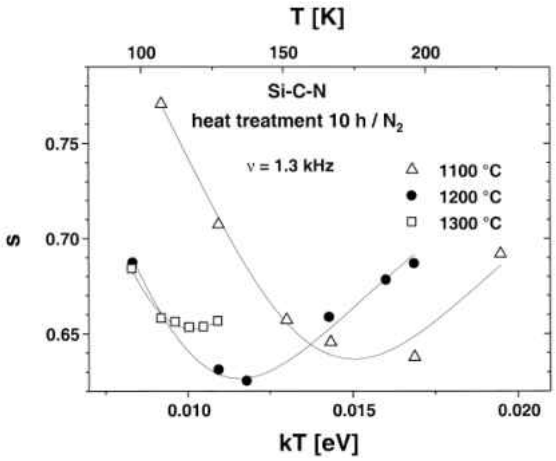

Figure 12: Frequency exponent s depending on the measuring temperature T and the annealing temperature T_a (fitting curves are represented by lines) [45].

2.6 Electronic Behavior of Amorphous Semiconductor

Previous studies have shown that SiCN polymer derived ceramics is one kind of amorphous semiconductors. So its electronic properties could be interpreted by conduction

mechanism of amorphous semiconductors. Amorphous semiconductors are materials which has short-range periodic ordering of constituent atoms. The electrical properties of this kind of materials can be changed and controlled not only by the addition of small amounts of another material but by external stimuli, such as temperature change, electric field, and incident radiation, etc. For amorphous semiconductors, experimental data of electrical transport properties can be properly interpreted by several electronic structure models including the Cohen– Fritzsche-Ovshinsky model, Small-Polaron model and the Davis-Mott model. These models used the concept of localized states which was proposed by Mott [46]. The Davis-Mott model is briefly introduced below.

Based on Anderson's theory [47], Mott argued that the spatial fluctuations in the potential caused by the configurationally disorder in amorphous materials may lead to the formation of localized states, which do not occupy all the different energies in the band, but form a tail above and below the normal band. Mott postulated furthermore that there should be a sharp boundary between the energy ranges of extended and localized states. At the transition from extended to localized state, the mobility drops by several orders of magnitude producing a mobility edge. Indeed, the concept of localized states implies that the mobility is zero at T = 0K. The schematic diagram of Davis-Mott energy band model is shown in figure 13(a). Here, E_C and E_V represent the mobility edge of extended state of conduction and valence band, respectively. E_F is Fermi energy while E_B and E_A are the minimum of band tail.

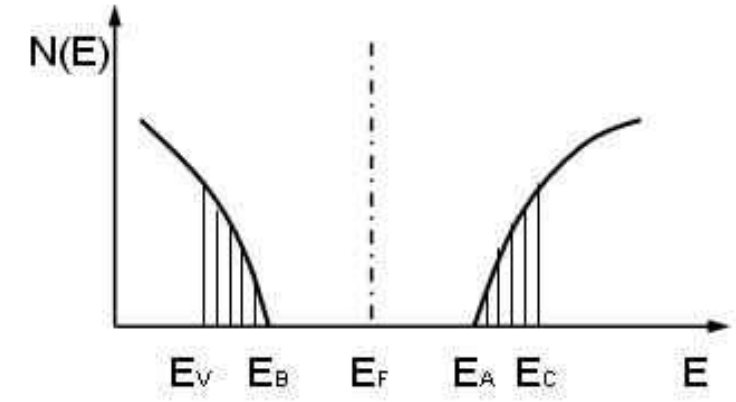

(a)

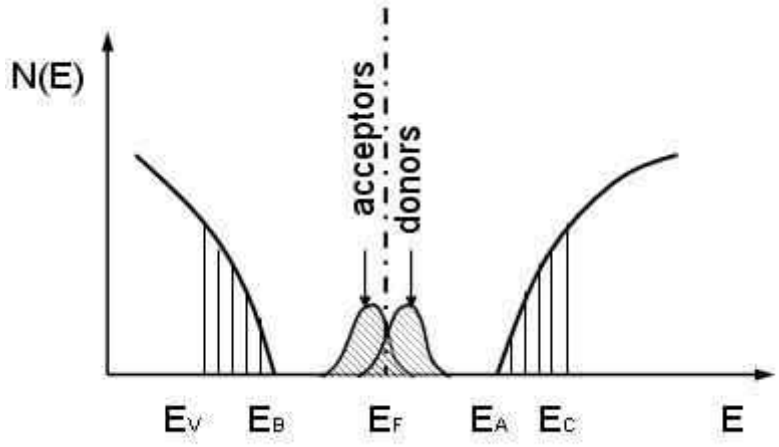

(b)

Figure 13: Schematic diagrams for amorphous semiconductor (a) the Davis-Mott model, (b) modified Davis-Mott model [47]

However, this model is based on the "perfect amorphous" structure which does not have any short-range defect. This is not going to happen in real materials. Then Mott proposed furthermore that there is a band of compensated levels near the middle of the gap originating from defects in the random network, e.g., dangling bonds, vacancies, etc. Figure 13 (b) sketches the modified Davis-Mott model. The center band may be split into a donor

and an acceptor band, which will pin the Fermi level. The interval between the energies E_C and E_V acts as a pseudo gap and is defined as the mobility gap.

On the basis of the modified Davis-Mott model, there can be four processes leading to conduction in amorphous semiconductors. Their relative contribution to the total conductivity will predominate in different temperature regions. At very low temperatures, conduction can occur by variable range hopping mechanism in localized states at the Fermi level. At higher temperature, conduction occurs by phonon- assisted tunneling between states at the Fermi level. A higher temperature, charge carriers are exited into the localized states of the band tails, carriers in these localized states can take part in the electric charge transport only by hopping. At still higher temperature, carriers are excited across the mobility edge into the extended states. These four conductions are introduced here:

2.6.1 Conduction in Variable Range Hopping:

As the temperature is very low, the number and energy of phonons decrease, and more energetic phonon-assisted hops will progressively become less favorable. Carriers will tend to hop to larger distances in order to find sites which lie energetically closer than the nearest neighbors. This mechanism is the so-called variable range hopping. Mott's treatment of variable range hopping leads to a temperature dependence for the conductivity of the form:

$$\sigma_1 = \sigma_{10} \exp\left[-\left(\frac{T_0}{T}\right)^{1/4}\right] \qquad (2.7)$$

Where,

$$T_0 = 2.1\left\{\frac{\alpha^3}{[kN(E_F)]}\right\}, \qquad (2.8)$$

$$\sigma_{10} = \frac{1}{6} e^2 \nu_{ph} N(E_F) R^2 \qquad (2.9)$$

$$R = \left[\frac{9}{8}\pi\alpha kTN(E_F)\right]^{1/4} \qquad (2.10)$$

There have been several more derivations of the conductivity formula for variable range hopping. In general, the $T^{-1/4}$ relationship remains unchanged, but slightly different values were found for the numerical factor in T_0.

2.6.2 Conduction in Localized States at the Fermi Energy (Tunneling Process):

If the Fermi energy level lies in a band of localized states, as predicted by the Davis - Mott model, the carriers can move between the states via a phonon-assisted tunneling process. This is the transport analogous to impurity conduction observed in heavily doped and highly compensated semiconductors at low temperature. An estimate for the temperature dependence of the hopping conductivity at E_F has been given by Mott [48]. The conductivity is expressed by:

$$\sigma_2 = \sigma_{20} \exp\left[-\frac{W_2}{kT}\right] \qquad (2.11)$$

Where, W_2 is phonon energy.

2.6.3 Conduction in Band Tails (Hopping Conduction):

If the wave functions are localized, so that σ (E) = 0, conduction can only occur by thermally activated hopping. Every time, an electron moves from one localized state to another, it will exchange energy with a photon. Generally, the conductivity in band tails can be expressed as equation 2.12:

$$\sigma_3 = \sigma_{30} \exp\left[-\frac{E_A - E_F + W_3}{kT}\right] \qquad (2.12)$$

Where, W_3 is activation energy.

2.6.4 Extended State Conduction:

When electron hops from deep defect band like localized state in Fermi energy level and band tail to extended state, extended state conduction will happen. The relationship of dc conductivity with temperature in extended state follows a simple exponential law:

$$\sigma_4 = \sigma_{40} \exp\left[-\frac{E_C - E_F}{kT}\right] \qquad (2.13)$$

2.6.5 The Total D.c Conductivity of Amorphous Semiconductor with Temperature

So the relationship between the total conductivity of amorphous semiconductors and temperature can be described as following equation (2.14) and drawn as Figure 14:

$$\sigma = \sigma_1 + \sigma_2 + \sigma_3 + \sigma_4 = \sigma_{10} \exp\left[-\left(\frac{T_0}{T}\right)^{1/4}\right] + \sigma_{20} \exp\left[-\frac{W_2}{kT}\right] + \sigma_{30} \exp\left[-\frac{E_A - E_F + W_3}{kT}\right] + \sigma_{40} \exp\left[-\frac{E_C - E_F}{kT}\right] \quad (2.14)$$

Where,

σ_1: Conduction in Variable range hopping.

σ_2: Conduction in Localized States at the Fermi Energy

σ_3: Conduction in Band Tails

σ_4: Extended State Conduction

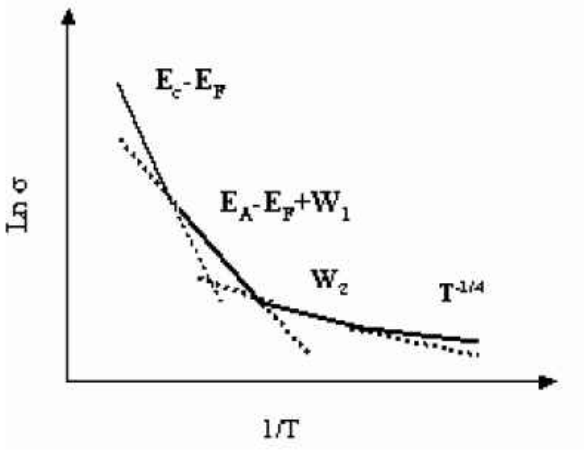

Figure 14: The relationship of DC conductivity with temperature

2.7 Characterization Methods Used in Polymer Derived Ceramics

2.7.1 Raman Spectroscopy

2.7.1.1 Basic Theory of Raman Spectroscopy

Raman spectroscopy is a spectroscopic technique used in condensed matter physics and chemistry to study vibrational, rotational, and other low-frequency modes in a system. It relies on inelastic scattering, or Raman scattering, of monochromatic light, usually from a laser in the visible, near infrared, or near ultraviolet range. The basic theory of Raman scattering is shown in figure 15 [49].

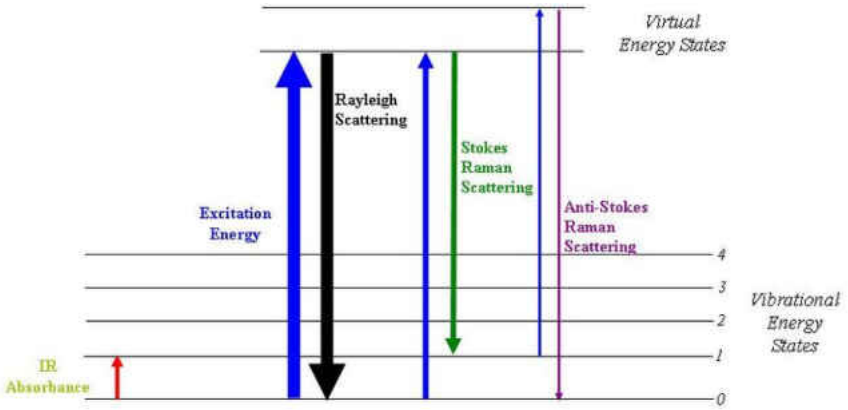

Figure 15: Energy level diagram shows the states involved in Raman signal. The line thickness is roughly proportional to the signal strength from the different transitions [49]

The Raman Effect occurs when light impinges upon a molecule and interacts with the electron cloud of the bonds of that molecule. The incident photon excites the molecule into a virtual state. For the spontaneous Raman Effect, the molecule will be excited from the ground state to a virtual energy state, and relax into a vibrational excited state, which generates Stokes Raman scattering. If the molecule was already in an elevated vibrational energy state, the Raman scattering is then called anti-Stokes Raman scattering. The intensity of anti-Stokes Raman scattering is much weaker than that of Stokes Raman scattering because there are typically more phonons in the ground state, due to the Maxwell-Boltzmann distribution.

The laser light interacts with phonons or other excitations in the system, resulting in the energy of the laser photons being shifted up or down. The shift in energy gives information about the phonon modes in the system.

2.7.1.2 Raman Spectra of Different Forms of Carbon

Raman spectroscopy is a standard nondestructive tool and one of the most sensitive methods for the characterization of the different modifications of carbon. As a new studying method, laser Raman spectroscopy has been used in field of various carbon materials for about 40 years started by Tuinstra and Koenig [50] in 1970s.

The carbon atom has four valence orbits, which can hybridize to form sp1, sp2 and sp3 orbital combinations. The sp1 orbital forms linear structures as found in white carbon.

The sp2 orbital forms planar structures with 3-fold symmetry at the carbon atom, and is found in aromatic molecules and in crystalline graphite. The sp3 orbital forms the basis for 3-dimensional, tetrahedrally bonded carbon as in methane (CH_4) and in diamond. The most well-known forms of elemental carbon found in nature are graphite and diamond. In recent years exotic sp2 forms known as Fullerenes, and including the carbon nanotubes, have also drawn interest.

The Raman spectra of these carbon materials are very different due to their different atomic structures, which are shown in figure 16 [51].

Diamond (D) is formed by an infinite extension of sp3 carbon-carbon bonds and in single crystal diamond, the Raman line appears at 1332 cm^{-1}, which is the characterization Raman spectrum for diamond.

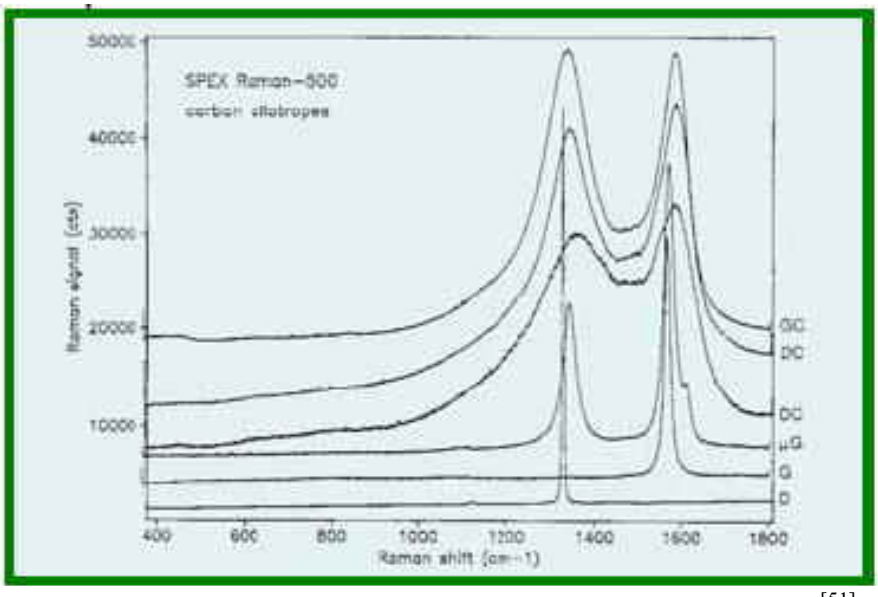

Figure 16: Raman spectra of different modifications of carbon [51]

Graphite (G) is formed from stacks of infinitely extended planes of fused aromatic rings. The π electrons in the planes provide for high electrical conductivity and a 0eV band gap. The graphite first order phonon at about 1580 cm-1 which is fairly sharp, although not as sharp as that of diamond. This line has been documented to move with stress and temperature. When the long-range order of the graphite lattice is disrupted, a second line appears at about 1360 cm-1. The intensity of the peak at 1360 cm-1 scaled with the size of the crystal.

Material with shorter range order will be denoted microcrystalline graphite (μG). A typical spectrum is shown in Figure 1.The relative peak intensities of these two lines at 1580 and 1360 cm-1, denoted respectively as G and D lines in the literature (graphite and defect), can vary enormously.

The Raman spectrum of many carbon materials exhibits such extensive broadening and overlap between the two bands that only band fitting would permit appropriate use of the data. Carbons showing this behavior will be denoted disordered carbon (DC). In addition, it has been shown that some carbon films require a second defect band at about 1500 cm-1 to flatten the residual of the band-fitted Raman spectra. These authors attribute this band to the presence of interstitial defects between the graphitic layers or between structural units in the layers. In contrast the D band at 1360 cm-1 is attributed to in-plane defects between basic structural units.

When band-broadening and overlap in carbon films is so extensive that separate bands are not discernible before the band-fit, the material is called "diamond-like carbon" (DLC). The peak at 1560 cm-1 of DLC is from sp2 band which is trapped in sp3 tetragonal net.

A material called "Glassy Carbon" (GC) has the intensity ratio of the D and G bands reversed (D band higher), with the bands fairly sharp. Ironically this material is composed of highly crystalline regions, but with very small dimensions.

Appearance of D and G band is the most famous feature in Raman spectra of Carbon materials. The peak position, peak width, and peak intensity of these two bands can be used to study the various carbon statuses like ordering and defect, residual stress, etc. In addition, the intensity ratio of I_D/I_G can be used to calculate the size of carbon cluster according to equation which was reported by Tuinstra and Koenig [50] for crystalline carbon and more recently by Ferrari and Robertson [52] in the case of amorphous carbon.

$$\frac{Isp3}{Isp2} = \frac{C}{Ls} \qquad (2.15)$$

Where, Ls is the laterals size of carbon cluster, C is a constant whose value depends on the laser wavelength (532 nm) and here corresponds to about 49.5 Å [50,52,53,54].

The Raman spectroscope that was used in our study was Renishaw inVia Raman microscopy (Renishaw Inc., Hoffman Estates, IL), employing the 532 nm line of Si laser and a sensitive Peltier-cooled couple charged device (CCD) detector.

Figure 17: Renishaw inVia Raman microscope

2.7.2 Electron Paramagnetic Resonance

Electron paramagnetic resonance (EPR), also known as electron spin resonance (ESR) is one kind of resonant absorption spectrum arises from transition of unpaired electron in paramagnetic species from one energy level to other energy level in the presence of a strong magnetic field. EPR spectroscopy can specifically be used in studying chemical species that have one or more unpaired electrons, such as organic and inorganic free radicals or inorganic complexes possessing a transition metal ion.

Every electron has a magnetic moment and spin quantum number s = 1/2, with magnetic components $m_s = +1/2$ and $m_s = -1/2$. In the presence of an external magnetic field with strength B_0, the electron's magnetic moment aligns itself in only two orientations, i.e., two spin states, either parallel ($m_s = -1/2$) or antiparallel ($m_s = +1/2$) to the field. Each alignment has a specific energy and the energy difference between these two spin states is ΔE

(known as the Zeeman splitting). When an electromagnetic radiation, with a frequency corresponding to the energy difference between these two spin states, is set up perpendicularly to the magnetic field, the unpaired electron can be transited between these two energy states and EPR absorption spectrum can be aroused.

The basic equation for an energy level transition (resonance absorption) for an unpaired electron is:

$$\Delta E = h\nu = gBH$$

Where,

ΔE = the energy difference between the two energy states

h = Plank's constant

ν = frequency of electromagnetic radiation

g = g factor

B = Bohr magneton. In EPR spectroscopy, the Bohr magneton is usually expressed as 9.274×10^{-28} J/G. (10,000 G = 1 Tesla)

H = Resonance magnetic field

This equation implies that the splitting of the energy levels is directly proportional to the magnetic field's strength, as shown in the diagram as Figure 18 [55]:

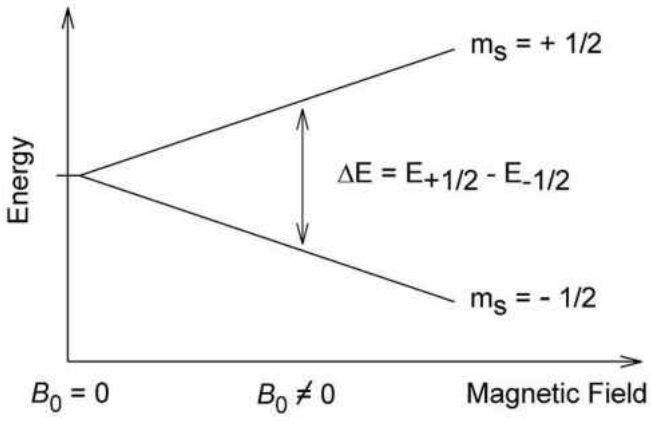

Figure 18: An energy level diagram for EPR resonance absorption [55]

In principle, EPR spectra can be generated by either varying the photon frequency incident on a sample while holding the magnetic field constant, or doing the reverse. In practice, it is usually the frequency which is kept fixed. A collection of paramagnetic centers, such as free radicals, is exposed to microwaves at a fixed frequency. By increasing an external magnetic field, the gap between the $m_s = +1/2$ and $m_s = -1/2$ energy states is widened until it matches the energy of the microwaves, as represented by the double-arrow in the diagram above. At this point the unpaired electrons can move between their two spin states. Since there typically are more electrons in the lower state, due to the Maxwell-Boltzmann distribution, there is a net absorption of energy. This absorption is detected by an EPR spectrometer, and after appropriate amplification, then converted and displayed as the first or second derivative of the absorption field.

Absorption resonance spectra are characterized by their g factor, line shape, linewidth and spins intensity. The details of these parameters are shown in following paragraphs:

1. g-factor:

Knowledge of the *g*-factor can give information about a paramagnetic center's electronic structure. An unpaired electron responds not only to a spectrometer's applied magnetic field B_0, but also to any local magnetic fields of atoms or molecules. When the unpaired electron gains or loses angular momentum through spin-orbit coupling, the ratio of the unpaired electron's spin magnetic moment to its angular momentum will differ from the free electron value. Then the g does not equal g_e. The different g values give information about the nature of the atomic or molecular orbital containing the unpaired electron, by which materials with different structure can be identified. For example, carbon with different structures like glassy graphite, planar graphite, turbostratic carbon, and multiwall nanotube phase have different g-values as 2.0027, 2.018, 2.02, and 2.012, respectively [56].

2. Line shape

Generally, the EPR spectrum gives symmetry Gaussian shape or Lorentzian shape. However, interactions of unpaired electron with its environment will influence the shape of the EPR spectral line. On one hand, dipolar interaction, broadening sources, etc. will broaden the spectrum. On the other hand, factors like spin exchange interaction, high spins intensity,

faster electron motions, etc., will narrow the line width. In addition, the line shape also can be changed from symmetry into asymmetry due to either the presence o conductive metallic like components with in matrix [36] or anisotropy in the *g*-tensor for the unpaired spins, or the presence of spins of two or three types with slightly different *g*-values and linewidths [57].

EPR spectrum does not always consist of a single line. When a single unpaired electron in a magnetic field interacts with nearby nuclear spins, additional energy states will be allowed and the spectrum splits into two or more lines, which produce hyperfine structure in the spectrum. In such cases, the spacing between the EPR spectral lines indicates the degree of interaction between the unpaired electron and the perturbing nuclei. The hyperfine coupling constant (units of G or MHz) of a nucleus is directly related to the spectral line spacing and, in the simplest cases, is essentially the spacing itself. The absolute position of the spectrum is expressed by the *g* value and the hyperfine coupling constant gives the detail information of electronic structure. In polymer chemistry, usually the hyperfine structure of the ESR spectrum provides more important information about the radical than does the *g* value, because most radicals detected are carbon centered radicals which have g~2.0027 [56, 58].

3. Line width

The width of the EPR signal reflects the interactions of the spins with their

environment. In the case of mobile spins, the motion characteristics, such as spin mobility and dimensionality, are also parameters which play a major role in determining the EPR line linewidth. Thus, EPR has been used intensively as a technique for investigating the properties of mobile spins. The linewidth is expected to originate from the competition of broadening sources, hyperfine coupling, dipole spin-spin interactions and narrowing processes, which reflect the spin motion. According to the well-known process of motional narrowing, the observation of a narrow line could be the signature of a fast motion.

In addition, EPR linewidth of some materials is expected to show the corresponding behavior to the electrical resistivity ρ qualitatively, when the ESR linewidth is dominated by the Elliott mechanism [59]. The EPR linewidth also is strongly temperature dependent and can be used to calculate the value of exchange interactions [56].

4. Spins intensity

Spin intensity can be used to estimate dangling bonds (unpaired electrons) which is related to conduction of materials, especially for amorphous semiconductors. Spin intensity can be calculated by comparing the area of the EPR spectrum with that of reference materials whose spin density is already known.

CHAPTER THREE: STRUCTURE OF POLYMER DERIVED SiCN CERAMICS

In this chapter, the fabrication process to achieve fully dense SiCN ceramics and the structural evolution during pyrolysis process that was studied by various characterization methods are discussed. XRD results confirmed that the SiCN ceramics, after annealing for 4 h in nitrogen at a wide temperature range of 1000 ~ 1350 ºC, were primarily amorphous in nature. FTIR showed a decrease in intensity of C-C and C=C bonds and an increase in Si-C bond with increasing annealing temperature, indicating that free carbon phase dissolved back to SiCN matrix during annealing process. Solid state NMR of ^{29} Si and EPR were used to study the atomic and electronic structure of SiCN matrix, and Raman Spectroscopy was used to study the property of free carbon phase.

3.1 Experiment Procedure

3.1.1 Fabrication of SiCN Ceramics.

3.1.1.1 Starting Materials:

1) The precursor used in this work is a commercially available poly (urea-methyl-vinyl) silazane (PUMVS), (CerasetTM, Kion Corp). As-received Ceraset is a pale yellow

liquid and the molecule formula is showed in figure 19.

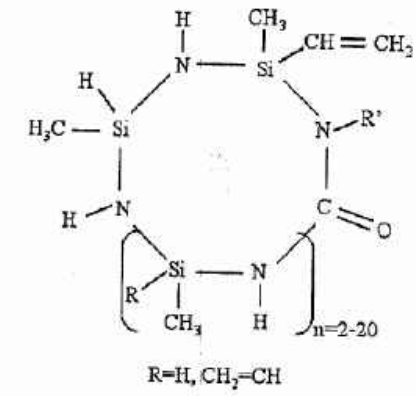

Figure 19: The chemical structure of poly (urea-methyl-vinyl) silazane (PUMVS)

2) Photo initiator powder used in this work is Phosphine oxide, Phenylbis (2,4,6 –trimethyl benzoyl-) (commercially available as Irgacure-819 from Ciba specialty chemicals Corp, USA). Irgacure 819 is a yellow powder and the molecule formula is showed in figure 20.

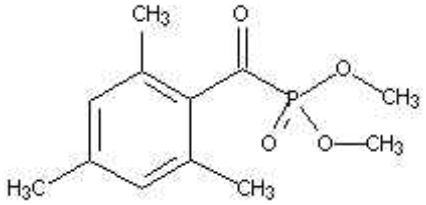

Figure 20: The chemical structure of Irgacure-819

3) Methacrylic acid (2-methyl-2-propenoic acid, $C_4H_6O_2$) is also used in our study to add double bonds into the precursor. Methacrylic acid is a transparent liquid and the molecule formula is showed in figure 21.

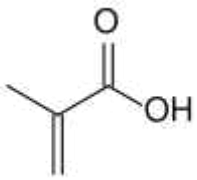

Figure 21: the chemical structure of Methacrylic Acid

3.1.1.2 Fabrication Method

The fabrication method used in our study consists of four steps: (1) addition of a photo initiator/methacrylic acid to the precursor, (2) cross linking the precursor into solid polymeric samples by exposing to UV light, (3) pyrolysis to convert the polymeric samples into ceramic at 1000°C, and (4) annealing the ceramic samples above 1000 ºC. The details of the process are:

1) Dissolve the photo initiator powder Phosphine oxide, Phenylbis(2,4,6 –trimethyl benzoyl-) (commercially available as Irgacure-819 from Ciba specialty chemicals Corp, USA) / Methacrylic Acid (2-methyl-2-propenoic acid, $C_4H_6O_2$) into poly (urea-methyl-vinyl) silazane (PUMVS) (commercially available CerasetTM from Kion Corp, USA) by magnetically stirring the mixed liquid at 105 ºC for 20min.
2) Put the mixed liquid precursor onto the surface of one Teflon-coated glass and then covered it by another Teflon-coated glass. Vertical spacers were sandwiched between these two glasses by which, the thickness of sample can be controlled. The liquid precursor was then exposed under Ultraviolet light (Dymax light curing system,

Bluewave™ 200) for 180 minutes at room temperature and solid polymeric samples were achieved. Following this, the solid polymer samples were removed from the Teflon-coated glasses using a surgical razor blade and cut into rectangular shapes with known dimensions. Finally, the samples were heat treated in an oven for two days at 100 ºC. This process is shown in figure 22.

3) 3and 4: these steps were carried out in a tube furnace in a nitrogen atmosphere. The cross linked rectangular polymer samples were placed between graphite substrates and pyrolyzed and annealed in the tube furnace.

The precursors, cross-linking, pyrolysis and annealing conditions used in this work differ from those used in the previous studies. The precursors used in previous work were powder derived, whereas the precursor that was used here is liquid. For cross-linking process, previous work mostly used thermal initiator such as Dicumyl peroxide and cross linking polymer at 200 ~ 400 ºC whereas, in this study, photo initiator Irgacure-819 was added to precursor as the UV catalyst for solidification. Pyrolysis and annealing conditions in this study are also different from previously studied PDC processes, as shown in figure 23.

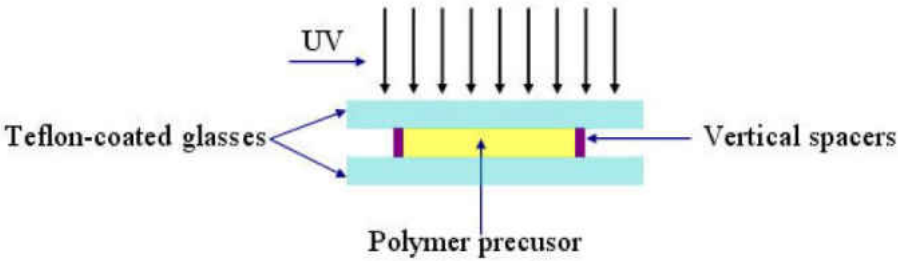

Figure 22: UV curing process of SiCN green body samples

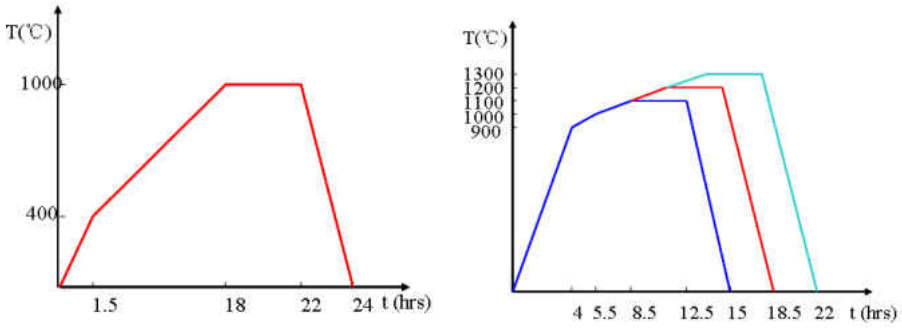

Figure 23: Pyrolysis and annealing conditions for fully dense SiCN sample

3.1.2 Characterization of the Fabricated SiCN Samples

3.1.2.1 XRD Spectra Measurement

X-Ray diffraction is a technique that measures the intensity of x-rays, diffracted by a sample material, to gain information from that material. XRD can determine the crystal structure and lattice parameters of crystalline materials. To study the structural change of SiCN materials during annealing process, Rigaku D/MAX X-ray Diffractometer was used in our research.

3.1.2.2 FTIR Spectra Measurement

FTIR is a powerful tool for identifying different types of chemical bonds in a molecule by producing an infrared absorption spectrum that is like a molecular "fingerprint".

In this part, it was used to analyze the chande in chemical bonds of SiCN ceramics due to annealing in a temperature range of 1000 to 1300 ºC

The fabricated SiCN materials was dried in oven at 60 ºC for 5 hours and then crushed to powder in petal and mortar. The reference chemical of KBr was also dried in oven at 200 ºC for 5 hours and then mixed with dried 0.5~1wt% SiCN. The mixed powder was dried in oven again at 100 ºC for 1 hour and subsequently pressed into disk of 0.5 mm in thickness. The instrument used in our work was FTIR-8400s and the spectrum range was 400~3200 cm^{-1}

3.1.2.3 NMR Spectra Measurement

NMR is a very useful method in investigating the chemical structural changes at the molecular level by showing the appropriate atomic coordination changes during the transformation of polymer-amorphous ceramics. In our work, the solid state NMR spectroscopy of ^{29}Si was used to get information of chemical structural rearrangement of the amorphous SiCN materials during pyrolysis process for a temperature range of 1100~1350 ºC.

The fabricated SiCN material was crushed into powder of ~1 μm by ball milling. The NMR measurement was finished in the National High Magnetic Field Laboratory (NHMFL) in Tallahassee, FL according to following procedure:

High resolution ^{29}Si solid state magic angle spinning (MAS) NMR experiments were carried out using a Chemagnetics 300 MHz Infinity spectrometer at Larmor frequencies of 78.2 and 59.6 MHz for ^{29}Si. A standard CP/MAS probe with a 7.5-mm pencil rotor system was used. A sample spin rate of 5 kHz and 10 kHz were used for ^{29}Si. All ^{29}Si spectra were acquired using a standard single pulse sequence with a tip angle of about 45 degrees and a recycle delay time of 10s (^{29}Si) with accumulation numbers varied between several hundred to 30,000 scans. The ^{29}Si chemical shifts are referenced to tetrakis(trimethylsilyl)silane (TTMS).

3.1.2.4 EPR Spectra Measurement

The status of dangling bonds, including their contents and distribution in SiCN ceramics, plays an important role in deciding the electronic properties of these materials. EPR can be used in studying these status changes of dangling bonds and their relationship with electronic properties of SiCN ceramics during pyrolysis process.

The fabricated SiCN material was crushed to powder of ~1 μm by ball milling. The X-band (9.5 GHz) EPR spectra of the various SiCN ceramics at temperatures ranging from 4K to 300 K were recorded on a Bruker ESP 300E (Bruker, Germany) spectrometer equipped with a Bruker ER 035 M NMR gaussmeter and a Hewlett-Packard HP 5350B microwave frequency counter at the National High Magnetic Field Laboratory (NHMFL) in Tallahassee.

High-frequency EPR spectra (406 GHz) at temperatures ranging from 5K to 300 K were recorded on a home-built spectrometer at the National High Magnetic Field Laboratory (NHMFL) in Tallahassee, FL. The instrument was a transmission-type device in which microwaves are propagated in cylindrical light pipes. The microwaves were generated by a phase locked Virginia Diodes source, generating a frequency of 406.4000(4) GHz ($g \approx 2.00$ around 14.52 T). A superconducting magnet (Oxford Instruments) capable of reaching a field of 17 T was employed.

3.1.2.5 Raman Spectra Measurement

Disordered carbon phase plays a very important role in the amorphous SiCN materials. The detail information like carbon domain size, graphitic ordering, free carbon composition, residual stress in graphite domain, etc. can yield better understanding of the microstructure and the electronic properties of these materials[22, 23, 24, 25, 26, 27,28, 29, 30, 36, 60, 61, 62, 63, 64]. The disordered carbon phase can be studied very well by Raman spectroscopy because this method is very sensitive with respect to the modification of disordered carbon and can give lots of information by recording the intensity, position and width of Raman peaks of disordered carbon. In this study, Raman spectroscopy was used to investigate the details of free carbon phase status as mentioned above in the amorphous SiCN materials and their relationship with electronic properties of these materials.

3.1.2.5.1 Standard curve testing for free carbon composition measurement

In this study, silicon powder (NP-Si-P50, MTI Corporation, Richmond, CA) was used as the external reference since it has strong and sharp Raman signal. In order to obtain the calibration curves, the silicon powder was mixed with pure carbon (graphite) powder (633100, Sigma-Aldrich Corp., St. Louis, MO) at different volume ratios using high energy ball-milling (8000M-115, Spex Certiprep Group, Metuchen, NJ) for 40 min. The obtained powder mixtures were then pressed into disks of 12.5 mm in diameter and 3 mm in thickness. The Raman spectra were obtained using a Renishaw inVia Raman microscopy (Renishaw Inc., UK), employing the 532 nm line of silicon-solid laser and a sensitive Peltier-cooled couple charged device (CCD) detector. The laser beam was focused on the sample through an x 20 objective lens. The laser spot size on the sample was about ~ 10 μm in diameter and the laser power on the sample was kept below 2.5 mW. In order to minimize the measuring error associated with possible non-uniform mixture, at least 20 Raman spectra were obtained for each disk from randomly picked sites.

3.1.2.5.2 Raman measurement of SiCN ceramics

The amorphous SiCN materials was prepared by 4% 819 + 100% Ceraset and 4% 819 + 6% MA + 100% Ceraset that was pyrolyzed at different temperatures according to procedure described in chapter 3.1. The pyrolyzed ceramics was crushed into powder of ~ 1

μm in diameter using high-energy ball-milling for 40 min. After that, the ceramic powder was heat-treated at 800C for two hours to remove the deposited carbon during pyrolysis process. The obtained ceramic powder was mixed with the silicon powder at different volume ratios using the high-energy ball-milling for 40 min. The mixtures were pressed into disks. Raman spectra were obtained from these disks.

3.2 Results and Discussion

3.2.1 Morphology

The pyrolyzed and annealed amorphous SiCN fully dense samples are black ceramic materials as shown in figure 24. The thickness of the sample was about 400 micron and the maximum length was about 1.5 inch. The SEM cross section and surface picture of the sample are also shown in figure 25.

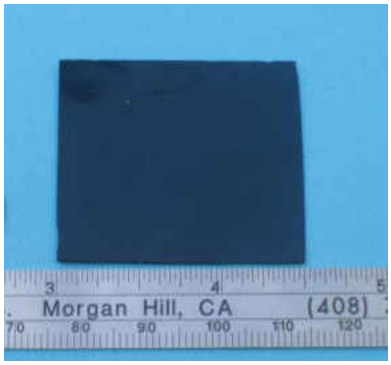

Figure 24: Pyrolyzed and annealed fully dense SiCN sample

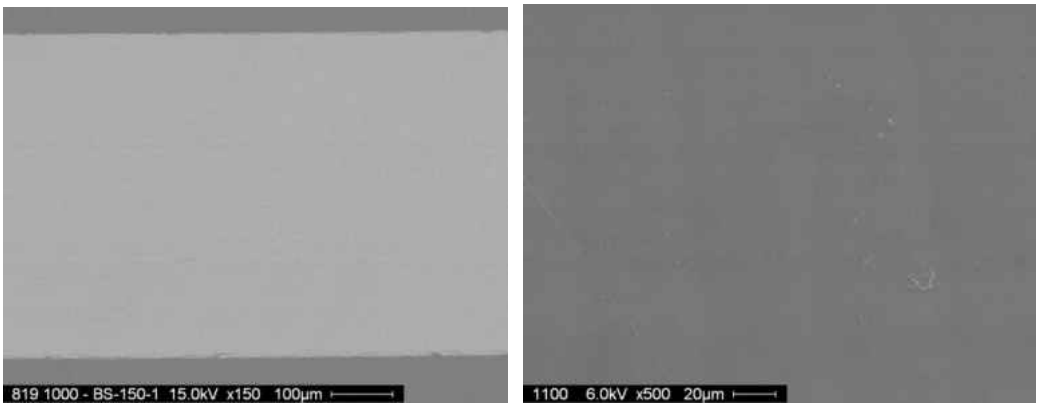

a) *b)*

Figure 25: SEM picture of SiCN sample pyrolyzed at 1100℃: a) cross-section picture (back scattering), b) surface picture.

When heat-treated at 1000~1350 ºC for 4 hours, the annealed samples are uniform and their surfaces are lustrous and smooth black.

3.2.2 XRD Spectra of SiCN Ceramics

In this work, the SiCN fully dense samples heat-treated at different temperature were studied using X-ray diffraction technique to identify the presence of any phases. The results are shown in figure 26. The X-ray diffraction results show that the SiCN fully dense sample, after annealing for 4 h in nitrogen at 1000 ~ 1350 ºC, was primarily amorphous in nature.

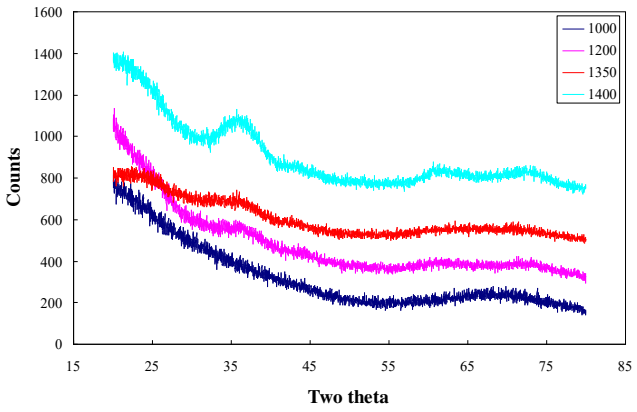

Figure 26: XRD spectrums of SiCN samples pyrolyzed at 1000～1400 ºC.

3.2.3 Raman Spectroscopy Measurement

3.2.3.1 Raman Spectrum Characterization

Figure 27 shows the Raman spectra recorded from the samples of SiCN (4%819 +100%Ceraset, and 4%819+6%MA+100%Ceraset) pyrolyzed at different temperatures, after the subtraction of the linear background.

The Raman spectra of these two sets of SiCN materials have similar features. Two Raman bands were observed at around wave numbers of 1350 and 1600 cm^{-1} for all spectra, which are allocated to the D and G band, respectively. These bands are the two most prominent features of disordered graphitic-like sp2-carbon. In addition, the presence of these two peaks in the spectrum indicates that at least a significant fraction of carbon atoms are bonded as ring-like configurations [65].

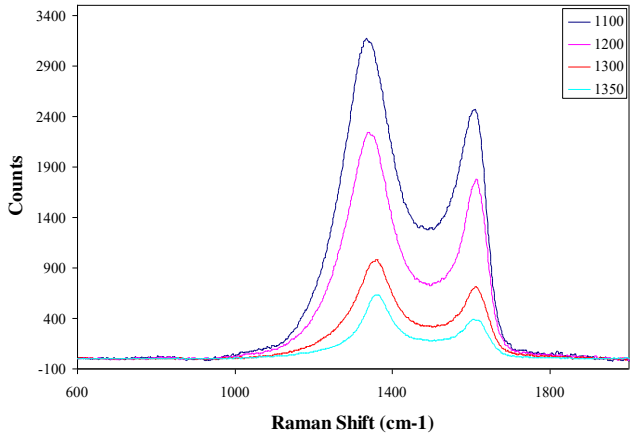

(a)

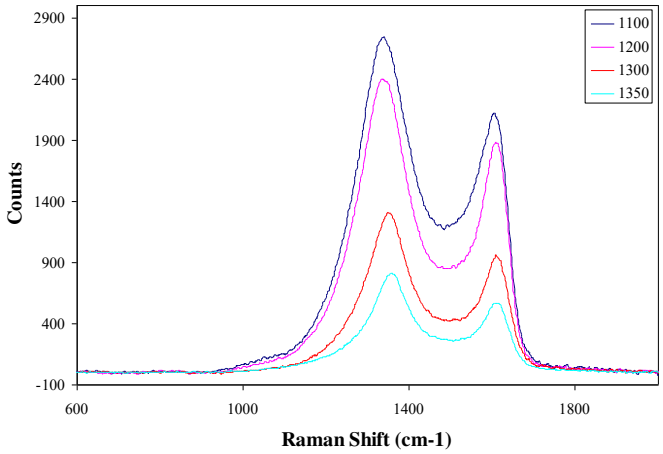

(b)

Figure 27: Raman spectra of SiCN samples pyrolyzed at different temperatures, a) 4%819+100% Ceraset, and b) 4%819+6%MA+100% Ceraset

The G band has E2g symmetry and is generated by in-plane bond stretching of sp2-hybridized carbon pairs [31,52]. This band is active at all sp2 sites and not necessarily limited to those arranged in six-fold symmetry. The D band has A1g symmetry and corresponds to the breathing mode of aromatic rings [31,52]. This band is forbidden in perfect

graphite and becomes active only in the presence of local disorder. The overall relative intensities of the spectra progressively decreased with increasing pyrolysis temperature, suggesting that composition of free carbon decreases with annealing temperature [66]. The intensity of D band was found to be apparently higher than that of G band indicating carbon segregation as glassy carbon clusters [51].

The Raman spectra were fitted using two Gaussian curves in order to extract information including peak position, peak width (full width at half maximum, FWHM), and relative intensity of the D- and G-band. The data are plotted in Figure 28, 29 and 30, respectively.

With increasing pyrolysis temperature, the D peak showed a small but continuous upward shift in position and a steady decrease of its peak width (FWHMD). In addition, a decrease of its relative intensity *I* (D) compared with that of the G peak (*I* (G)) was observed, quantified as the net decrease in the intensity ratio *I*(D)/*I*(G).

In contrast, the G peak position stabilized at all pyrolyzed temperature and the peak width (FWHMG) showed negligible variation for all samples. The population of all C–C bonds and the distribution of the C–C bond angle typically determine the intensity and the width of the G peak, respectively [65].

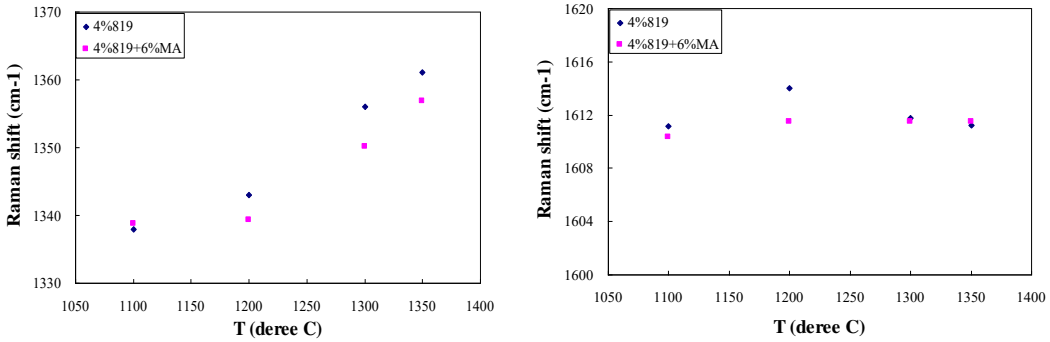

(a) *(b)*

Figure 28: Raman peak positions of SiCN samples (4%819+100% Ceraset, 4%819+6%MA+100% Ceraset) pyrolyzed at different temperatures, a) D band, and b) G band

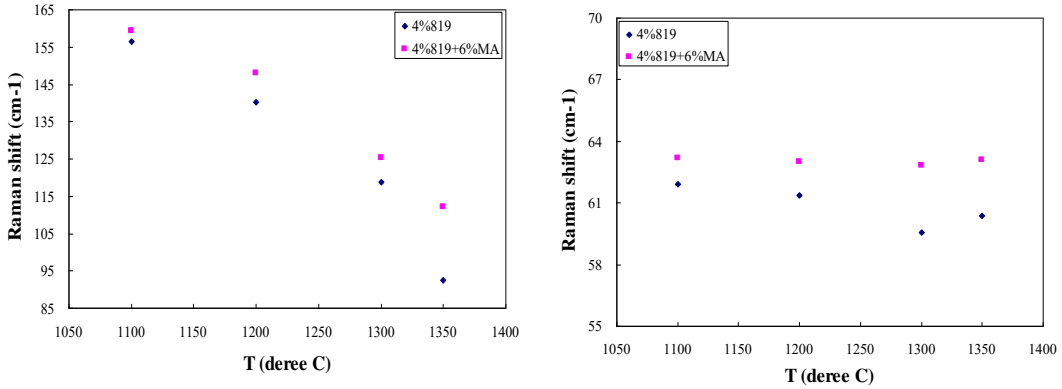

(a) *(b)*

Figure 29: Raman peak widths of SiCN samples (4%819+100% Ceraset, 4%819+6%MA+100% Ceraset) pyrolyzed at different temperatures, a) D band, and b) G band

The D peak shift, peak width and intensity are correlated to the distribution of cluster size and order of carbon atoms. Since the D peak shifts upward and its line widths decrease with increasing pyrolysis temperature, structural rearrangements accompanied by ordering of the free carbon phase into aromatic graphene layers occur for all temperature in the range of

1100 °C < Tp < 1350 °C. The increased ordering will cause a higher mobility of the electrons yielding an increased conductivity.

The intensity ratios of these two bands, I_D/I_G, were found to decrease with an increase in pyrolysis temperature from 1000 to1350 ºC. This fact indicates that the bonding character of carbon changes from sp3 to sp2 and carbon with a basic structural unit of turbostratic structure had been formed.

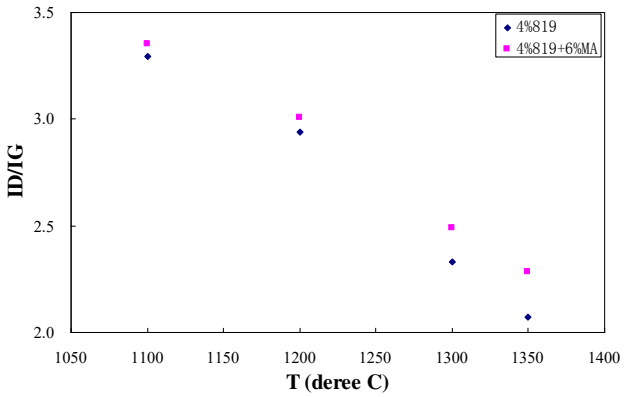

Figure 30: The intensity ratios of D- and G-peaks of Raman spectra of SiCN samples (4%819+100%Ceraset, 4%819+6%MA+100% Ceraset) annealed at different temperature

3.2.3.2 Free Carbon Cluster Size

The intensity ratio I (D)/I (G) can be used to evaluate the lateral size, Ls, of the free carbon domains, as reported by Tuinstra and Koenig [50] for crystalline carbon and more recently by Ferrari and Robertson [52] in the case of amorphous carbon. The results calculated according to equation 2.15 in our work are shown in figure 31, in which, the free carbon domains of these two materials was found to grow with increasing annealing temperature.

$$\frac{I_D}{I_G} = \frac{C}{Ls} \qquad (2.15)$$

Where, the value of constant C depends on the laser wavelength (532 nm) and here corresponds to 49.5 Å [50, 52, 53, 54].

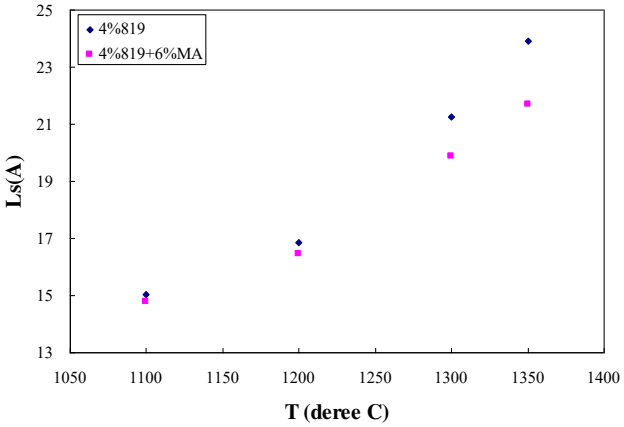

Figure 31: the evaluated lateral, Ls, of free carbon domains of SiCN samples (4%819+100%Ceraset, 4%819+6%MA+100% Ceraset) annealed at different temperature

3.2.3.3 Residual Stress Measurement

Residual stresses are an important factor influencing the strength of these SiCN polymer derived ceramics. The causes of residual stresses are usually differences in the thermo-mechanical properties of the constituents. There are two main reasons here for the introduction of residual stresses: thermal stresses due to differences in expansion coefficients between the carbon cluster and the SiCN matrix, and due to shrinkage during curing or solidification of the matrix [67]. In many cases, the presence of residual stresses can be very detrimental to the electrical insulation performance of the material. The residual stress of free

carbon cluster in ceramics matrix has not been studied extensively[68]. As reported by other researchers [68, 69,70, 71], residual stress within a matrix can be measured by Raman spectroscopy according to the difference of Raman peak shifts upward or downward. In this study, the equation 3.1 was used to calculate the residual stress of free carbon in SiCN materials [68].

$$\sigma = -204 \times \Delta\omega \quad (Mpa) \qquad (3.1)$$

Where, σ is residual stress, Δω is the Raman peak shift. The results of residual stress of free carbon domains in SiCN samples studied in this work are shown in figure 32. The residual stress of free carbon domains within SiCN samples annealed at different temperature show negative values around -1800 Mpa, indicating a state of compressive stress. The stress magnitudes for these samples are almost same, indicating that the shrinkage during annealing process is very small.

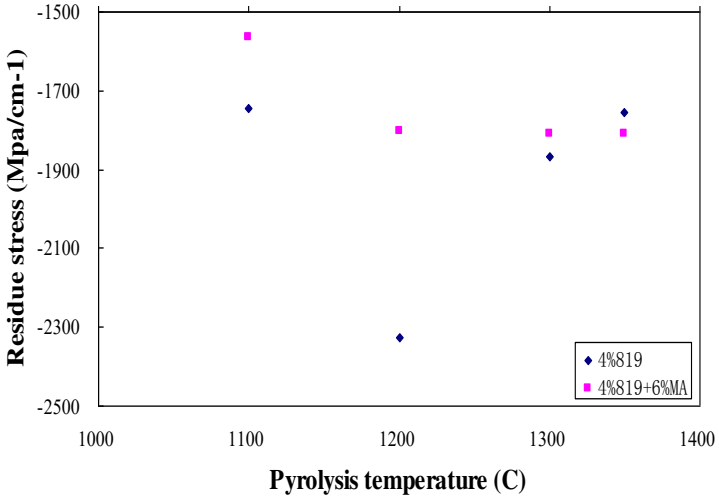

Figure 32: Residual stress of free carbon domains within SiCN samples (4%819+100%Ceraset, 4%819+6%MA+100% Ceraset) heat-treated at temperature 1100~1350 ºC

The influence of starting material MA on the free carbon domains of SiCN materials was also studied. Based on the information mentioned above, the Raman spectra of SiCN prepared by using additives (MA) have lower D peak position, broader linewidth and smaller free carbon domain size. This indicates that MA can retard the ordering of free carbon domains and its growth in size during annealing process, at least with 6% percent.

3.2.3.4 Free Carbon Composition Measurement

While free carbon clusters were widely observed in PDCs, quantitatively measuring their concentration has not been reported. It was proved to be very difficult for such measurements. Transmission electron microscopy (TEM) can only be used to observe these carbon clusters within relatively small areas [65], but is not suitable for large scale quantitative measurements. Due to the amorphous nature of the materials, X-ray diffraction is not suitable for such measurements either. Lack of quantitative information on the free carbon concentrations drastically limits the understanding of the properties of PDCs in detail.

In this study, this Raman spectroscopy-based method for quantitative measurements of free carbon concentrations within polymer-derived ceramics was used for the first time. The method employs silicon as an external reference. First a calibration curve was obtained by measuring the relationship between the concentration ratio of silicon to carbon and Raman band intensity ratio of the two materials. The calibration curve was then used to obtain free

carbon concentrations in PDCs by analyzing the Raman band intensity ratio of silicon to PDCs. The average size of the free carbons was also estimated from the Raman intensity ratio of D- to G-bands.

3.2.3.4.1 Quantitative Raman analysis

Intensity of the Raman band, I of a given species can be expressed as [72]

$$I = k(v)A(v)J(v)CI_o(v)^4 \qquad (3.2)$$

Where $k(v)$ is a constant related to the spectrometer, $A(v)$ the self-absorption of the medium, $J(v)$ a molar scattering parameter, C the concentration of the species responsible for the scattering; I_o the intensity of the incident beam, and v the frequency of the incident radiation. Equation (3.2) cannot be directly used to measure the concentration of the species since the constants associated with the materials are usually difficult to obtain. More importantly, Raman intensity is sensitive to the surface conditions of the sample, thus can vary significantly from sample to sample of the same composition.

However, quantitative Raman analysis can be done by using an external reference. From equation (3.2), Raman signals obtained from the sample containing the external reference can be expressed as

$$\frac{I_r}{I_s} = K\frac{C_r}{C_s} \qquad (3.3)$$

Where I_r and I_s are respective Raman band intensities of the reference and the species to be measured; C_r and C_s are respective concentrations of the reference and the species. The pre-factor K is only related to the properties of the species and the reference, thus should be a constant for a given species-reference system. Note that since both the species and the reference are in the same sample, K is no longer affected by the surface conditions of the sample. It is seen from Equation (3.3) that if K is known, the concentration of the species can be calculated by measuring the relative Raman band intensities from a sample containing a known amount of reference.

For a given species-reference system, K can be determined experimentally. This can be simply done by measuring the relative Raman band intensities from the sample of known species-to-reference ratio. K can also be determined graphically based on Equation (3.3) by measuring relative Raman band intensities from a set of samples with different species-to-reference ratios.

3.2.3.4.2. Results and discussion

Figure 33 shows typical Raman spectra obtained for the pure silicon powder, the pure carbon powder, and the mixture of the silicon and carbon powders. As it is expected, the positions and curve-shapes of Raman signals for both silicon and carbon in the mixture

remains the same as they are in free-stand forms. This is the first sign, that silicon could be a good reference for measuring the concentration of free carbons.

The intensities of Raman signals are measured from figure 33 as the area underneath the signals. For carbon, the intensity is the sum of the area underneath both G-band and D-band. Figure 3.16 demostrated that the intensity ratio of silicon-to-carbon Raman bands as a function of the volume ratio of the two materials (since silicon and carbon are only two components of the mixture, the volume ratio of the two is equal to their volume fraction ratio). It is not a surprise that the signal ratio and the volume fraction ratio exhibit a well-defined linear relationship as predicted by Equation (3.5). Such a well-defined linear relationship is also indicative that our measurements are accurate. The K factor for the silicon-carbon system was calculated to be 0.0164 as calculated from the data presented in figure 34.

To measure the free carbon concentration in amorphous SiCN, silicon powder was mixed with the SiCN powder in known proportions. The typical Raman spectra of the SiCN powder and the mixture are shown in Figure 3.17 (a) and (b), respectively. The spectrum of the SiCN contains only two bands belonging to D and G bands of free carbon. The position and shape of the Raman bands for the SiCN powder in the mixture are the same as they have for pure SiCN.

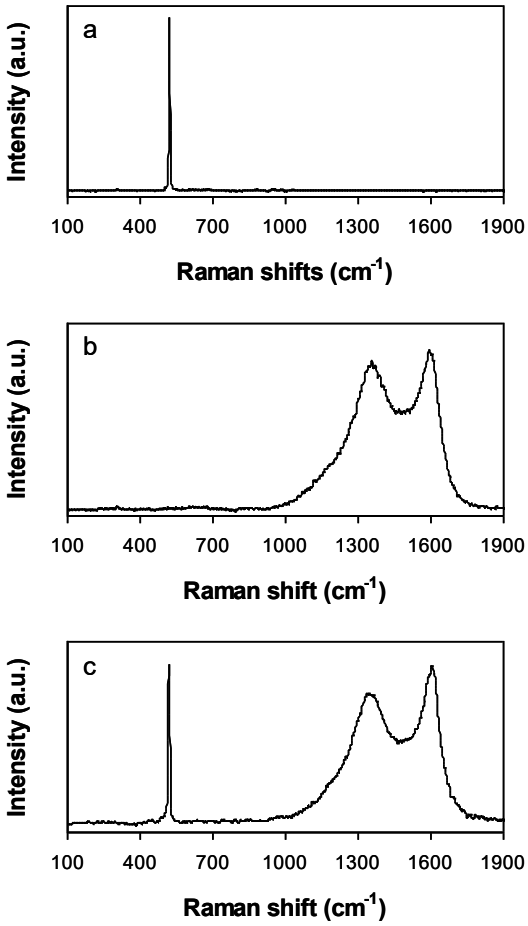

Figure 33: Raman spectra of (a) pure silicon reference, (b) pure graphite powder and (c) the silicon-carbon mixture with the volume ratio of 2:1.

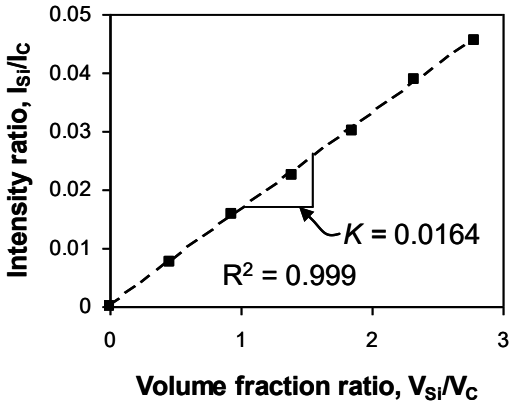

Figure 34: A plot of Raman band intensity ratio of Si-to-C as a function of the volume ratio of Si-to-C.

The SiCN contains a certain amount of the free carbon, whose volume fraction, $C_C^{'}$ is

$$C_C^{'} = \frac{V_C}{V_{SiCN}} \qquad (3.4)$$

where V_C is the volume of the free carbon in the SiCN and V_{SiCN} volume of the SiCN (including that of the free carbon). The respective volume fractions of the free carbon and silicon powder in the silicon-SiCN mixture are

$$C_C = \frac{V_C}{V_{SiCN} + V_{Si}} \qquad (3.5a)$$

$$C_{Si} = \frac{V_{Si}}{V_{SiCN} + V_{Si}} \qquad (3.5b)$$

where V_{Si} is the volume of the reference silicon within the mixture. According to Equation (3.3) and (3.5), we have

$$\frac{I_{Si}}{I_C} = K\frac{C_{Si}}{C_C} = K\frac{V_{Si}}{V_C} \qquad (3.6)$$

Combining Equation (3.4) and (3.6),

$$\frac{I_{Si}}{I_C}\frac{1}{K} = \frac{V_{Si}/V_{SiCN}}{V_C/V_{SiCN}} = \frac{1}{C_C^{'}}\frac{V_{Si}}{V_{SiCN}} \qquad (3.7a)$$

Rearrange Equation (3.7a), we obtain that

$$\frac{V_{Si}}{V_{SiCN}} = C_C^{'}\frac{I_{Si}}{I_C K} \qquad (3.7b)$$

Equation (3.7b) suggests that the volume ratio of silicon-to-SiCN (V_{Si}/V_{SiCN}) should exhibit a linear relationship with the normalized intensity ratio ($\frac{I_{Si}}{I_C K}$); and the slope of the

curve is the free carbon concentration to be measured. Figure 35 (c) plots the V_{Si}/V_{SiCN} as a function of the normalized intensity ratio. A well-defined linear relationship is obtained as predicted by Equation (3.7b). Again, such a well-defined linear relationship suggests that the measurement is highly accurate. The free carbon concentration of these SiCN was measured from the curve and shown in figure 36.

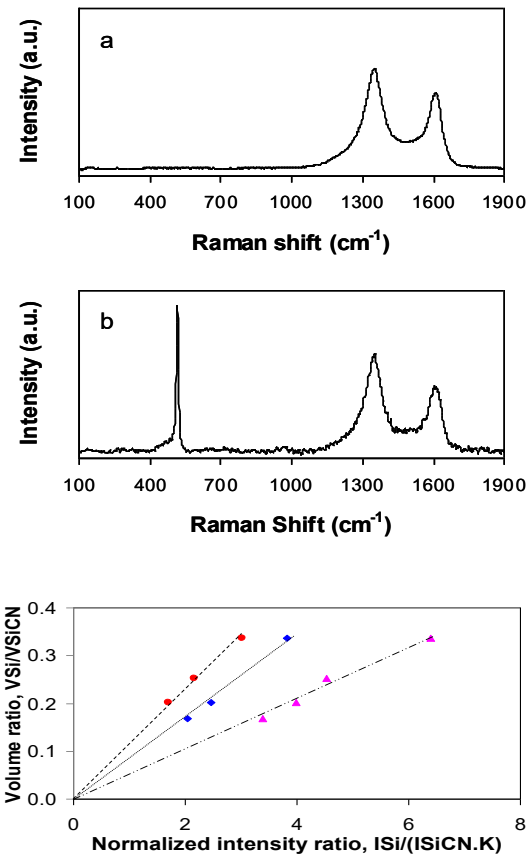

Figure 35: (a & b) Typical Raman spectra obtained from the SiCN powder and the silicon-SiCN mixture with volume ratio of 1:1. (c) A plot of silicon-to-SiCN volume ratio as a function of normalized silicon-to-SiCN Raman intensity ratio.

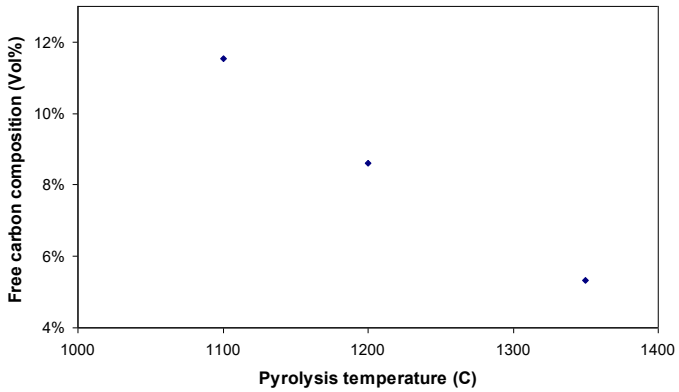

Figure 36: Free carbon volume composition of SiCN ceramics pyrolyzed at different temperature.

Based on the information analyzed from Raman spectra, structural evolution of free carbon phase in SiCN ceramics during annealing temperature range of 1100 ~ 1350 °C can be described as follows: Free carbon phase with ring-like configurations was dispersed in SiCN matrix as glassy form. With increasing pyrolysis temperature, the structure of free carbon was found to be rearranged into aromatic graphene layers with more ordering. Interestingly, the domain size of free carbon increased with increasing annealing temperature, whereas the composition it was found to decrease, which is also proved by FTIR results as discussed in following section.

3.2.4 FTIR Spectra

The FTIR spectra of SiCN ceramics pyrolyzed at different temperature are shown in figure 37. The peaks of 2924 and 2852 cm^{-1} are ascribed to the asymmetric stretching and

symmetric vibration bands of CH_2, respectively [73, 74]. The peaks of 1383 and 1467 cm^{-1} are assigned to CH_3 and CH_2 bent vibration band [73]. The intensities of these C-H related bands decreased with increasing annealing temperature due to loss of Hydrogen. The intensities of peaks of 1402 and 1632 cm^{-1} assigned to C-C and C=C bands also decreased with increasing annealing temperature, indicating that the free carbon composition decreased [75]. This was also proved by Raman spectroscopy measurement. The peaks of 1026 and 1071 cm^{-1} were ascribed to Si-O band, which decreased with increasing temperature and its peak width was found to be broader [73-77]. During pyrolysis process, it is hard to avoid little Oxygen from entering into SiCN ceramics. However, the SiCN pyrolyzed at higher temperature is more compact, thus less Oxygen can enter it. The stretching peaks of Si-N band were found at 850 and 449 cm-1, respectively [73, 78]. The intensity of these two peaks was decreased a little bit during pyrolysis process, revealing the number of Si-N bond decreased. The peaks of 780 and 795 cm-1 were assigned to Si-C band and the intensities of them increase with increasing temperature, indicating Si-C bond in SiCN matrix was increased.

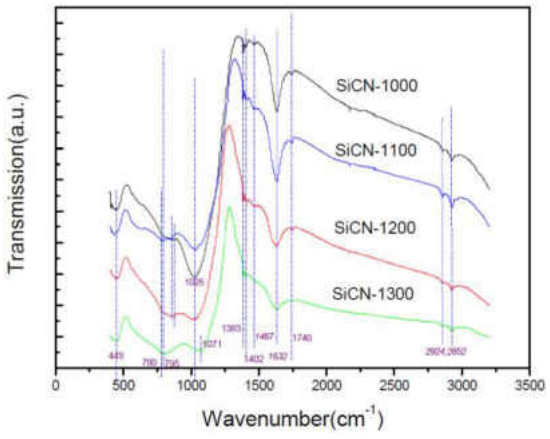

Figure 37: FTIR spectra of SiCN ceramics pyrolyzed at different temperature

Previous study by other researchers have shown that there are two phases in this kind of amorphous SiCN materials, i.e. free carbon and SiCN matrix. During the pyrolysis process at temperature above 1000ºC, the composition of free carbon phase increases qualitatively with increasing annealing temperature due to loss of Hydrogen. However, based on the FTIR results discussed above, there might be least two main mechanisms in the process. Firstly, free carbon phase was produced by loss of Hydrogen from C-H bond and secondly, these free carbons dissolved back into Si-C-N matrix by reacted with some chemistry units within Si-C-N matrix, resulting in increase of Si-C bond.

3.2.5 NMR Spectra Measurement

Figure 38 shows ^{29}Si solid-state NMR spectra of the SiCN ceramics heat-treated at different temperatures from 1100 to 1350 °C. The peak at 8 ppm can be assigned to SiC_3N units [79, 80], whereas SiC_2N_2 is responsible for the peak at -10 ppm [80, 81]. The peak around -25 ppm can be assigned to $SiCN_3$. Intensity of SiC_3N and SiC_2N_2 signals increases with increasing of pyrlysis temperature whereas intensity of $SiCN_3$ decreases. This might be ascribed to following chemistry reaction during annealing process:

$$SiCN_3 + C \rightarrow SiC_2N_2 \qquad (3.8)$$

$$SiCN_3 + 2C \rightarrow SiC_3N \qquad (3.9)$$

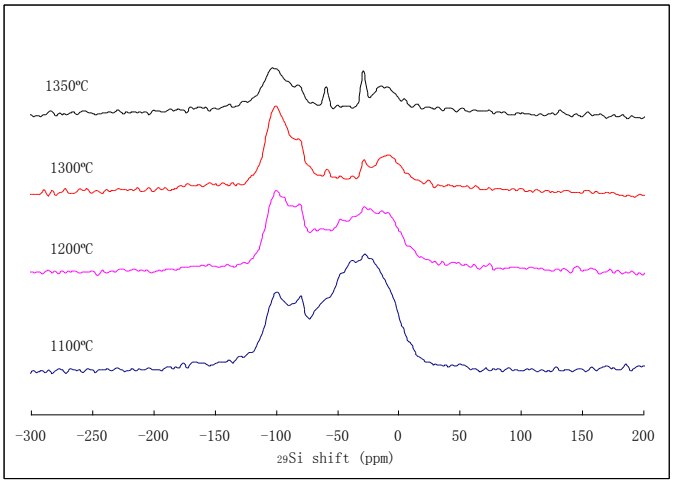

Figure 38: Si solid-state NMR spectra of SiCN samples pyrolyzed at different temperature

Combined with results of FTIR and Raman spectra, we believe that the free carbon produced during pyrolysis process due to Hydrogen loss from C-H band, dissolved back into Si-C-N matrix with increasing annealing temperature, resulting in a decrease in free carbon content.

The peaks of -58, -82, -100 cm^{-1} are assigned to SiN_2O_2, $SiCO_3$ and SiO_4, respectively [80]. Intensity of $SiCO_3$ and SiO_4 signals increases with increasing pyrolysis temperature whereas intensity of SiN_2O_2 decreases with temperature. During pyrolysis process, it is very hard to prevent small amount of air from entering the tube furnace. The air reacted with SiCN matrix by substituting the N and C to form more Si-O band on the ceramics surface, resulting in increase of Intensity of $SiCO_3$ and SiO_4 signals.

By curve fitting for the obtained NMR spectra, the number of these chemistry units and related chemistry bond within SiCN matrix can be calculated semi-quantitatively. The results are shown in table 3 and 4, respectively.

Table 3: Percentage of different chemistry units within SiCN ceramics, SiO_4 unit was removed due to oxidation of samples surface.

	SiO_3C	SiN_2O_2	$SiCN_3$	SiC_2N_2/SiC_3N
SiCN-1100	6.55%	26.22%	59.39%	7.84%
SiCN-1200	22.25%	38.19%	14.42%	25.14%
SiCN-1300	37.71%	2.27%	5.03%	54.99%
SiCN-1350	15.71%	7.22%	15.21%	61.87

Table 4: Percentage of different chemistry bonds related to chemistry units shown in table 2 within SiCN ceramics.

	Si-C	Si-N	Si-O
SiCN-1100	18.77%	63.21%	18.02%
SiCN-1200	16.18%	48.04%	35.78%
SiCN-1300	28.75%	41.83%	29.42%
SiCN-1350	34.74%	49.86%	15.40%

In table 4, Si-C bond increases with temperature whereas Si-O bond decreases. Meanwhile, the Si-N bond also decreases a little bit. These results have similar trend as that of FTIR.

3.2.6 EPR Spectra Measurement

3.2.6.1 X-band (9.5 GHz) EPR Spectra of Various SiCN Samples

3.2.6.1.1 Room temperature measurement

The room-temperature *X*-band (9.5 GHz) EPR spectra of various SiCN samples and

their linewidth as a function of pyrolysis temperature of the sample are shown in figure 39. At *X* band, only one single isotropic symmetric line was recorded for all samples independent of their pyrolysis temperatures at room temperature with the *g* values equal to 2.0047±0.0001. This reveals that the observed EPR signal in these samples is neither due to carbon-related defects with g value of 2.0027~2.0032[56,82] nor due to silicon-related dangling bonds which is characterized by the *g* value of 2.005[14], whereas due to an "average effect" of exchange interaction related to the high spin concentration comes from different dangling bond sources [58].

At room temperature, the peak-to-peak linewidth of these spectra decreases with increasing pyrolysis temperature. This is due to the increase in the number of dangling bonds (paramagnetic) produced in the SiCN materials with increasing pyrolysis temperature, enhancing exchange narrowing of the EPR line.

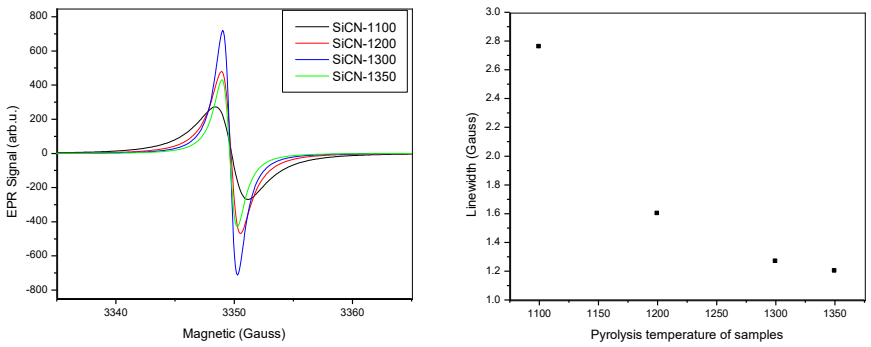

a) *b)*

Figure 39: The EPR spectra measured at room temperature for various SiCN ceramics pyrolyzed at different temperature and the linewidth of these spectra

3.2.6.1.2 Low temperature measurement

The EPR spectra measured at low temperature for SiCN ceramic pyrolyzed at 1300ºC and temperature dependence of linewidth of SiCN ceramics pyrolyzed at 1100, 1200, and 1300ºC are shown in Figure 40.

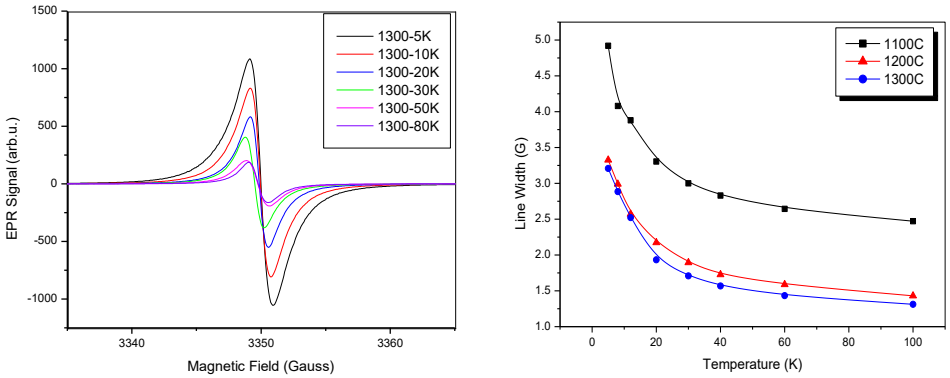

a) b)

Figure 40: The EPR spectra measured at low temperature for various SiCN ceramics pyrolyzed at different temperature and the linewidth of these spectra

These spectra are also symmetric and there are no hyperfine peaks. A decrease in peak-to-peak linewidth of EPR spectra with increasing temperature was observed.

Due to the apparently isotropic character of the spectrum and the absence of any resolved hyperfine interactions or *g*-tensor anisotropy at X band spectra, the information on the nature and microscopic structure of the paramagnetic centers is very limited. One reason for the observation of an isotropic symmetric line is the importance of the "average effect" of exchange interaction related to the high spin concentration [58]. To overcome this ''averaging

effect'' and to reveal the detail information of electronic structures of the paramagnetic centers in SiCN ceramics, we have extended the EPR measurements from the *X* band (9.5 GHz) range to the high frequency of 406 GHz.

3.2.6.2 EPR Spectra of SiCN Samples Tested at High Frequency

3.2.6.2.1 Room temperature high frequency EPR spectra of SiCN samples

Figure 41 shows the High frequency EPR spectra of various SiCN samples tested at room temperature. At a higher microwave frequency of 406 GHz , the room-temperature EPR spectra of SiCN samples also consist of a symmetric line with g value of 2.0032±0.0001, which is due to the dangling bonds present in the defects within the bulk SiCN ceramic network [56]. This g-factor is far from *g*=2.018, 2.02, and 2.012, those for the planar graphite phase [58], turbostratic carbon [83] and multiwall nanotube phase [58], respectively, which are ordered networks. It implies that the SiCN ceramics synthesized here do not contain ordered carbon networks. In addition, this g-factor is totally different from that of the single spectrum at X band (2.005), indicating that the higher frequency of 406 GHz can overcome the "average effect" produced by the high spin concentration at X band. Compare to X band, an additional weaker line with a slightly higher *g* value of 2.0050±0.0001 is present in high frequency of 406 GHz spectra, shown in figure 5. The *g* value of 2.0050±0.0001 for the less

intense line is due to silicon-related dangling bonds [56].

Free carbon can be formed during the pyrolysis process of PDCs, which was reported by many articles and proved by NMR and Raman results in our study. However, its typical EPR *g* value of 2.0027 has not been observed in EPR spectra of all SiCN samples tested with both low and high microwave frequency in our study. This phenomenon is different from the results reported earlier.

EPR signal intensity is proportional to spin concentration (defects density), which decides the conduction property of amorphous semiconductor. EPR signal intensities of various SiCN samples are calculated from the room temperature high frequency spectra on the assumption that the number of spins is proportional to product of (peak-to-peak width)^2 x (peak-to-peak height). In the absence of peak fitting and spin concentration of reference materials, these values of signal intensity are only an approximate and are intended to illustrate the relatively differences in ESR activity of these SiCN samples pyrolyzed at different temperature. The signal intensity of dangling bond from Si and C within SiCN matrix is shown in figure 42 and figure 43, respectively.

The both signal intensities of Si and C within matrix increased with increasing pyrolysis temperature, indicating that the defects in matrix increase. And the intensity of Si-related dangling bond is very smaller as that of C-related dangling bond, indicating that the conduction property of SiCN ceramics is mainly decided by carbon within in matrix.

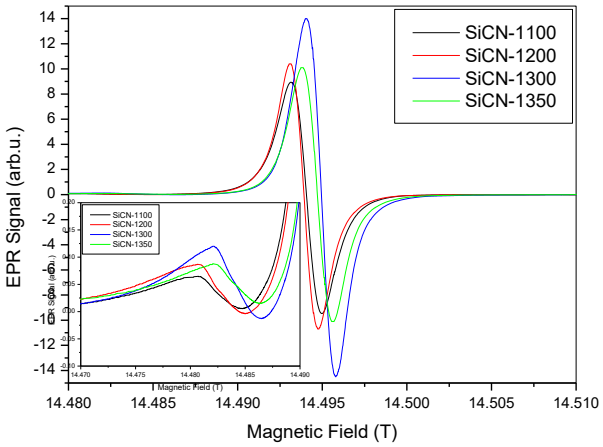

Figure 41: The high frequency (406.6GHz) EPR spectra measured at room temperature for various SiCN ceramics pyrolyzed at different temperature

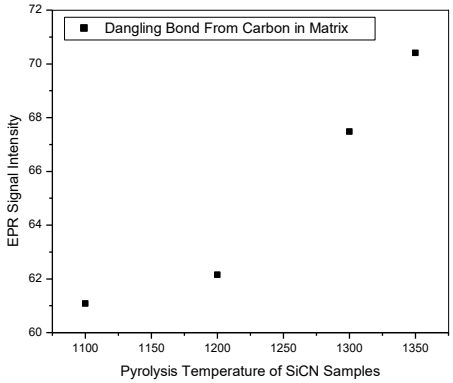

Figure 42: Dangling bonds from carbon - related bond within SiCN matrix of samples pyrolyzed at different temperature

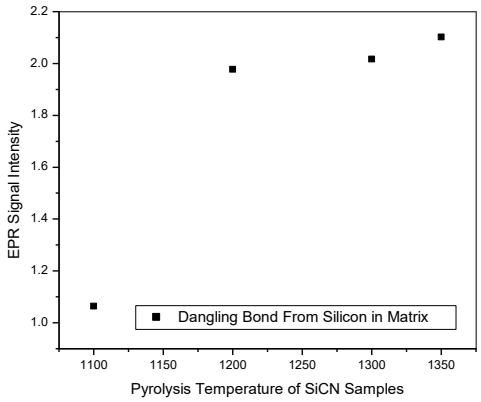

Figure 43: Dangling bonds from Si - related bond within SiCN matrix of samples pyrolyzed at different temperature

3.2.6.2.2 Low temperature high frequency EPR spectra of SiCN samples

In order to gain a complete information about dangling bonds present in the surface defects of the free carbon phase, the EPR testing for SiCN samples with frequency of 406 GHz was taken at low temperature range 5K ~ 80K. The EPR spectra and linewidth are shown in figure 44 and 45, respectively. The *g* value for the less intense line is 2.0050±0.0001, and for the intense line is 2.0032±0.0001, respectively, which is similar as that of samples tested at room temperature.

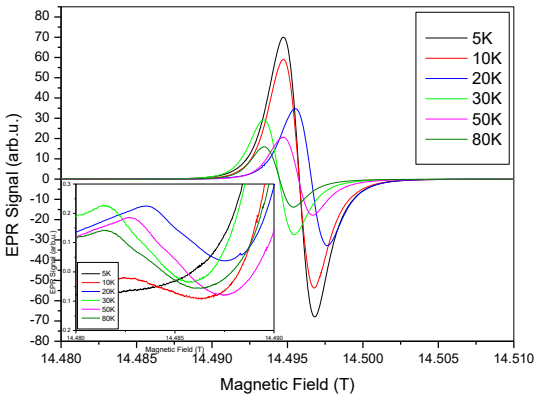

Figure 44: The high frequency (406.6GHz) EPR spectra measured at low temperature for various SiCN ceramics pyrolyzed at different temperature

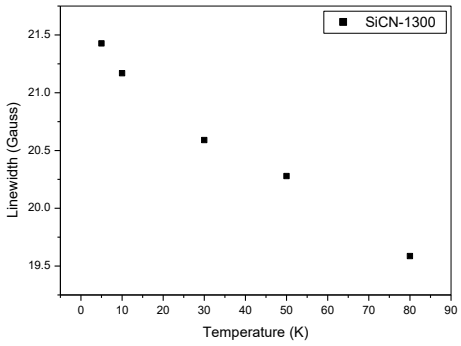

Figure 45: The linewidth of high frequency (406.4GHz) EPR spectra measured at low temperature for various SiCN ceramics pyrolyzed at different temperature

3.3. Summary

Amorphous SiCN ceramics were fabricated at a temperature range of 1000 ~ 1350ºC, which has uniform structure. The material has two phases including free carbon domain and SiCN matrix.

Free carbon phase with ring-like configurations is dispersed in SiCN ceramics as glassy form. With increasing pyrolysis temperature, the structure of free carbon was found to rearrange into aromatic graphene layers and became more ordering. The domain size of free carbon increased with increasing of annealing temperature, whereas its composition decreased by dissolving back into SiCN matrix.

The SiCN matrix has some chemistry units including $SiCO_3$, SiN_2O_2, $SiCN_3$, SiC_2N_2, and SiC_3N. With increasing pyrolysis temperature, the structure and composition of these units were also changed. Number of $SiCO_3$, SiC_2N_2, and SiC_3N units increased while SiN_2O_2, $SiCN_3$ decreased. The corresponded Si-C bond increased with temperature, whereas Si-O bond decreased. Meanwhile, the Si-N bond also decreased to an appreciable level.

In addition, the dangling bond within SiCN matrix related to Si- and C- bond increased with annealing temperature, which would alter the electrical property of these materials.

CHAPTER FOUR: ELECTRONIC PROPERTY OF POLYMER DERIVED SiCN CERAMICS

The aim of this chapter is to study the electrical properties of polymer derived SiCN ceramics pyrolyzed at different temperatures. The conductivity of SiCN was measured by I-V curve at room temperature and T-dependence of conductivity was measured using a digital-multimeter with an accuracy of ± 0.5% in high temperature tube furnace. Hall Effect was measured by Lakeshoe's system. The results show that the d.c. conductivity of SiCN ceramics increased with increasing annealing temperature and the conduction mechanism of amorphous semi-conductor could be used to interpret the conduction phenomena of SiCN ceramics. UV-visible light measurement were carried out using UV-VIS-NIR3101 over a range of 190~800nm to study the absorption property of the materials. .

4.1 Experiment Procedure

4.1.1 D.C.-Conductivities of SiCN Fully Dense Ceramics

Square shaped SiCN samples (10 mm X 10 mm X 0.5 mm) were heat-treated for 2 hours at 800°C in air to remove carbon powder deposited during pyrolysis process. Two ends of samples were polished by 600 grit SiC grinding paper and coated with silver paste. After

that, the samples were dried in air for two days. The D.C-conductivities of fully dense SiCN ceramics were tested. The setup is shown in figure 46. The volt range is -10 V ~ +10 V.

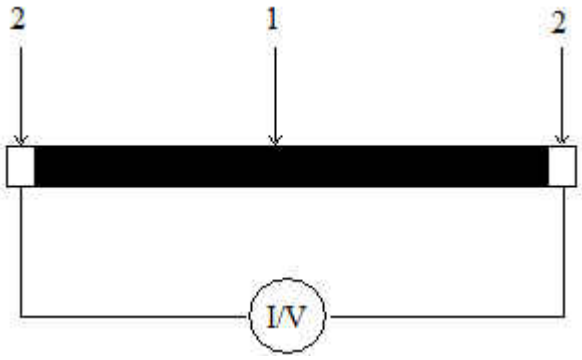

Figure 46: SiCN sample prepared for I-V curve measurement, 1. Sample, 2. Silver paste

4.1.2 Temperature dependence of d.c. conductivity

Two faces of square SiCN samples (10mm × 10mm × 0.5mm) were polished with 600 grit SiC grinding paper and washed in acetone under ultrasonication for 5 minutes. The polished faces were then coated with conductive silver paste and dried under IR light for one hour. The d.c conductivity of the SiCN samples was measured at temperature range 25 ~ 800ºC using a digital-multimeter with an accuracy of ± 0.5%. The samples were subjected to high temperature in a tube furnace under UHP Nitrogen atmosphere. Both the multimeter and a thermal couple were connected to a computer, so that the resistance and temperature were read at the same time. The setup is shown in figure 47.

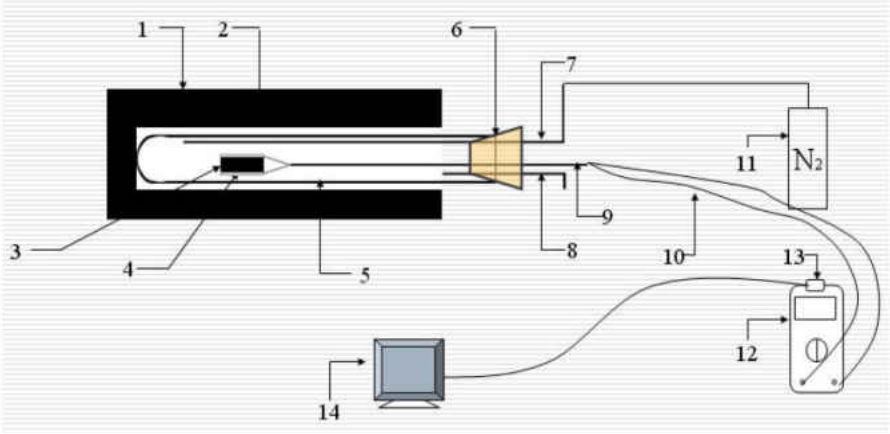

Figure 47: 1. Oven body, 2. Oven Chamber, 3. SiCN Sample, 4. Silver Paste, 5. Al2O3 tube, 6. Rubber Stopper, 7. Flowing N2 Tube (inner), 8. Flowing N2 Tube (outer), 9. Al2O3 Tube with Double holes, 10. Silver wire, 11, N2 tank, 12. Multimeter, 13. RSC IR detector, 14. Computer.

4.1.3 Hall Effect of SiCN ceramics.

One face of square SiCN samples (10mm × 10mm ×0.5mm) were polished with 600 grit SiC grinding paper and washed in acetone under ultrasonication for 5 minutes. Four In particles were put on the four corners of the surface, respectively. Then the samples were heat-treated in vacuum oven (10^{-3}Pa) for 3 minuets at temperature 180 ºC. The resistivity and the Hall Effect of the samples were measured with Vander Pauw Method shown in figure 48 and 49, using Lakeshoe's system.

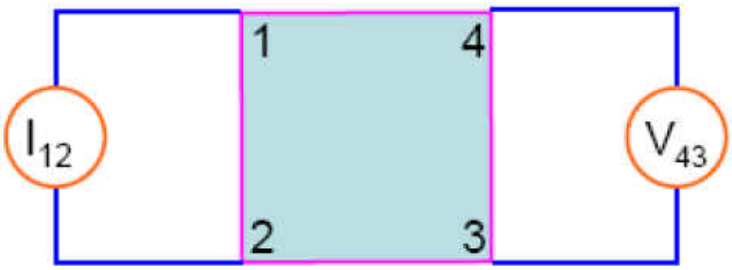

Figure 48: Resistivity of SiCN samples measured by Vander Pauw Method

$$\rho = \frac{\pi}{\ln 2} \times \frac{V_{43}}{I_{12}} \times t = 4.5324 \times \frac{V_{43}}{I_{12}} \times t \qquad (4.1)$$

Where, ρ is resistivity of samples, V_{43} is voltage between point 3 and 4, I_{12} is current from point 1 to 2, t is thickness of samples.

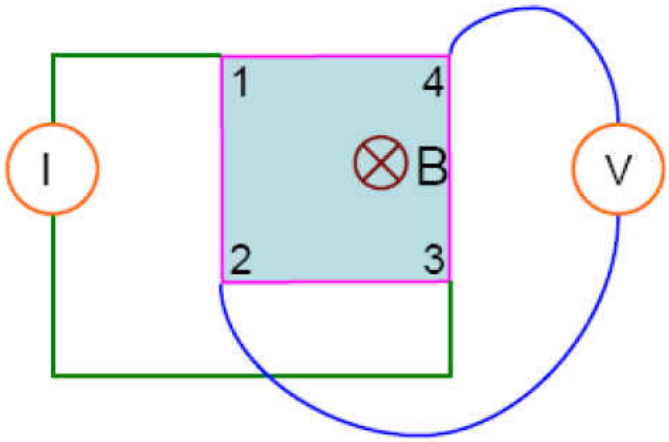

Figure 49: Hall Effect of SiCN samples measured by Vander Pauw Method

$$R_H = \frac{V_{42} \cdot t}{I_{13} \cdot B} \qquad (4.2)$$

Where, R_H is Hall coefficient, V_{42} is voltage between point 2 and 4, I_{13} is current from point 1 to 3, t is thickness of samples, B is intensity of magnet filed.

With results of R_H and ρ, we can calculate parameters like carrier density, Hall mobility, etc.

$$n = \frac{1}{R_H e} \qquad (4.3)$$

$$\mu = |R_H|\sigma = |R_H|\frac{1}{\rho} \qquad (4.4)$$

4.1.4 UV light absorption measurement of SiCN ceramics.

SiCN samples were prepared with procedure described in chapter 2 and were subsequently crushed into powders of ~ 1 μm size, which were mixed with KBr powder and pressed into discs of 10 mm diameter and 0.5 mm thick. The ratio of the SiCN powder to KBr powder was controlled so that the overall absorption coefficient of the discs range between 0.2-0.8 to optimize the results. The optical absorption spectra of the disks were obtained using a UV-3101 double channel spectrometer over a range of 190~800 nm. The absorption spectra of the SiCNs were obtained by extracting the spectrum of the pure KBr powder from those of the mixtures.

4.2 Results and discussion

Previous studies suggested that PDCs were comprised of an amorphous matrix and distributed carbon clusters (also referred as to free carbons) [33, 34, 84]. For SiCN ceramics, the amorphous matrix is a random network, with SiC_xN_{4-x} (x=0, 1, 2, 3, and 4) as building units, as summarized by Raj et al. [85]. There are also a fairly high number of C-dangling bonds with unpaired electrons within the matrix due to the loss of hydrogen [41]. Based on this structural model, several conducting mechanisms could function in PDCs, as described schematically in Figure 50.

When the free-carbon concentration reaches a certain critical level, the electrical

conductivity of the material should follow percolation models, especially when the carbon concentration is lower than the critical level, the electrical conductivity should be determined by the matrix phase, which should follow amorphous semiconducting behavior [86, 87, 88]. For percolation models, the electrical conductivity is mainly controlled by free carbon concentration. In addition, high piezo-resistivity property is clear evidence for tunneling–percolation process [88]. For the matrix-controlled amorphous semiconducting mechanism, the electrical conductivity is affected by both the chemical bonding configuration of the amorphous network (effect on band gap) and the C-dangling bond concentration (effect on defect concentration) [88]. The conduction of SiCN ceramics studied in our research should follow matrix-controlled amorphous semiconducting mechanism because no sign of piezo-resistivity property in these samples was found before. This result will also be proved by other electronic properties of the samples shown in following sections.

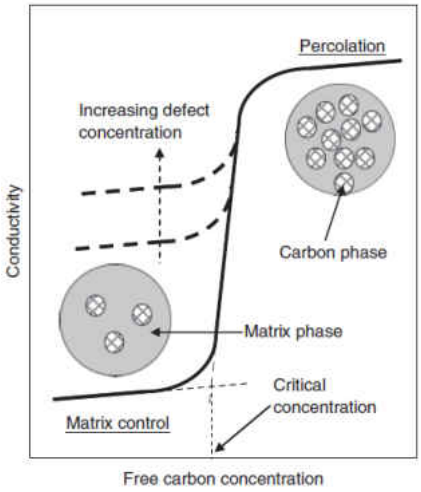

Figure 50: Schematic showing the possible conducting mechanisms in polymer-derived ceramics

4.2.1 Hall Effect Measurement:

The electrical parameters of SiCN samples pyrolyzed at 1100, 1200, 1300ºC obtained by Hall Effect are shown in table 5. The amorphous SiCN samples annealed at these three temperatures are n type semiconductors and the Carrier Density and Carrier Mobility was found to increase with increasing annealing temperature, whereas the Resistivity and Hall Coefficient decreased. The Carrier Mobility of these three samples are very low, indicting that lots of localized states are in the amorphous SiCN materials. The increase of Carrier Mobility with annealing temperature reveals the ordering process of the materials. From the changes of Carrier Density and Carrier Mobility, the conductivity of the materials is mostly due to Carrier Density.

Table 5: Hall Effect results of SiCN samples pyrolyzed at temperature of 1100, 1200, and 1300 ºC

	Field (G)	Resistivity (Ω.cm)	Hall Coefficient	Type	Carrier Density(cm^{-1})	Hall Mobility ($cm^2.V^{-1}.S^{-1}$)
SiCN-1100	9.0001E+3	4.1033E+6	-5.3750E+5	n	1.1613E+13	1.3471E-1
SiCN-1200	9.0001E+3	4.1810E+4	-1.0816E+4	n	5.7714E+14	2.6263E-1
SiCN-1300	9.0001E+3	1.3264E+3	-9.2375E+2	n	6.7575E+15	6.9967E-1

4.2.2 D.C.-Conductivities of SiCN Ceramics

4.2.2.1 D.C.-Conductivities of SiCN Ceramics Prepared by 4, 10%819+100%Ceraset

I–V measurement is one of the most simple and widely used technique to determine

the basic electric characteristics of semiconductor materials. Typical I–V curves of SiCN samples pyrolyzed at different temperature are shown in Figure 51.

I-V curves for these samples have typical semiconductor behavior, i.e. the curves are symmetric non-straight line. The d.c. conductivities of SiCN ceramics prepared by 4, 10% 819 + 100% ceraset were calculated from I-V curves and Ln (σ) versus 1/K is plotted as shown in figure 52:

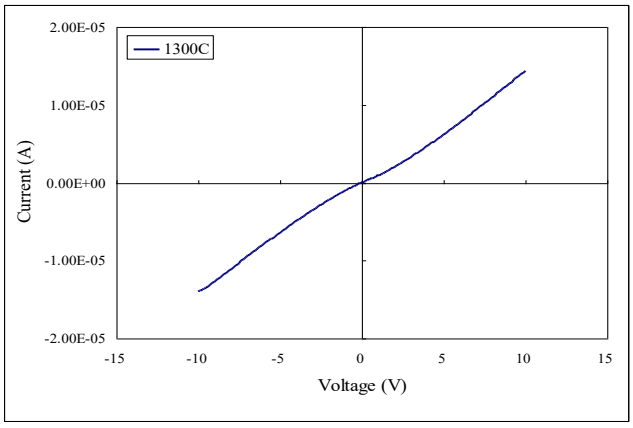

Figure 51: Typical I-V curves of SiCN samples.

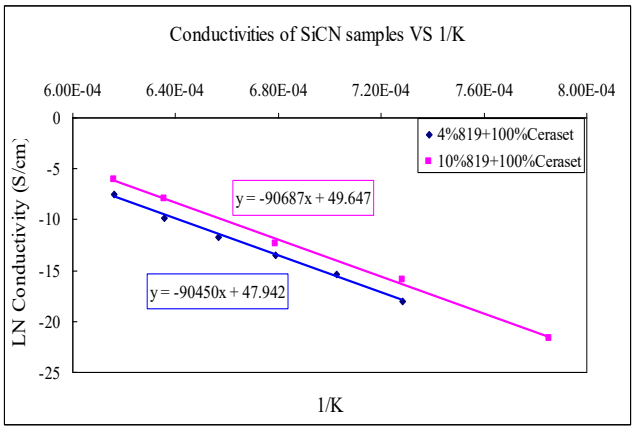

Figure 52: Conductivities of SiCN samples (4, 10%819+100% Cearset) pyrolyzed at different temperature from 1000 to 1350 ºC in N_2 tube furnace

In temperature regime 1000~1350 ºC, conductivities of these materials increased by as much as 7 orders of magnitude with increasing annealing temperature. Interestingly, the Ln (σ) shows a very good linear behavior with 1/K, which has never been reported earlier. Materials conductivity is typically decided by carrier density and its mobility. The carrier mobility of these SiCN materials is very low and carrier density plays a more important role in conduction. Linear behavior of conductivity of these materials indicates that the carrier density also increased with annealing temperature, suggesting there is an equilibrium reaction which can produce charge carriers. Based on the results obtained by structure testing shown in chapter 2, the equilibrium reaction in most probability is that the free carbon dissolved back to Si-C-N matrix and produced carbon related dangling bond.

The slopes for these two sets of samples are almost same, indicating the reaction mechanisms were not influenced by 819 compositions. This linear behavior can be used to calculate the reaction activation energy by the Arrhenius type functions expressed in equation 4.6 and 4.7:

$$\sigma = \sigma_0 \times Exp(\frac{-\mu}{kT}) \qquad (4.6)$$

$$Ln(\sigma) = Ln(\sigma_0) - \frac{\mu}{kT} \qquad (4.7)$$

Where, σ is d.c conductivity of SiCN fully dense samples, μ is reaction activation energy, k is Boltzmann constant, T is pyrolysis and annealing temperature, σ_0 is a coefficient. From these equations, we can get parameters as shown in table 6:

Table 6: parameters of A and μ of SiCN samples pyrolyzed with different precursors

	4%819	10%819
σ_0	6.62E+22	3.64E+21
μ (eV)	7.79	7.81

The conductivity of SiCN samples increased with increasing annealing temperature and shows no significant increase in conductivity but a linear behavior. This indicates that the free carbon concentration is not high enough to form carbon-cluster-based tunneling–percolation networks. In addition, the composition of free carbon in these samples decreased with annealing temperature, which contradicts to the tunneling–percolation mechanism in which both of the conductivity and free carbon concentration of samples should increase in same trend. Consequently, the conductivities of the SiCNs arise from the semiconducting process. The increase of conductivities of the SiCNs with annealing temperature is due to the change of the solid state structure of the amorphous SiCN phase owing to the rearrangement of free carbon. As shown in results of FTIR, Raman spectroscopy, EPR and NMR, the free carbon dissolved back into SiCN matrix with increasing pyrolysis temperature, resulting in a decrease in free carbon content and dangling bond within SiCN matrix increased and thus the electrical conductivity was found to be increased.

4.2.2.2 D.C.-Conductivities of SiCN Ceramics Prepared by wt %MA +4%819+100%Ceraset

The electronic properties of SiCN fully dense samples can be changed by adding some chemicals such as MA into mixed liquid precursors. MA may influence the electronic properties of SiCN samples because they not only provide lots of double bonds, which will provide much more charge carriers, but also can react with ceraset and thus change the structure of the mixed precursors. The d.c.-conductivities of SiCN ceramics prepared by 0, 6, 10, and 20%MA +4%819+100%Ceraset pyrolyzed at different temperatures are shown in figure 53.

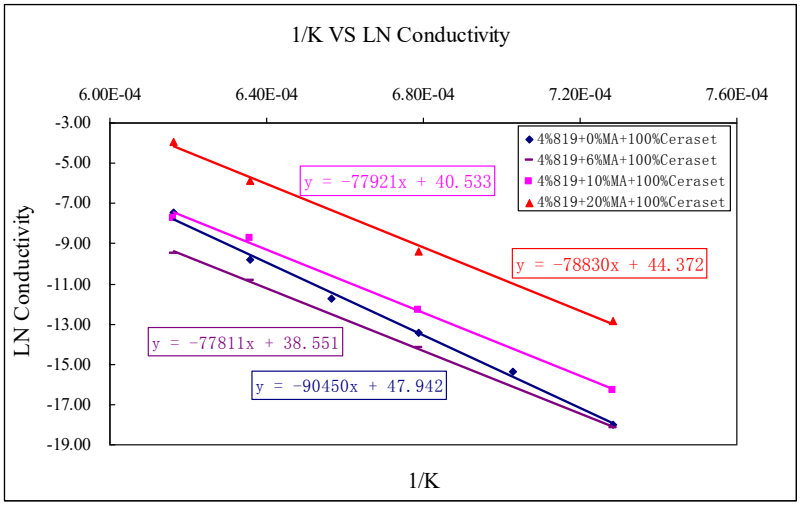

Figure 53: Conductivities of SiCN samples (0, 6, 10, 20%MA+4%819+100% Ceraset) pyrolyzed at different temperature from 1100 to 1350 ºC in N_2 tube furnace

In comparison to samples prepared by precursor without MA, the conductivity of samples prepared by mixed precursor consists of MA decreased (6% MA) followed by an

increase with increasing MA content (10 and 20%MA). This can be interpreted as follows. For a minor addition of MA (6%) into Ceraset, MA reacted and the double bond of Ceraset was dissipated thus the conductivity of pyrolyzed ceramics decreased. With an increased addition of MA, the double bond of MA can make up for the dissipated bonds and thus increase the total number of these bonds, thereby increasing the conductivity. However, the density of dangling bonds in SiCN ceramics is very high, so the addition of MA cannot alter the conductivity to a greater extent. The details of chemical reaction between MA and ceraset need to be investigated thoroughly.

In figure 53, the Ln (σ) also shows a very good linear behavior with 1/K. The slopes for these three sets of samples are almost same but are different from that of samples prepared by mixed precursors without MA, indicating that the reaction mechanisms were influenced by MA. The parameters of σ_0 and μ are shown in table 7

Table 7: Parameters of A and μ of SiCN samples pyrolyzed with different precursors

	0%MA	6%MA	10%MA	20%MA
σ_0	6.62E+20	5.53E+16	4.01E+17	1.60E+19
μ (eV)	7.79	6.70	6.71	6.77

4.2.3 Temperature Dependence of the D.c.-Conductivity

The Temperature dependence of the d.c.-conductivity of SiCN materials are shown in figure 54. It is seen that the conductivity increased drastically with increasing pyrolysis

temperature. The room-temperature conductivity is increased by seven orders of magnitude when pyrolysis temperatures increase from 1000 to 1300°C. More interestingly, the results also show that all samples exhibit semiconducting behavior with positive temperature coefficients of the electrical conductivity. This demonstrates that the conduction is not dominated by a tunneling-percolation mechanism, as that should lead to a negative temperature coefficient of the electrical conductivity [89, 90].

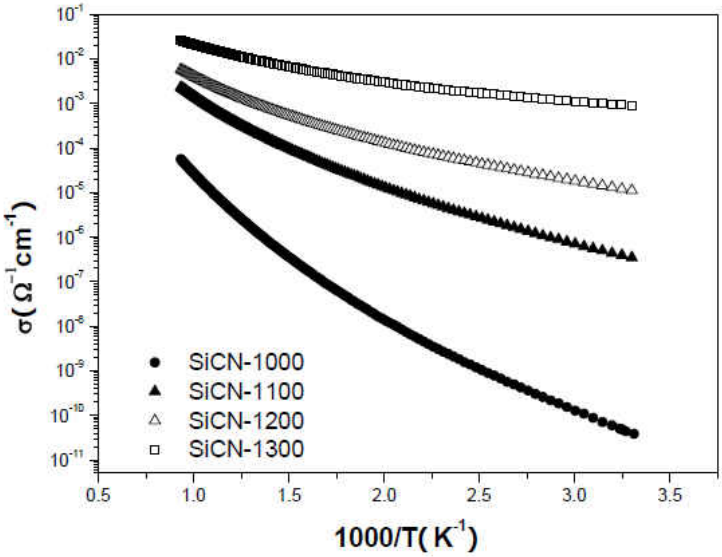

Figure 54: A plot of d.c.-conductivity of various SiCN materials as a function of 1000/T

The experimental results were also examined based on amorphous semiconducting theories. According to Mott and Davis [91], the temperature-dependent conductivity of amorphous semiconductors can be expressed using the following equation:

$$\sigma = \sigma_1 e^{-\frac{E_C - E_F}{kT}} + \sigma_2 e^{-\frac{E_A - E_F + w}{kT}} + \sigma_3 e^{-(\frac{T_o}{T})^{1/4}} \qquad (4.8)$$

The first term is the conduction in extended states; the second term is the thermal-assisted conduction in band tail states; the third term, according to Mott's original model [92], is the conduction around the Fermi level via variable range hopping (VRH). E_C, E_A and E_F are the extended band edge, the band tail and the Fermi level, respectively. w is the thermal activation energy, which is equal to the phonon energy of the material (neglecting multi-phonon processes).[91] σ_1, σ_2, and σ_3 are prefactors and T_o is the characteristic temperature for VRH. Equation (4.8) has been used to analyze the experimental results. A very good fit is obtained for all the samples in the whole range of testing temperature (Fig. 55). The parameters determined by curve fitting are summarized in Table 8.

The results reveal that pyrolysis temperature has remarkable effects on the band structure of the SiCNs. Both E_C-E_F and E_A-E_F+w decreased with increasing pyrolysis temperature, suggesting the E_F is moving closer to E_C and E_A with increasing pyrolysis temperature. Previous studies revealed that SiCN-based materials consist of carbon dangling bonds [93]. The dangling bonds work as donor defects to form defect states within the band gap. With increasing pyrolysis temperature, the concentration of the carbon dangling bonds increases, likely due to the rearrangement of carbon [93], leading to the increase in the density of the defect states. Consequently, the Fermi level moves toward the conduction band and band tail with increasing pyrolysis temperature, resulting in decrease of the gaps between E_F and E_C /E_A.

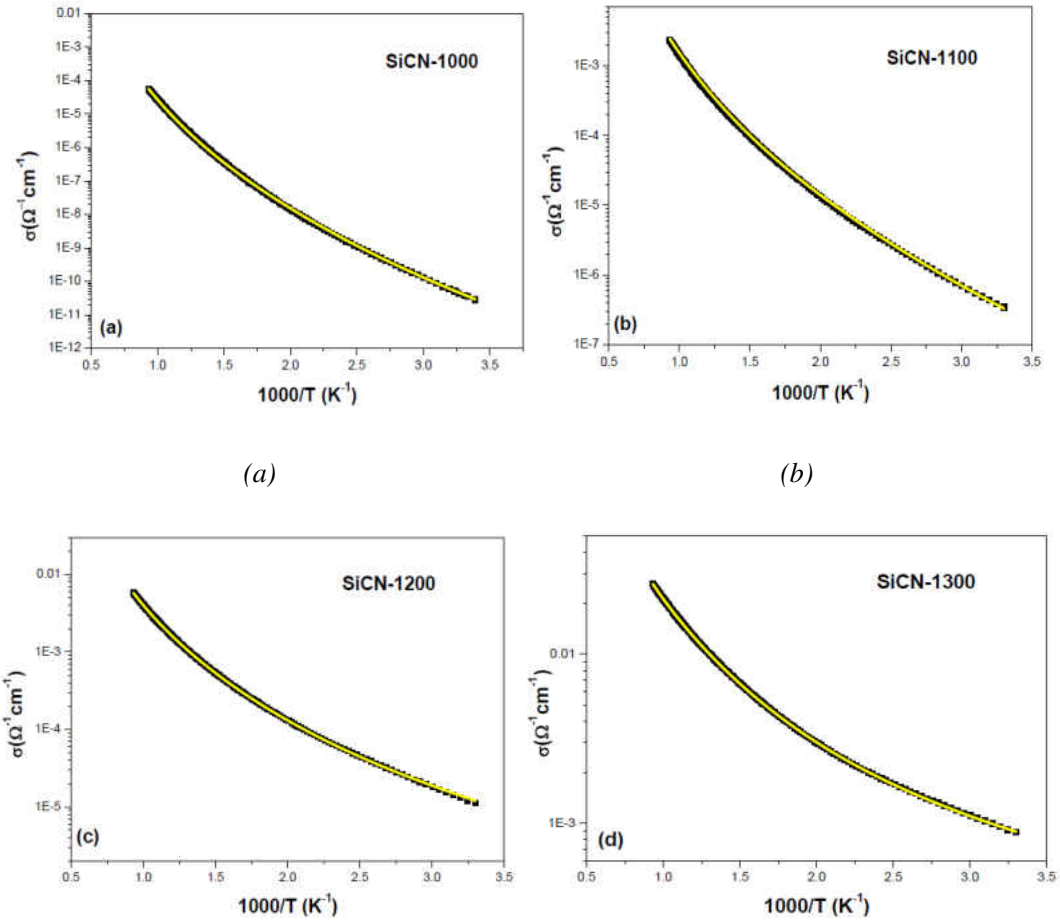

(a) *(b)*

(c) *(d)*

Figure 55: Comparison of experimental results and theoretical predictions-the temperature dependence d.c.conductivity of SiCN pyrolyzed at different temperature. The solid lines are computed from Eq. (4.5).

Table 8: Summary of the pyrolysis temperature and the conduction parameters obtained by curve fitting using equation (4.5)

Pyrolysis temperature (°C)	E_C-E_F (eV)	E_A-E_F-w (eV)	T_0 (K)	σ_3 ($\Omega^{-1}cm^{-1}$)
1000	1.03	0.71	$1.8x10^9$	$1.2x10^{11}$
1100	0.80	0.54	$2.9x10^8$	$0.6x10^6$
1200	0.75	0.52	$3.5x10^7$	$2.4x10^3$
1300	0.50	0.46	$1.2x10^6$	2.5

The energy difference between the edge of the extended states and the band tail is also estimated using the data in Table 8 by assuming w = 110meV[1)]. It is seen that E_C-E_A first decreased slowly with increasing the pyrolysis temperature up to 1200°C and then decreased steeply from 1200°C to 1300°C (Fig. 56). Nuclear magnetic resonance (NMR) studies revealed that the degree of the structural order of the SiCNs increased with increasing pyrolysis temperature, with a sudden change occurred between 1200 and 1300°C [94]. We, thereby, attribute the decrease in E_C-E_A to the increase in the structural order due to the formation of band tail states in amorphous semiconductors that is due to structural disorder[91].

It is interesting to note that both T_o and σ_3 decreased drastically with increasing pyrolysis temperature (Table 8). According to Mott's original model, these two parameters should change in opposite directions as a function of the density of states near the Fermi level, $N(E_F)$ [92]:

$$T_o \propto 1/N(E_F) \quad and \quad \sigma_3 \propto [N(E_F)]^{1/2} \qquad (4.9)$$

This obviously contradicts the experimental results. Recent theoretical studies consider a new transport mechanism, in which electrons near Fermi level fill empty electronic states near a so-called "transport energy" and then hop back to lower localized states, named

---

[1)] The w is the phonon energy of the SiCNs, which should be in the same range as those of SiC and Si_3N_4 phonons; and phonon energies are about 100meV for SiC[22] and 120meV for Si_3N_4[23].

band tail hopping conduction mechanism (BTH)[95, 96]. By considering the filling rate and assuming an exponential band tail states distribution, BTH model also suggests a $T^{-1/4}$ law.

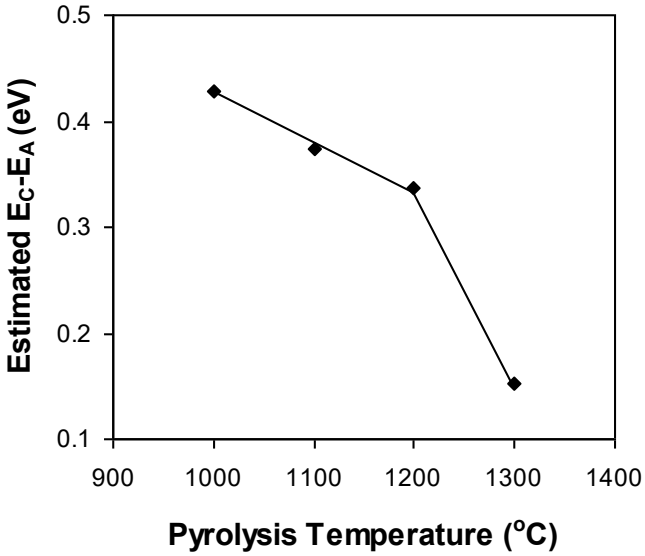

Figure 56: A plot of estimated E_C-E_A as a function of pyrolysis temperature.

Unlike VRH model, BTH model predicts that T_o and σ_3 should follow the following relationship [95, 97]:

$$\sigma_3 \propto \exp(T_o^{1/4}) \qquad (4.10)$$

Previous studies on amorphous carbons and carbon nitrides revealed that these covalent glasses followed the BTH mechanism, rather than hopping near Fermi level [98-100]. Figure 57 plots σ_3 as a function of $T_o^{1/4}$. A very good liner relationship suggests that the SiCNs studied should follow the BTH conduction mechanism at the low temperature range.

Every conducting mechanism of the three states shown in equation 4.8 has its own temperature range in which the respective state dominates the main mechanism. To get these

temperature ranges, the conductivity of the four SiCN samples is plotted against 1000/T and $1/T^{1/4}$, respectively. The curves are simulated by $\sigma = \sigma_0 + \sigma_1 \text{ Exp } (-E_1/KT) + \sigma_2 \text{ Exp } (-E_2/KT)$. The results are shown in figure 58 and starting temperature for thermal activation hopping mechanism is listed in table 9.

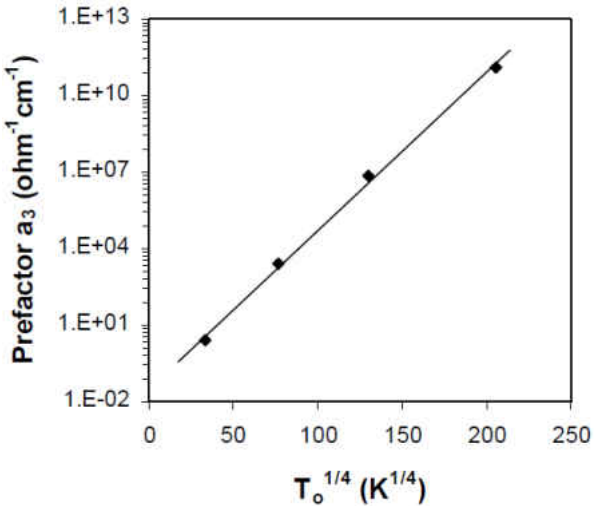

Figure 57: A plot of the prefactor σ_3 as a function of $T_o^{1/4}$ for all four samples.

According to the simulated results, the starting temperature for thermal activation hopping mechanism shift downward to lower temperature from 440ºC to 203ºC for samples pyrolyzed at 1000ºC to 1300ºC. With increasing annealing temperature, Fermi energy level E_F moves close to E_C, the edge of extended state. The active energy for electron hoping from localized state near Fermi energy level to band tail decrease. As a result, electrons in localized state of Fermi energy level can be activated into band tail at lower temperature. At the same time, the influence of band tail hopping conduction decreased and shifted away from the linear behavior at lower temperature.

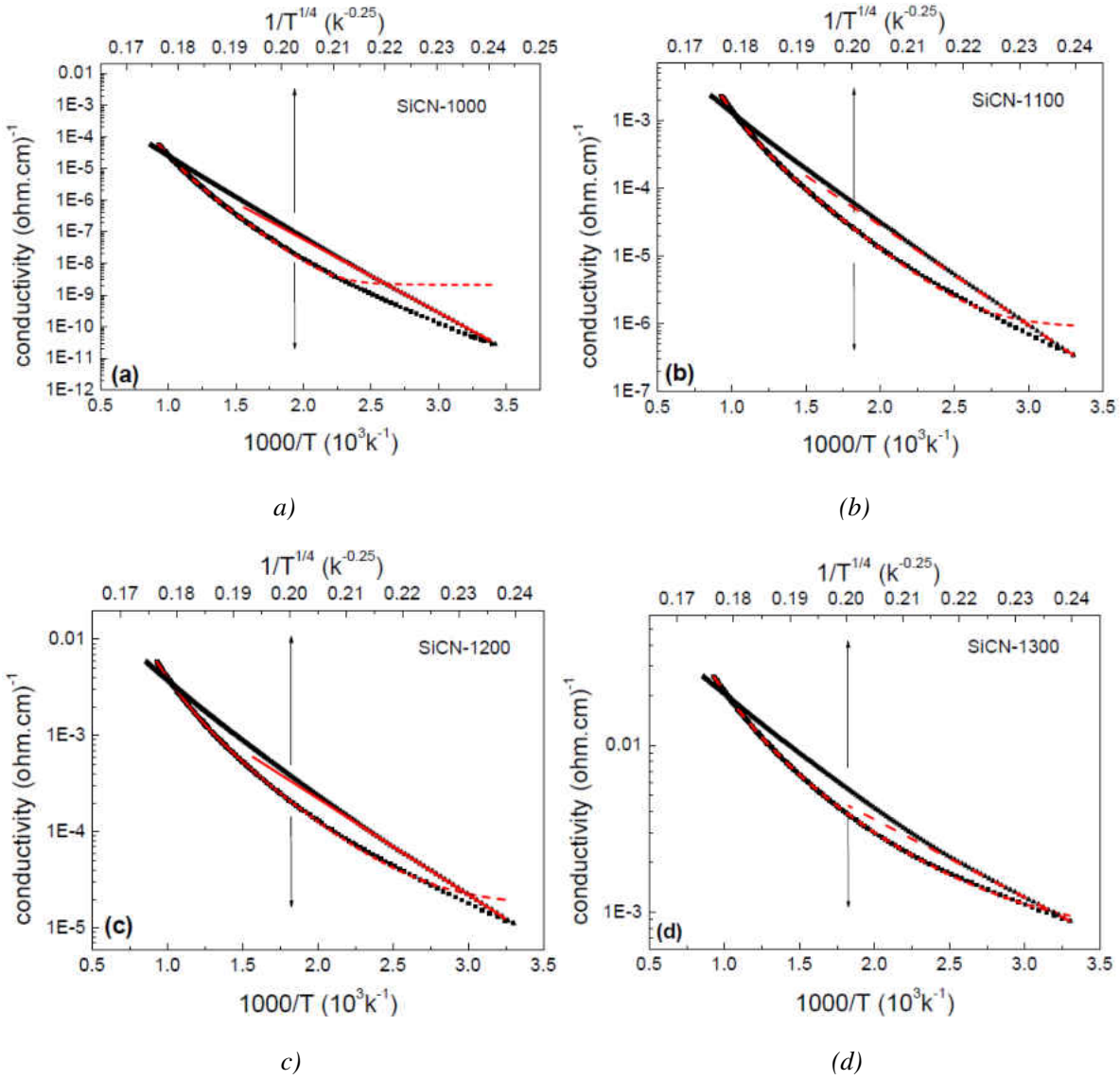

a) *(b)*

c) *(d)*

Figure 58: Conductivity plots as a function of 1000/T and $1/T^{1/4}$, respectively. Dash lines are simulation curve with equation: $\sigma = \sigma_0 + \sigma_1 \text{ Exp } (-E_1/KT) + \sigma_2 \text{ Exp } (-E_2/KT)$, and solid lines are standard lines for $\sigma \sim 1/T^{1/4}$. a) 1000 °C, b) 1100 °C, c) 1200 °C, and d), 1300 °C.

Table 9: Starting temperature for thermal activation hopping mechanism

	SiCN-1000	SiCN-1100	SiCN-1200	SiCN-1300
T (°C)	440	352	267	203

4.2.4 UV-Visible Light Absorption Spectrum

Figure 59 shows the relationship between absorption coefficient (α) and photon energy (hv) for the three SiCNs. For obtaining useful information about electronic structures, these original spectra are compared with theoretical models.

Tauc and co-workers [101-103] suggested that for amorphous semiconductors, the optical absorption spectra at a lower excitation energy range should follow

$$\alpha hv = B(hv - E_T)^n \qquad (4.11)$$

Where n is a constant with the value of ~ 1.5, E_T an energy gap (named Tauc band-gap), and B a constant. Inkson [104] suggested that this type of absorption is resulted from a transition between deep impurity trap and delocalized band (either conductive or valence band). Pfost *et al.* [103] also suggested that Tauc band-gap can be related to the electronic structures of amorphous semiconductors,

$$E_T = E_c - E_d \qquad (4.12)$$

where E_c is edge of extended conduction band (also called mobility edge) and E_d a deep defect level with a high density of state.

The equation (4.11) is used to analyze the spectra in figure 59. It is seen that the spectra within excitation energy range of 1.5 to 3.0eV can be well fitted by the equation (figure 60). The n values obtained by curve fitting are very close to the theoretical one (table 10). This suggests that the absorption of the SiCNs over the lower excitation energy range is

due to the transition between deep defect states and mobility edge. It is likely that the deep defect level (E_d) within the SiCNs is associated with carbon dangling bands [105], which have unpaired electrons. The Tauc band-gap values obtained by curve-fitting are also listed in table 10. It is seen that the band-gap significantly decreases with increasing the pyrolysis temperature.

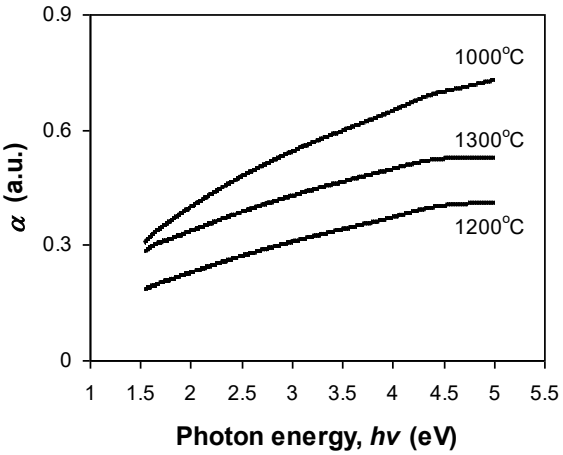

Figure 59: Room-temperature optical absorption spectra for the amorphous SiCNs pyrolyzed at different temperatures.

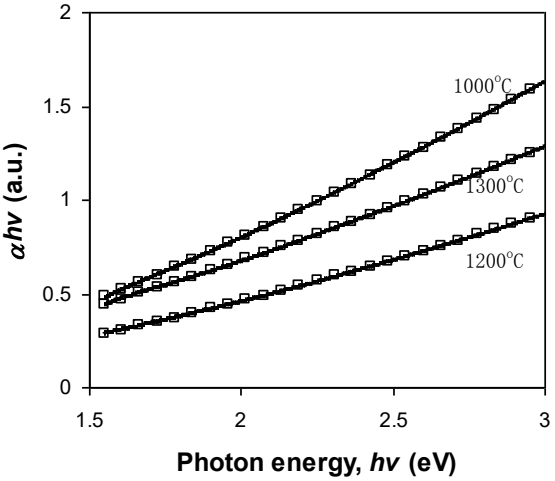

Figure 60: Plots of αhν as a function of photon energy for the three SiCNs. The solid lines are experimental data; the open symbols are curve fits using Eq. (4.11).

Table 10: Curve fit parameters for the three SiCNs.

Pyrolysis Temprature (°C)	n	E_{Tauc} (eV)	E_g (eV)
1000	1.41	0.55	2.95
1200	1.44	0.42	2.90
1300	1.44	0.21	2.75

Amorphous semiconductors can also exhibit a vertical optical transition between extended bands at higher excitation energy range [106]. This absorption can produce an absorption edge following the equation

$$(\alpha h\upsilon)^2 \propto (h\upsilon - E_g) \qquad (4.13)$$

where E_g is optical band gap, which is the difference between conduction band (E_c) and valence band (E_v). The absorption spectra of the SiCNs are re-plotted in the form of $(\alpha h\upsilon)^2$ versus $h\upsilon$ (fig. 61). It is seen that the absorption over the excitation energy range of 2.5 to 5.0eV can be well described by equation (4.13). The band gaps for the three SiCNs are estimated by extrapolation (dashed lines in fig. 61) to be 2.95, 2.90 and 2.75eV, respectively (table 10). Previous studies revealed that depending on their compositions and processing conditions, the optical absorption gaps for amorphous silicon oxide, silicon carbide and silicon nitride are 8eV [107], 2.4-3eV [108], and 2.5 to 4eV [109], respectively. The obtained band gaps of the SiCNs, which consisted of mixed $SiC_{x+4}N_y$ tetrahedra, are within these ranges. The decrease in the band gap with increasing pyrolysis temperature suggests structural evolutions with increasing pyrolysis temperature. Such structural evolutions have been widely observed for polymer-derived amorphous ceramics [110].

Based on the above results, the electronic structures of the SiCNs can be deduced, which are schematically shown in Figure 62. It is interesting that the defect-associated state level (E_d) increases with increasing the pyrolysis temperature. Since the defect level is associated with C-dangling bands, the increase in the level indicates that increase in the concentration of C-dangling bands. Such increase in C-dangling band with pyrolysis temperature had been widely observed in polymer-derived ceramics [110].

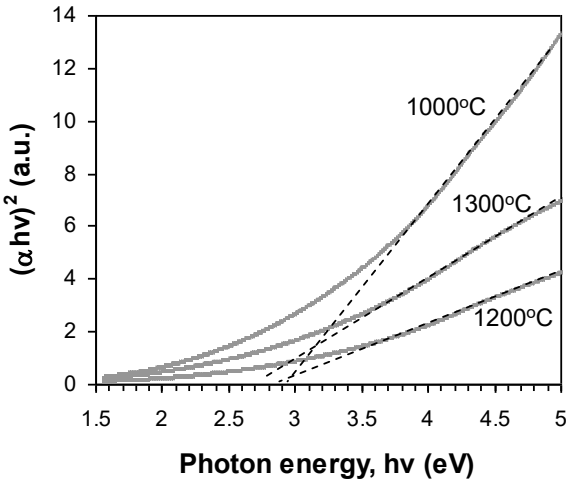

Figure 61: Plots of $(\alpha hv)^2$ as a function of photon energy for the three SiCNs.

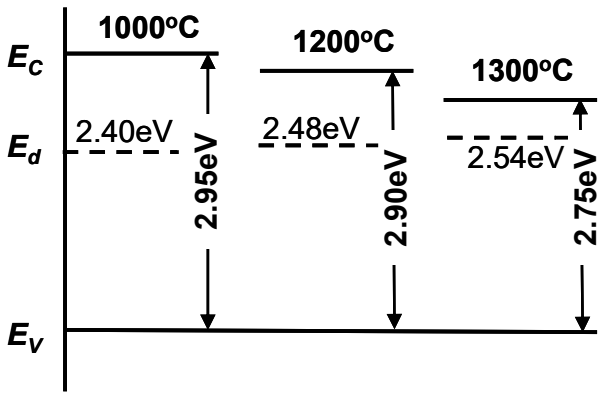

Figure 62: Schematic shows the electronic structures of the SiCNs as a function of the pyrolysis temperature.

4.3 Summary

The electrical property of SiCN ceramics can be interpreted by amorphous semi-conductor mechanism. The d.c. conductivity of these materials increased with increasing annealing temperature and showed a linear behavior, indicating that there is an equilibrium reaction which produced the charge carrier thus decided the conduction process. The starting material of MA retarded the equilibrium reaction and decreased the conductivity of the samples for a minor addition of lower than 6%. However, the conductivity was found to increase with increased addition of MA (>6%). The conductivity of SiCNs increased with testing temperature, indicating the materials has the semi-conductor process behavior. With increasing annealing temperature, the Fermi energy level moves to conduction band edge and more electrons can be activated from localized states on Fermi energy level to band tail states and extended states, resulting in an increased conductivity. At low temperature, the conductivity was decided by band tail hopping conduction mechanism (BTH) other than variable range hopping on Fermi level. The UV-Vis-absorption spectra were also used to study the electrical structure of SiCN samples. The optical band gap, which is the difference between conduction band (E_c) and valence band (E_v), decreased with increasing annealing temperature. Defect-associated state level (E_d) also increased with increasing pyrolysis temperature, indicating the increase in the concentration of C-dangling bands.

CHAPTER FIVE: DIELECTRONIC PROPERTY OF POLYMER DERIVED SiCN CERAMICS

In this chapter, impedance and dielectric properties of SiCN ceramics were carried out using LF impedance analyzer (Model HP4294, Agilent, Palo Alto, CA) over a range of frequencies (100Hz – 110 MHz). The impendence spectra of these samples showed two semi-circular arcs and their equivalent electrical circuit can be expressed as one which comprised a series combination of two parallel resistance and capacitance circuits, indicating there are two phases in SiCN ceramics. Dielectric constants of the materials increased with increasing annealing temperature, indicating the space charge, i.e. the ions and electrons adjacent to defects, increased due to increased defect concentration at higher annealing temperature.

5.1 Introduction

5.1.1 Impendence Spectrum Measurement

Impedance technique was related to a well-developed branch of ac theory concerned with the response of a given circuit to an ac voltage as a function of frequency. For an ac, a voltage E (volts) applied to a circuit, the resultant current I (amps) measured, and the impedance Z (ohms) can be related using following:

$$E = IZ \qquad (5.1)$$

Here, the impedance Z is the ac equivalent of resistance. The vector expression for ac impedance is:

$$Z\ Total = Z' + j\ Z'' \qquad (5.2)$$

Here, Z' is the real part of the impedance vector, j Z'' is the imaginary part, and $j=\sqrt{-1}$. The absolute magnitude of the impedance vector can be expressed as:

$$Z = [(Z')2 + (Z'')2]\ 1/2 \qquad (5.3)$$

and the phase is defined by:

$$\tan\theta = Z''/Z' \qquad (5.4)$$

The impedance measurements of a material give us data having both resistive (real part) and reactive (imaginary part) components, which can provide a true picture of the material properties.

Phenomenologically, a resistance (R) represents the dissipative component of the dielectric response, while a capacitance (C) and inductor (L) describe the storage component of the material. The overall admittance of a parallel (RC) circuit is given by the sum of conductance and capacitance contributions:

$$(1/Z) = (1/R) + (j\omega C) \qquad (5.5)$$

The complex impedance can be separated into real and imaginary parts by algebraic rules:

$$Z\ real = (R/[1+(\omega RC)^2]$$

$$Z_{img} = -(\omega R^2 C\,[1 + (\omega RC)^2]) \qquad (5.6)$$

The overall impedance of series of circuit (RL) is given by the sum of resistance and inductor contributions,

$$Z = R + j\omega L \qquad (5.7)$$

Analysis of the impedance data is often carried out using the Nyquist plot ($-Z_{img}$ vs Z_{real}).

5.1.2 Dielectric Constant and Loss Measurement

Dielectric is the study of dielectric materials and involves physical models to describe how an electric field behaves inside a material. When a dielectric material is put under an external electric field, four kinds of electrical polarization can happen within materials including 1) electronic polarization, 2) ionic polarization, 3) dipolar orientation polarization, and 4) space change (thermal ions relaxation) polarization. These polarizations happen at different electric field frequency range and electrical charge will be accumulated in different site of materials, thus produce an internal electric field inside of dielectric materials. The ability of dielectric materials to polarize in response to the field and then affect external electric field to each other can be described by electric constant which is defined by equation 5.8:

$$\varepsilon_r = \frac{C}{C_0} \qquad (5.8)$$

Where, ε_r is dielectric constant, C is the capacitance of the capacitor with dielectric and C_0 is the capacitance of the capacitor without dielectric materials.

The process of polarization need time to be performed. This time was named relaxation time, defined by equation 5.9.

$$\tau = \frac{1}{2\upsilon} e^{U/kT} \qquad (5.9)$$

Where τ is relaxation time, ν is vibration frequency of ions, U is thermal activation energy of ions, k is Boltzmann constant and T is temperature.

When polarizations cannot follow up the frequency change of electric field, the electrical energy will be dissipated as heat. This is so-called dielectric loss, which is defined as equation 5.10.

$$\tan\delta = \frac{I_a}{I_r} \qquad (5.10)$$

Where tan δ is dielectric loss, I_a is active component and I_r is reactive component.

5.2. Experiment Procedure

Two faces of square shaped SiCN samples (10mm × 10mm × 0.5mm) were polished with 600 grit SiC paper and washed in acetone under ultrasonication for 5 minutes. The polished faces were coated with conductive silver paste and dried under IR light for one hour.

Impedance measurements were carried out using LF impedance analyzer (Model HP4294, Agilent, Palo Alto, CA) over a range of frequencies (100 Hz –110 MHz) and dielectric constant and loss also were tested with the same instrument over a range of frequencies (100 Hz –40 MHz).

5.3. Results and Discussion

5.3.1. Impedance Measurement

Figure 63 shows the impedance spectra of SiCN ceramics pyrolyzed at different temperature from 1100 to 1300 ºC. All impedance spectra are characterized by the appearance of two semicircular arcs. Similar impedance spectra observed for SiCN 1100 ~1300 ºC indicated the microstructures for these SiCN simples are similar. Two semicircular arcs in the impedance pattern of SiCN-1100 ~ 1300 ºC can be modeled in terms of an equivalent electrical circuit, which comprised a series combination of two parallel resistance and capacitance circuits. The equivalent electrical circuit for these ceramic samples is shown in Figure 64. The values of circuit elements can be obtained by curve fitting the impedance spectra. The results are list in Table 11.

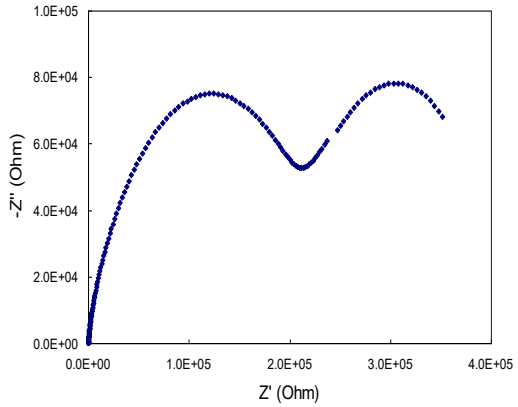

(a)

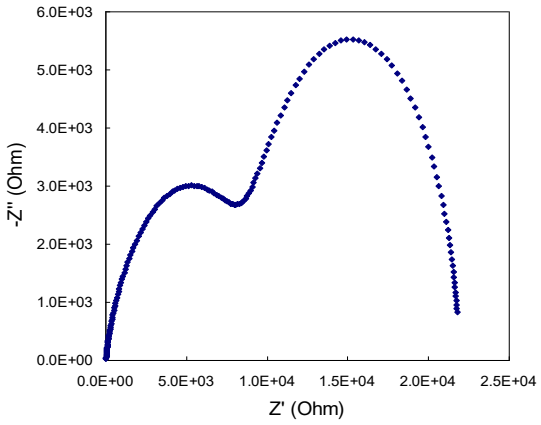

(b)

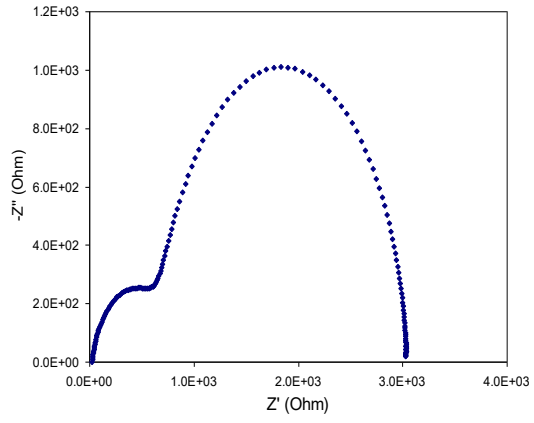

(c)

Figure 63: Impedance measurement of SiCN fully dens sample annealed at different temperature: (a) 1100 ºC, (b) 1200 ºC, and (c) 1300 ºC.

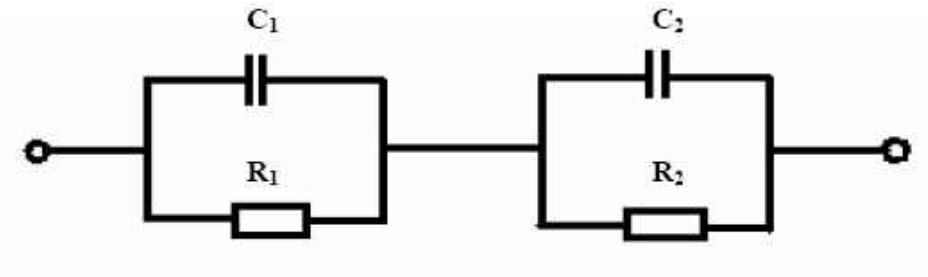

Figure 64: The equivalent circuits of SiCN fully dense samples annealed at temperature 1100, 1200, 1300 ºC.

Table 11: The simulated parameters for impedance spectra of SiCN samples pyrolyzed at different temperature.

	R_1 (Ω)	C_1(F)	R_2 (Ω)	C_2(F)
SiCN-1100	2.37E06	3.40E-11	2.53E06	2.26E-09
SiCN-1200	1.11E05	6.97E-11	1.49E05	4.45E-09
SiCN-1300	6.68E03	1.01E-10	2.03E04	3.27E-09

The two semicircular arcs of SiCN samples revealed that these materials have two phases, i.e. Si-C-N matrix and free carbon phase. The parameters of the first loop in the high-frequency region, R_1 and C_1, can be ascribed to Si-C-N matrix whose resistivity decreased with pyrolysis temperature due to increasing content of dangling bond, which could be proved by EPR result. The parameters of the second loop in the low-frequency region, R_2 and C_2, can be assigned to free carbon phase because, according to results obtained by Raman spectroscopy, the free carbon composition decreased with increasing temperature, thus the resistivity should also be decreased. In addition, the resistivity of first loop decreased faster than that of the second loop, indicating that the Si-C-N matrix plays a more important role than free carbon in conduction property of the samples at higher annealing temperature.

5.3.2 Dielectric Constant and Loss Measurement

5.3.2.1 Frequency Dependence of Dielectric Constant and Loss

Figure 65 shows the dielectric constant and loss of SiCN samples pyrolyzed at different temperature from 1100 to 1300 ºC change with frequency over range of 100 Hz to 40 MHz. The dielectric constants of these samples within this frequency decreased with increasing frequency and no maximum value could be found. The dielectric constants are mainly aroused from space charge polarization in which the ions and electrons adjacent to defects are activated and moved to interface of different phases. The space charge polarization was decided by the number of ions and electrons near to defects within SiCN samples. So it is not hard to understand that at same frequency, the dielectric constants of these samples increased with increasing of annealing temperatures shown in figure 65. The samples pyrolyzed at higher temperature can provide more defects like dangling bonds within matrix, which was proved by results measured by EPR, resulting in more ionic and electronic relaxation polarizations and higher dielectric constant.

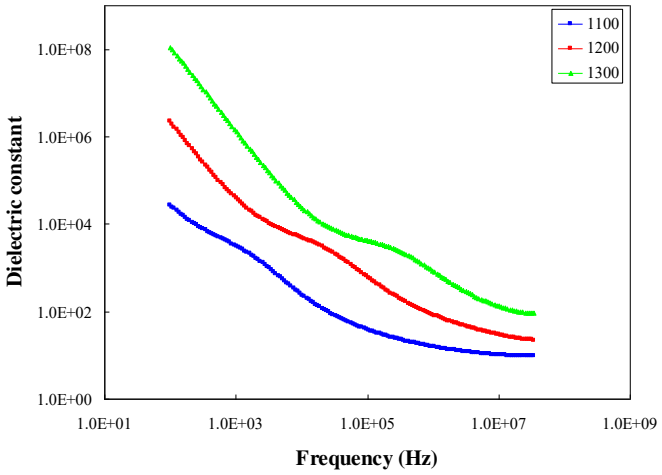

(a)

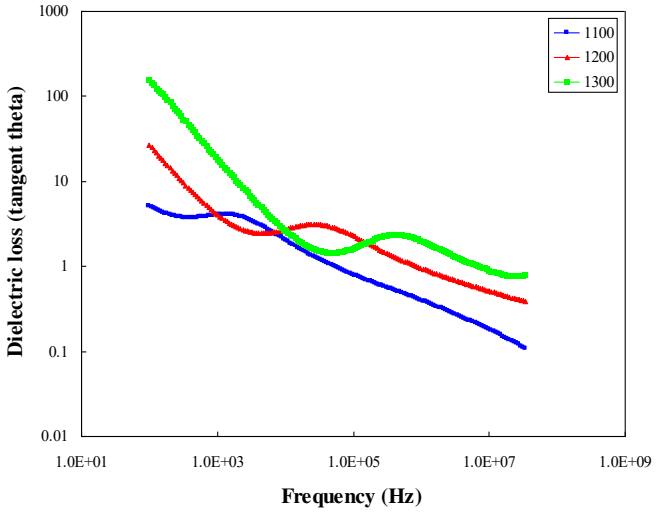

(b)

Figure 65: Dielectric constants and loss of various SiCN samples change with electric field frequency, (a) dielectric constant, and (b) dielectric loss

In figure 65 (b), the dielectric loss of these three samples has maximum value, which is the sign of ionic relaxation polarization. The relaxation time, τ, can be calculated by the frequency corresponding to the maximum value of constant according to equation 5.11.

$$\omega \tau = 1 \qquad (5.11)$$

The results are shown in table 12. The relaxation time of these samples are in typical range of ionic relaxation polarization of $10^{2} \sim 10^{8}$ s and decreased with increasing pyrolyzed temperature, indicating that the polarization can happen easier for samples annealed at higher temperature, which has more defects and lower activation energy.

Table 12: Ionic polarization relaxation time of SiCN samples annealing at different temperature

	Ω (Hz)	τ (s)
SiCN-1100	1.38E03	7.23E-04
SiCN-1200	3.05E04	3.28E-05
SiCN-1300	4.55E05	2.20E-06

5.3.2.2 Temperature Dependence of Dielectric Constant and Loss

Figure 66 shows the temperature dependence of dielectric constant and tangent loss of sample SiCN-1200 measured at frequency of 1, 10, and 100 KHz over temperature range of 20 ~ 675 °C, respectively. Generally, dielectric constant increases with temperature first and then decreases after reaching a maximum value. At the temperature corresponding to the maximum constant, relaxation polarization has been fully reached when the polarization relaxation time equals to electric filed period. The relaxation time has a maximum value, which is at temperature lower than temperature corresponding to the maximum constant. In

figure 66 (a), there is a minimum value of dielectric constant at temperature of 267 ºC, which separates the curve into two parts. These two parts might be related to two kinds of defects, i.e., Si-related dangling bond and C-related dangling bond within the samples, which was proved by EPR results in our study. The ions near to these two kinds of defects have different thermal activation energy, which can be polarized at different temperature range.

The part at temperature range lower than 267ºC has a maximum constant at temperature of 215ºC for 100 KHz electrical field. Its corresponding tangent loss has a maximum value at temperature of 110 ºC, which is lower than 215 ºC, the temperature of the maximum dielectric constant.

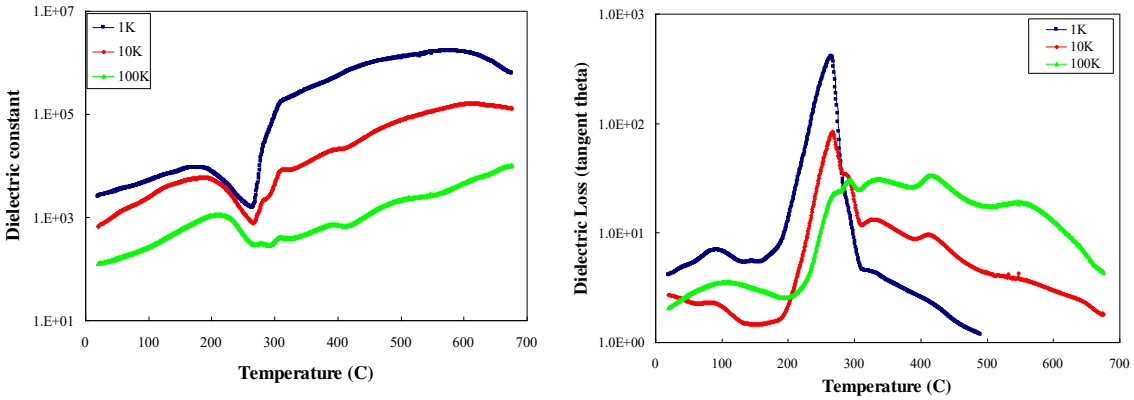

(a) *(b)*

Figure 66: Temperature dependence of (a) dielectric constant, and (b) tangent loss of sample SiCN-1200 measured at frequency of 1, 10, and 100 KHz over temperature range of 20 ~ 675 ºC.

The part at temperature range higher than 267ºC has more than one maximum dielectric constant and same number of minimum constant values which are listed in table 13. Meanwhile, several maximum values of dielectric loss and susequently the same number of relaxation times can be found in figure 66 (b). The corresponding temperatures also are listed in table 13.

Table 13: Temperature dependence of dielectric constant and loss parameters of SiCN samples annealed at 1200ºC in 100 KHz electrical field.

	T (°C)	T (°C)	T (°C)	T (°C)	T (°C)
Constant Max Peak	282	313	395	495	618
Constant Min Peak	271	296	339	420	562
Loss Max Peak	273	295	339	420	554

There are five sets of parameters in table 13, indicating that there are at least five types of defect centers that could be activated at higher temperatures for SiCN ceramics. As measured by NMR, there are various chemistry units including $SiCO_3$, SiN_2O_2, $SiCN_3$, SiC_2N_2, and $SiCN_3$, etc. in amorphous SiCN samples. The Si- and C-related dangling bond can be in any one of these units. The polarization relaxation times of ions near to these dangling bonds are different thus the maximum values of dielectric loss can be found at different temperature. It is normal that the temperatures of dielectric loss maximum peaks are lower than that of constant maximum peaks. Interestingly, the temperatures of dielectric loss maximum peaks are almost similar to that of constant minimum peaks at which, as we

believe, a new ions provider is activated. The loss reaching its maximum value at this temperature not only is provided by ions relaxation loss, but also is influenced by conduction loss.

5.4. Summary

The impendence spectra of these samples have two semi-circular arcs and their equivalent electrical circuit can be expressed as one which comprised a series combination of two parallel resistance and capacitance circuits, indicating there are two phases in SiCN ceramics. Dielectric constants of the materials increased with increasing annealing temperature, indicating the space charge density, i.e. the ions and electrons near to defects, increased due to more defects at higher annealing temperature. The relaxation time of SiCN materials decreased with annealing temperature, also indicating the increased defect density at higher temperature. In addition, several kinds of defects related to Si- and C- bond can provide ions relaxation polarization at different temperature.

CHAPTER SIX: CONCLUSION

From the discussion aforementioned, the following conclusions can be drawn:

1) Amorphous SiCN ceramics were fabricated at a temperature range of 1000 ~ 1350ºC, which has uniform structure. These materials possess two phases including free carbon domains and Si-C-N matrix. Free carbon phase with ring-like configurations was found to be dispersed in Si-C-N ceramics as glassy form. With increasing pyrolysis temperature, the structure of free carbon was rearranged into aromatic graphene layers and resulted in more ordering. The domain size of free carbon increased with increasing annealing temperature, whereas the free carbon concentration was found to decrease due to its nature to dissolve back into Si-C-N matrix. The Si-C-N matrix has some chemistry units including $SiCO_3$, SiN_2O_2, $SiCN_3$, SiC_2N_2, and SiC_3N. With increasing pyrolysis temperature, the structure and composition of these units were also changed. Number of unit $SiCO_3$, SiC_2N_2, and SiC_3N increased while SiN_2O_2, $SiCN_3$ decreased. In addition, the dangling bond within Si-C-N matrix related to Si- and C- bond increased with annealing temperature, which could alter the electrical property of these materials.
2) The electrical property of SiCN ceramics can be interpreted by amorphous semi-conductor mechanism. The d.c. conductivity of these materials increased with increasing annealing temperature and also showed a linear behavior, indicating that

there is an equilibrium reaction, which produced the charge carrier and thus decided the conduction process. With increasing annealing temperature, the Fermi energy level moved to conduction band edge and more electrons could be activated from localized states on Fermi energy level to band tail states and extended states, resulting in an increased conductivity. At lower temperature, the conductivity was decided by band tail hopping conduction mechanism (BTH) other than variable range hopping on Fermi level. The optical band gap, which is the difference between conduction band (E_c) and valence band (E_v), decreased with increasing annealing temperature. Defect-associated state level (E_d) also increased with increasing pyrolysis temperature, indicating the increase in the concentration of C-dangling bands.

3) The impendence spectra of these samples have two semi-circular arcs, indicating there are two phases in SiCN ceramics. Dielectric constants of the materials increased, whereas the relaxation time decreased with increasing annealing temperature, indicating the space charge, i.e. the ions and electrons near to defects, increased due to more defects at higher annealing temperature. In addition, several kinds of defects related to Si- and C- bond can also provide ions relaxation polarization at different temperature.

LIST OF REFERENCE:

1. Edwin Kroke, Ya-Li Li, Christoph Konetschny, Emmanuel Lecomte, Claudia Fasel, Ralf Riedel, "Silazane derived ceramics and related materials", *Materials Science and Engineering*. *26*, 97-199(2000)
2. Stephan Trassl, Manfred Puchinger, Ernst Ro¨ ssler, Gu¨ nter Ziegler, "Electrical properties of amorphous SiCxNyHz-ceramics derived from polyvinylsilazane", *Journal of the European Ceramic Society 23*, 781–789(2003)
3. K.J. Wynne and R.W. Rice, "Ceramics via Polymer Pyrolysis," *Annu. Rev. Mater. Sci. 14*, 397-334 (1984)
4. D. Seyferth, In *Inorganic and Organometallic Polymers*, edited by M. Zeldin, K.J Wynne, H.R. and Allcock. ACS Symposium Series 360, American Chemical Society, Washington DC, 1988.
5. M. Birot, J.P. Pillot, and J. Dunogues, "Comprehensive Chemistry of Polycarbosilanes, Polysilazanes, and Polycarbosilazanes as Precursors of Ceramics," *Chem. Rev. 95*, 1443-1477 (1995).
6. D. Seyferth, in: *Euro-Ceramics* 2, Vol. 1, edited by G. Ziegler and H. Hausner, Deutsche Keramische Gesellschaft e. V.,Augsburg, 1991.
7. N.S. Choong Kwet Yive, R.J.P. Corriu, D. Leclerq, P.H. Mutin, A. Vioux, *Chem. Mater. 4*, 141(1992)

8. D. Seyferth, C. Strohniann, H. J. Tracy, and J. L. Robinson, "Synthesis and Useful Reactions of Organosilicon Polymeric Precursors for Ceramics," *Mater. Res. Soc. Symp. Proc. 249*, 1-14 (1992).

9. J. Bill, J. Seitz, G. Thurn, J. DuÈrr, J. Canel, B.Z. Janos, A. Jalowiecki, A. Sauter, S. Schempp, H.P. Lamparter, J. Mayer, F. Aldinger, Phys. Stat. Solidi (a) 166, 269(1998)

10. N.S. Choong, R.J.P. Corriu, D. Leclercq, P.H. Mutin, and A. Vioux, "Thermogravimetric Analysis/Mass Spectrometry Investigation of the thermal Conversion of Organosilicon Precursors into Ceramics under Argon and Ammonia," *Chemistry of Materials, 4*, 1263-71 (1992)

11. R.J.P Corriu, "Ceramic and Nanostructures from Molecular Precursors," *Angewdante Chemie- International Edition, 39*, 1376-98 (2000)

12. M. Weinmann, "High Temperature Stable Ceramics from Inorganic Polymers," in *Polymer Derived Ceramics*, edited by J. Bill, F. Wakai, and F. Aldinger, Wiley-VCH Verlag Gmbh, Weinheim, Germany 1999

13. R. Riedel, H.J. Kleee, H. Schbrifelder, and F. Aldinger, " A covalent Micro/ Nano Composite Resistant to High temperature Oxidation*," Nature, 374*, 526-28 (1995)

14. J. LuÈcke, J. Hacker, D. Suttor, G. Ziegler, "Synthesis and Characterization of Silazane-based Polymer as Precursors for Ceramic Matrix Composites," *Appl. Organomet. Chem. 11*, 181-194(1997).

15. Y.L.Li, E. Kroke, R. Riedel, C. Fasel, C. Gervais, F. Babonneal, " Thermal

cross-linking and pyrolytic conversion of poly(ureamethylvinyl)silazanes to silicon-based ceramics". *Appl. Organometal .chem. 15*, 820-832(2001)

16. S. Johnson, *The Si-Al-O-N System -- Thermodynamic Properties and Phase Diagrams*, Report of the Division of Physical Metallurgy, Royal Institute of Technology, Stockholm, Sweden, 1991

17. R. Riedel, G. Passing, H. SchoÈnfelder, and R.J. Brook, "Synthesis of dense silicon-based ceramics at low temperatures", *Nature 355*, 714-717(1992).

18. J. Seitz and J. Bill, "Production of Compact Polysilazane-derived Si/C/N-ceramics by Plastic Forming," *J. Mater. Sci. Lett. 15*, 391-393(1996)

19. P. Greil, "Near Net Shape Manufacturing of Polymer Derived Ceramics," *J. Eur. Ceram. Soc. 18*, 1905-1914(1998)

20. T. Erny, M. Seibold, O. Jarchow, and P. Greil, "Microstructure Development of Oxycarbide Composites during Active-filler-controlled Polymer Pyrolysis," *J. Am. Ceram. Soc. 76,* 207-213(1993).

21. L. An, Y. Wang, L. Bharadwaj, L. Zhang, Y. Fan, D. Jiang, Y.H. Sohn, V.H. Desai, J. Kapat, and L. C. Chow "Silicoaluminum carbonitride with anomalously high resistance to oxidation and hot corrosion," *Adv. Eng. Mater.* 6(5), 337-340 (2004).

22. M.Monthioux, O.Delverdier, "Thermal Behavior of (Organosilicon) Polymer-Derived Ceramics .5. Main Facts and Trends,"*J.Eur. Ceram.Soc. 16,* 721-37 (1996)

23. M. Peuckert, T. Vaahs, M. Brück, "Ceramics from Organometallic Polymers,"*Adv.*

Mater. **2** 398-404 (1990)

24. C.Gerardin, F. Taulelle, J. Livage, "Pyrolysis of a Polyvinylsilazane,Polymeric Precursor for Silicon Carbonitride - Structural Investigation by H-1, C-13, Si-29, N-15 and N-14 Nuclear-Magnetic-Resonance,"*Journal de Chimie Physique et de Physico-Chimie Biologique*, *89 (2)* 461-7 (1992)

25. Y.Sasaki, Y.Nishina, M.sato, K.Okamura, "Raman study of SiC fibres made from polycarbosilane,"*J. Mater.Sci*. **22** 443 -8 (1987)

26. R.M.Laine, F.Babonneau, K.Y.Blowhowiak, R.A.Kennish, J.A.Rahn, G.J.Exarhos, K.Waldner, "Group - II Tris(glycolato) Silicates as Precursors to Silicate-glassed and Ceramics," *J.Am.Cerm.Soc*. **78** 529-38 (1995)

27. D. Bahloul, M.Pereira, P.Goursat, "Preparation of Silicon Carbonitrides from an Organosilicon Polymer: 2. Thermal-Behavior at High-Temperature under Argon," *J.Am.Ceram.Soc*. **76** 1163-8 (1993)

28. G.T.Burns, R.B.Taylor, Y.Xu, A.Zangvil, G.A.Zank, "High-temperature Chemistry of The Conversion of Siloxanes to Silicon-Carbide,"*Chem. Mater*. **4** 1313-23 (1992)

29. G.D.Soraru,G.D'Andrea,R.Campostrini,F.Bahonneau,G.Mariotto,"Structural Characterization and High-Temperature Behavior of Silicon Oxycarbide Classes Prepared from Sol-Gel Precursors Containing Si-H Bonds," *J.Am.Ceram.Soc*.**78** 379-87(1995)

30. J.Durr, Sehempp, P.Lamparter, J.Bill, S.Steeb, F.Aldinger, "X-ray and neutron small

angle scattering with Si-C-N ceramics using isotopic substitution,"*Solid state Ionics* **101**, 1041-7 (1997)

31. G. Gregori, H.-J. Kleebe, H. Brequel, S. Enzo, G. Ziegler, "Microstructure evolution of precursors-derived SiCN ceramics upon thermal treatment between 1000 and 1400°C,"*Journal of Non-Crystalline Solids 351* 1393–402 (2005)

32. Q. D. Nghiem, J. K. Jeon, L.Y. Hong, D. P. Kim, *Journal of organometallic chemistry.* 688, 27-35(2003)

33. J. Cordelair, P. Greil, ''Electrical Conductivity Measurements as a Microprobe for Structure Transitions in Polysiloxane Derived Si–O–C Ceramics,'' *Journal of the European Ceramic Society.* 20, 1947-1957(2000)

34. A. Saha, R. Raj, D. L. Williamson, ''A Model for the Nanodomains in Polymer-Derived SiCO," *J. Am. Ceram. Soc.* 89[7], 2188-2195(2006)

35. T. Varga, A. Saha, R. Raj, D. L. Williamson, ea al, *J. Am. Ceram. Soc.* 90[10], 3213-3219(2007)

36. S. Traßl, G. Motz, E. Ro¨ssler, G. Ziegler, "Characterisation of the free-carbon phase in precursor-derived SiCN ceramics," *J. Non-Cryst. Solids* **293** 261-7 (2001)

37. C. Haluschka, C. Engel, R. Riedel, "Silicon carbonitride ceramics derived from polysilazanes Part II. Investigation of electrical properties", *Journal of the European Ceramic Society 20,* 1365-1374 (2000)

38. D.Galusek, S.Reschke, R. Riedel, W. Dreûler, P. Sajgalik, Z. Lences and J. Majling,

"In-Situ Carbon Content Adjustment in Polysilazane Derived Amorphous SiCN Bulk Ceramics", *Journal of the European Ceramic Society 19*, 1911-1921(1999)

39. A. M.Hermann, Y.Wang and R.Riedel, "Structure and Electronic Transport Properties of Si-(B)-C-N Ceramics"J.*Amer.Ceram.Soc*.**84**, (10), 2260-5 (2001)

40. L. Liew, R.A. Saravanan, V. M. Bright, M. L. Dunn, J. W. Daily, R. Raj, "Processing and characterization of silicon carbon-nitride ceramics: application of electrical properties towards MEMS thermal actuators", *Sensors and Actuators A 103,* 171–181(2003)

41. C.Haluschka, H.J.Kleebe, R.Franke, R.Riedel, "Silicon carbonitride ceramics derived from polysilazanes Part I. Investigation of compositional and structural properties", *Journal of the European Ceramic Society 20,* 1355-1364(2000)

42. L. An, R. Riedel, C. Konetschny, H.-J. Kleebe, and R. Raj, "Newtonian Viscosity of Amorphous Silicon Carbonitride at High Temperature," *J. Am. Ceram. Soc. 81*, 1349-1352(1998).

43. R. Riedel, L.M. Ruwisch, L. An, and R. Raj, "Amorphous Silicoboron Carbonitride Ceramic with Very High Viscosity at temperatures above 1500℃" *J. Am. Ceram. Soc. 81*, 3341-3344(1998)

44. T. Hirai, K. Nihara and T. Goto, "Oxidation of CVD Silicon Nitride (Si3N4) at 1550 °C to 1650 °C,"*J. Am. Ceram. Soc*. **63** (7-8) 419-24 (1980)

45. S.R. Elliott, "a.c. conduction in amorphous chalcogenide pnictide semiconductors",

Adv. Phys. 36(2), 135-218(1987)

46. N.F.Mott, "Conduction in Non-Crystalline Systems.5. Conductivity,Optical Absorption and Photoconductivity in Amorphous Semiconductors,"*Philosophical Magazine*, **22** (179) 903-& (1970)

47. P.W.Anderson, "Absence of Diffusion in Certain Random Lattices,"*Physical Review* **109** 1492-505 (1958)

48. N.F.Mott, "Conduction in Non-Crystalline Materials. 3. Localized States in A Pseudo gap and Near Extremities of Conduction and Valence Bands,"*Philosophical Magazine*, **19** (160) 835-& (1969)

49. http://en.wikipedia.org/wiki/Raman_spectroscopy

50. F. Tuinstra, J.L. Koening, "Raman spectra of graphite," J. Chem. Phys. 53 (1970) 1126

51. http://www.jobinyvon.com/usadivisions/Raman/applications/Carbon01.pdf

52. A.C. Ferrari, J. Robertson, "Interpretation of Raman spectra of disordered and amorphous carbon", Phys. Rev. B 61 (2000) 14095

53. D.S. Knight and W.B. White, "Characterization of diamond films by Raman spectroscopy," *J. Mater. Res*., **4**, 385-393 (1989).

54. M.J. Mathews, M.A. Pimenta, G. Dresselhaus, M.S. Dresselhaus and M. Endo, "Origin of dispersive effects of the Raman *D* band in carbon materials," *Phys. Rev. B*, **59**, R6585-6588 (1999).

55. http://en.wikipedia.org/wiki/Electron_paramagnetic_resonance

56. S. I. Andronenko, I. Stiharu, S. K. Misra, "Synthesis and characterization of polyureasilazane derived SiCN ceramics", *J. App. Phys.,* 99, 113907 (2006)

57. M. R. Mucalo, D. G. Mcgavin, N. B. Milestone, "Electron spin resonance studies of amorphous and crystallized residues derived from pyrolysis of pre-ceramic polymers", *J. Mater. Sci.*, 32 3271-76 (1997)

58. H. J. Bardeleben, J. L. Cantin, A. Zeinert, B. Racine, K. Zellama, P. N. Hai, "Spins and microstructure of hydrogenated amorphous carbon: A multiple frequency electron paramagnetic resonance study", *App. Phys. Letters*, 78, 2843-45 (2001)

59. Y. Yafet, *Solid State Physics* V14, Ed.H Ehrenreich, F. Seitz, D. Turnbull, Academic, N-Y. (1966)

60. J. Seitz, J. Bill, N. Eggert, F. Aldinger, "Structural investigations of Si/C/N-ceramics from polysilazane precursors by nuclear magnetic resonance,"*J. Eur. Ceram. Soc*. **16** 885-91 (1996)

61. S. Traßl, D. Suttor, G. Motz, E. Rossler, G. Ziegler, "Structural characterisation of silicon carbonitride ceramics derived from polymeric precursors,"*J. Eur. Ceram. Soc*. **20,** 215-25 (2000)

62. S. Traßl, G. Motz, E. Ro¨ssler, G. Ziegler, "Characterization of the free-carbon phase in precursor-derived Si-C-N ceramics: I, spectroscopic methods,"*J. Am. Ceram. Soc*. **85,** 239-44 (2002)

63. S. Traßl, H.-J. Kleebe, H. Sto¨rmer, G. Motz, E. Rossler, G. Ziegler, "Characterization

of the free-carbon phase in Si-C-N ceramics: Part II, comparison of different polysilazane precursors," *J. Am. Ceram.Soc.* **85** 1268-74 (2002)

64. J. Durr, P. Lamparter, J. Bill, S. Steeb, F. Aldinger, "An X-ray and neutron scattering investigation of precursor derived Si24C43N33 ceramics,"*J. Non-Cryst. Solids* **234** 155-61 (1998)

65. N. Janakiraman , F. Aldinger, "Fabrication and characterization of fully dense Si–C–N ceramics from a poly(ureamethylvinyl)silazane precursor", *J. Euro. Ceramic Society* 29 (2009) 163–173

66. Y. S. Wang, L. G. Zhang, W. X. Xu, T. Jiang, Y. Fan, D. P. Jiang, L. N. An, "Effect of Thermal Initiator Concentration on the Electrical Behavior of Polymer-Derived Amorphous Silicon Carbonitrides", *J. Am. Ceram. Soc.*, 91 [12] 3971–3975 (2008)

67. http://ieeexplore.ieee.org/stamp/stamp.jsp?arnumber=01266360 H. Z. Ding, B. R. Varlow, "Raman Spectroscopy— A Technique to Assess the Residual Stress in Fiber-Reinforced Polymeric Insulation Materials"

68. J. W. Ager III, S. Anders, A. Anders, I. G. Brown, "Effect of intrinsic growth stress on the Raman spectra of vacuum-arcdeposited amorphous carbon films", *Appl. Phys. Lett.*, **66** (25), 19 (1995)

69. S. Hataka, G. Dresselhaus, M. S. Dresselhaus, M. Endo, "Effect of uniaxial stress on the Raman spectra of graphite fibers", *J. App. Phys.*, 63(8) 15, 2769-72(1988)

70. J. Wu**,** Ph. Colomban**, "**Raman Spectroscopic Study of the Stress Distribution in

Continuous Fibre-Reinforced Ceramic Matrix Composites", *J. Raman Spectrosc.*, 28, 523-529 (1997)

71. Y. l. Ward, R. J. Young, R. A. Shatwell, "Determination of residual stresses in SiC monofilament reinforced metal-matrix composites using Raman spectroscopy", *Composites: Part A* 33 1409–1416 (2002)

72. J. R. Ferraro, K. nakamoto, C. W. Brown, *Introductory Raman Spectroscopy*, 2nd ed., Elsevier, 2003

73. X. C. Wu, R. Q. Cai, P. X. Yan, et al, "SiCN thin film prepared at room temperature by r.f. reactive sputtering", *Applied Surface Science*, 2002, 185, 262-266

74. M. Schulz, M. Börner, J. Haußelt, R. Heldele, "Polymer derived ceramic microparts from X-ray lithography—cross-linking behavior and process optimization", *J Eur Ceram Soc*, 2005, 25, 199-204

75. E. Xie, Z. Ma, H. Lin, et al, "Preparation and characterization of SiCN films", *Optical Materials*, 2003, 23, 151-156

76. K. B. Sundaram, J. Alizadeh, "Deposition and optical studies of silicon carbide nitride thin films", *Thin Solid Films*, 2000, 370, 151-154

77. Y. P. Guo, J. C. Zheng, A. S. Wee, et al, "Photoluminescence studies of SiC nanocrystals embedded in a SiO2 matrix", *Chem Phys Lett*, 2001, 339,319-322

78. W. F. A Besling, A. Goossens, B. Meester, J. Schoonman, "Laser-induced chemical vapor deposition of nanostructured silicon carbonitride thin films", *J. Appl Phys*, 1998,

83, 544-553

79. F. Berger, M. Weinmann, F. Aldinger and K. Muller, "Solid-state NMR Studies of the Preparation of Si-Al-C-N Ceramics from Aluminum-modified Polysilazanes and Polysilycarbodiimides," *Chem. Mater. 16,* 919-929 (2004)

80. K. J. D. Mackenzie and M. E. Smith *Multinuclear Solid-State NMR of Inorganic Materials*, Pergamon, 2002.

81. N. S. C. K. Yive, R. Corriu, D. Leclercq, P.H. Mutin, and A. Vioux, "Polyvinylsilazane- a Novel Precursor to Silicon Carbonitride," *New J. Chem*., *15*, 85-92 (1991)

82. T. Shimizu, M. Kumeda, and Y. Kiriyama, Solid State Commun. **37**, 699 (1981)

83. F. Berger, A. Muller, F. Albinger, K. Muller, Z. Anorg, "Solid-state NMR Investigations on Si_B_C_N Ceramics derived from Boron-Modified Poly(allylmethylsilazane)", Allg.Chem. **631**, 355 (2005)

84. A. Saha, R. Raj, D. L. Williamson, and H. K. Kleebe, ''Characterization of Nanodomains in Polymer-Derived SiCN Ceramics Employing Multiple Techniques,'' *J. Am. Ceram. Soc.*, 88, 232–4 (2005)

85. R. Raj, R. Riedel, and G. Soraru, ''Introduction to the Special Topical Issue on Ultrahigh-Temperature Polymer-Derived Ceramics,'' *J. Am. Ceram. Soc.*, 84, 2158–9 (2001)

86. P. A. Ramakrishnan, Y. T.Wang, D. Balzar, L. An, C. Haluschka, R. Riedel, and A.

Herman, ‘‘Silicoboron–Carbonitride Ceramics: A Class of High-Temperature, Dopable Electronic Materials,’’ *Appl. Phys. Lett.*, 78 [20] 3076–8 (2001)

87. A. M. Hermann, Y. T. Wang, P. A. Ramakrishnan, D. Balzar, L. An, C. Haluschka, and R. Riedel, ‘‘Structure and Electronic Transport Properties of Si–(B)–C–N Ceramics,’’ *J. Am. Ceram. Soc.*, 84 [10] 2260–4 (2001)

88. Y. Wang, T. Jiang, L. Zhang, Y. Fan, D. Jiang, and L. An, ‘‘Electron Transport in Polymer-Derived Amorphous Silicon Carbonitrides,’’ *Appl. Phys. Lett.*, in review

89. B. Lundberg and B. Sundqvist, ‘‘Resistivity of a Composite Conducting Polymer as a Function of Temperature, Pressure, and Environment: Applications as a Pressure and Gas Concentration Transducer,’’ *J. Appl. Phys.*, 60, 1074–9 (1986)

90. A. Celzard, E. McRae, J.F. Maêché, and G. Furdin, “Conduction mechanisms in some graphite–polymer composites: Effects of temperature and hydrostatic pressure”, *J. Appl. Phys*. **83**, 1410 (1998)

91. N.F. Mott, and E.A. Davis, *Electronic Processes in Non-Crystalline Materials*, (Clarendon Press, Oxford, 1971)

92. N.F. Mott, Philos. Mag. **19**, 835 (1969)

93. G. Jeschke, M. Kroschel, and M. Jansen, “A magnetic resonance study on the structure of amorphous networks in the Si±B±N(±C) system”, *J. Non-Cryst. Solids* **260**, 216 (1999)

94. Y. Wang, *Polymer-Derived Si-Al-C-N Ceramics: Oxidation, Hot-Corrosion and*

Structural Evolution, Ph.D. dissertation, University of Central Florida, 2006

95. C. Godet, "Physics of bandtail hopping in disordered carbons", *Diamond Relat. Mater.* **12**, 159 (2003)

96. C. Godet, "Hopping model for charge transport in amorphous carbon", *Philos. Mag. B* **81**, 205 (2001)

97. C. Godet, "Variable range hopping revisited: the case of an exponential distribution of localized states" *J. Non-Cryst. Solids* **299**, 333 (2002)

98. S.H. Moustafa, M. Koos, and I. Pocsik, "DC electrical properties of amorphous carbon with different bonding hybridization", *J. Non-Cryst. Solids* **227-230**, 1087 (1998)

99. G. Lazar, K. Zellama, N. Clin, and C. Godet, "Band tail hopping conduction mechanism in highly conductive amorphous carbon nitride thin films", *Appl. Phys. Lett.* **85**, 6176 (2004)

100. K. Rohwer, P. Hammer, and J.U. Thiele, "Electrical and optical properties of plasma-deposited amorphous hydrocarbon films", *J. Non-Cryst. Solids* **137-138**, 843 (1991)

101. J. Tauc, in *Optical Properties of Solids*, ed. F. Abeles, North-Holland, Amsterdam, 1971

102. P. O'Connor and J. Tauc, "Spectrum of photoinduced optical absorption in a-Si: H", *Solid State Commun*. **36**, 947 (1980)

103. D. Pfost, H. Liu, Z. Vardeny and J. Tauc, "photoinduced absorption spectra in Ge:H and

Si:H", *Phys. Rev. B* **30**, 1083 (1984)

104. J.C. Inkson, "Deep impurities in semiconductors: 11. The optical cross section", *J. Phys. C: Solid State Phys*. **14**, 1093-101(1981)

105. S.Trassl, G.Motz, E.Rossler and G. Ziegler, "Characterization of free carbon phase in precursor derived SiCN ceramics:q, spectroscopic methods", *J. Am. Ceram. Soc*, **85**, 239-44 (2002)

106. P.M. Schneider and W.B. Fowler, "band structure and optical properties of Silicon Dioxide", *Phys. Rev. Lett.* **36**, 425-428 (1976)

107. I.P. Kaminow, B.G. Bagley and C.G. Olson, "measurements of the absorption edge in fused silica", *Appl. Phys. Lett.* **32**, 98-99 (1978)

108. J.B. Casady and R.W. Johnson, "Status of silicon carbide as a wide-bandgap semiconductor for high temperature applications: a Review", *Solid State Elect.* **39**, 1409-1422 (1996)

109. S.V. Deshpande, E. Gulari, S.W. Brown and S.C. Rand, "Optical properties of silicon nitride films deposited by hot filament chemical vapor deposition", *J Appl. Phys*.**77**, 6534(1995)

110. S.I. Andronenko, I. Stiharu and S.K.Misra "Synthesis and characterization of polyureasilazane derived SiCN ceramics", *J. Appl. Phys.* **99**, 113907 (2006)